UNIVERSITÉ DE MONTRÉAL

COMPUTATION OF FREQUENCY DEPENDENT NETWORK EQUIVALENTS USING VECTOR FITTING, MATRIX PENCIL METHOD AND LOEWNER MATRIX

JESÚS MORALES RODRÍGUEZ

DÉPARTEMENT DE GÉNIE ÉLECTRIQUE

ÉCOLE POLYTECHNIQUE DE MONTRÉAL

THÈSE PRÉSENTÉE EN VUE DE L'OBTENTION

DU DIPLÔME DE PHILOSOPHIAE DOCTOR

(GÉNIE ÉLECTRIQUE)

MAI 2019

UNIVERSITÉ DE MONTRÉAL

ÉCOLE POLYTECHNIQUE DE MONTRÉAL

Cette thèse intitulée :

COMPUTATION OF FREQUENCY DEPENDENT NETWORK EQUIVALENTS USING VECTOR FITTING, MATRIX PENCIL METHOD AND LOEWNER MATRIX

présentée par : MORALES RODRÍGUEZ Jesús

en vue de l'obtention du diplôme de : Philosophiae Doctor

a été dûment acceptée par le jury d'examen constitué de :

M. HOUSHANG Karimi, Ph. D., président

M. MAHSEREDJIAN Jean, Ph. D., membre et directeur de recherche

M. KOÇAR Ilhan, Ph. D., membre et codirecteur de recherche

M. RAMIREZ Abner, Ph. D., membre et codirecteur de recherche

M. SHESHYEKANI Keyhan, Ph. D., membre

M. FILIZADEH Shaahin, Ph. D., membre externe

DEDICATION

To Leonel, Zuria, and Orlandito.

ACKNOWLEDGEMENTS

Firstly, I would like to thank professors Jean Mahseredjian and Ilhan Kocar for their trust since the first contact we had for coming to Polytechnique de Montréal, but also for the guidance and for sharing their expertise as researchers during my PhD studies.

Equally, I would like to express my enormous gratitude to professor Abner Ramírez, first, for encouraging me to come to Canada to pursue the PhD degree, and second, for his wise advices, not only as a professor but also as a friend.

Also, my sincere thanks to professor Keyhan Sheshyekani for his very valuable advices and guidance during my PhD.

I would like to specially thank the person who encourages me every day to achieve my personal goals, who has changed the way I understand life, and therefore, has been very important during this stage of my life, Gwendoline.

Also, many thanks to my family, my parents Jesus and Pilar, and my sisters Janine and Jessica, for the encouragement and for the unconditional support in both, good and difficult times.

Many thanks to my department colleagues, who are my friends at the same time, Miguel, Haoyan, Ming, Anton, Aramis, Reza, professor Akiro Ametani, Isabel, Masashi, Baki, Thomas, Nazak, Diane, David, Aboutaleb, Serigne, Louis, Willy and Edgar, for all the good moments we have spent together.

Finally, I would like to thank the chair partners: Polytechnique de Montréal, CNSRC, Hydro-Québec, Opal-RT, EDF and RTE for the financial support.

RÉSUMÉ

Cette thèse présente l'analyse des techniques existantes et des nouveaux développements pour le calcul d'équivalents de réseaux électriques (FDNEs en anglais). Les FDNEs sont des modèles rationnels d'ordre réduit de dispositifs ou de parties de réseaux, utilisés pour l'accélération des simulations de transitoires électromagnétiques. Un FDNE est calculé de façon à ce que sa réponse fréquentielle corresponde à celle du système original dans une bande de fréquences definie. Ce qui permet la réduction de l'ordre du modèle et par conséquent, la réduction du temps de calcul des simulations dans le domaine du temps.

Pour l'application de la technique FDNE, le système original et le modèle équivalent doivent être linéaires, causals et passifs. Ces caractéristiques sont étudiées en détail dans cette thèse, ainsi que la dérivation mathématique de la matrice Hamiltonienne et la matrice de singularité associée pour l'évaluation de la passivité des FDNEs.

Les FDNEs sont calculés à l'aide d'une technique d'ajustement de courbes. Ensuite, la passivité du modèle doit être évaluée, et, si des violations de passivité sont découvertes, une technique pour forcer la passivité du modèle doit être appliquée pour assurer la stabilité numérique du modèle.

Dans la littérature, les techniques existantes pour l'ajustement de courbes et pour forcer la passivité des modèles rationnels sont nombreuses, donc, les plus matures ont été sélectionnées et étudiées. Les théories de ces techniques sont analysées et comparées avec des exemples numériques. À partir des résultats obtenus des ces études, la technique Vector Fitting (VF) est reconnue comme la plus précise. Cependant, les techniques Matrix Pencil Method (MPM) et Loewner Matrix (LM) sont reconnues comme des techniques utiles pour l'identification de l'ordre des modèles équivalents. Finalement, une nouvelle technique est proposée en combinant les techniques étudiées. La méthodologie proposée est plus efficace que les techniques étudiées appliquées de façon individuelle.

En ce qui concerne la passivité des modèles FDNE, un problème majeur avec les techniques qui forcent la passivité est identifié comme suit. Pour des FDNEs d'ordre élevé, ou des FDNEs dotés de nombreux ports de connexion, ou une combinaison des deux, les techniques étudiées, Fast Residue Perturbation (FRP), Hamiltonian Matrix Perturbation (HMP) et Semidefinite Programming (SDP) sont numériquement très coûteuses, et parfois incapables de trouver une solution. Donc, une nouvelle technique, nommée Pole-Selective Residue Perturbation (PSRP) est

proposée. Contrairement aux techniques traditionnelles, la technique PSRP calcule les perturbations de façon algébrique, permettant une meilleure performance numérique que les techniques FRP, HMP et SDP. En plus, la technique proposée permet de trouver des solutions aux problèmes pour lesquels les techniques traditionnelles échouent.

ABSTRACT

This thesis presents a thorough analysis of existing techniques and new developments for the calculation of Frequency-Dependent Network Equivalents (FDNEs). FDNEs consist of reduced-order rational models of devices or subnetworks aimed at acceleration of electromagnetic transient (EMT) simulations. A FDNE is calculated such that the frequency-response of the original model is matched for a finite frequency band, this allows the reduction of the model order and consequently, the reduction of computational burden in time-domain simulations.

For the application of the FDNE approach, both, the original and equivalent (FDNE) models are required to be linear, causal and passive. These modeling requirements are studied in detail in this thesis. Also, the mathematical derivation of the Hamiltonian matrix and associated singularity test matrix for the passivity assessment of rational models is reviewed.

The computation of FDNEs is achieved by applying a curve fitting approach to identify the system's equivalent rational model. Then, the passivity of the model must be assessed, and, in case that passivity violations are revealed, a passivity enforcement technique must be applied to guarantee numerical stability of the model in transient simulations.

Since different techniques exist for both, rational modeling and passivity enforcement, the most relevant are chosen and further studied. The theories of these techniques are first revisited, then, the studied techniques are compared with numerical examples. From these numerical studies, the Vector Fitting (VF) technique is demonstrated to be the most accurate technique for rational modeling. However, the Matrix Pencil Method (MPM) and Loewner Matrix (LM) technique are shown to be useful methods for model order identification. Thus, a novel fitting technique, consisting of a combination of the above-mentioned techniques, is proposed. The new methodology is demonstrated to be more efficient than any of the involved techniques applied independently.

Regarding the passivity enforcement stage, a major issue is identified as follows. For high-order FDNE models, or FDNEs with many connection ports, or a combination of both, available passivity enforcement techniques, such as the Fast Residue Perturbation (FRP), Hamiltonian Matrix Perturbation (HMP) and Semidefinite Programming (SDP), are either computationally very expensive or unable to find a solution due to the large computational burden required. Then, a novel passivity enforcement technique named Pole-Selective Residue Perturbation (PSRP) is

proposed. Unlike the existing techniques, the PSRP method consists of algebraic calculations, instead of solving optimization problems as required by the traditional methods. This feature of the proposed technique allows improved computational performance compared to the FRP, HMP and SDP techniques. Additionally, the proposed method allows finding a solution to problems for which the traditional techniques fail.

TABLE OF CONTENTS

LIST OF TABLES

LIST OF FIGURES

LIST OF SYMBOLS AND ABBREVIATIONS

BIBO	Bounded-input bounded-output
CFIFT	Closed-form inverse Fourier transform
CPU	Central processing unit
EMT	Electromagnetic transients
EMTP	Electromagnetic transient program
FD	Frequency domain
FFT	Fast Fourier transform
FRP	Fast residue perturbation
HMP	Hamiltonian matrix perturbation
HVDC	High voltage direct current
IFFT	Inverse fast Fourier transform
LM	Loewner matrix
LTI	Linear time invariant
MPM	Matrix pencil method
PRL	Positive real lemma
PSRP	Pole-selective residue perturbation
ROC	Region of convergence
SDP	Semidefinite programming
TD	Time domain
VF	Vector fitting
WF	Wind farm

LIST OF APPENDICES

CHAPTER 1 INTRODUCTION

The increasing complexity of modern electrical networks around the world has made essential the use of simulation software for electromagnetic transient (EMT) analysis. EMT-type simulations are widely used for design, operation and analysis of power systems. The large number of nodes in modern electrical networks, together with the complexity of its components results in very high computational burden for EMT-type simulations. This issue can be addressed using Frequency-Dependent Network Equivalents (FDNEs).

The computation of an FDNE requires to divide the network under study into study- and external-zone. The external zone is replaced by the FDNE as illustrated in Figure 1.1. The FDNE constitutes an equivalent reduced-order model of the external zone of the network, which allows the acceleration of time-domain computations. A restriction of FDNEs is that only linear and passive devices can be modelled.

In general, the calculation of FDNEs involves the following steps: 1. computation of the frequency response of the external zone of the network (impedance, admittance, scattering parameters or transfer function), 2. identification of the frequency response, normally achieved via a curve fitting technique, 3. passivity assessment of the identified frequency response and, if required, 4. passivity enforcement. The passivity condition is related to the inability of the model to generate energy, this condition is vital for the numerical stability of FDNE models in time-domain (TD) simulations.

The FDNE approach is not a novel technique and many research works have been conducted on this topic. Thus, several techniques exist for the calculation of FDNEs and passivity enforcement as discussed in the literature review presented next.

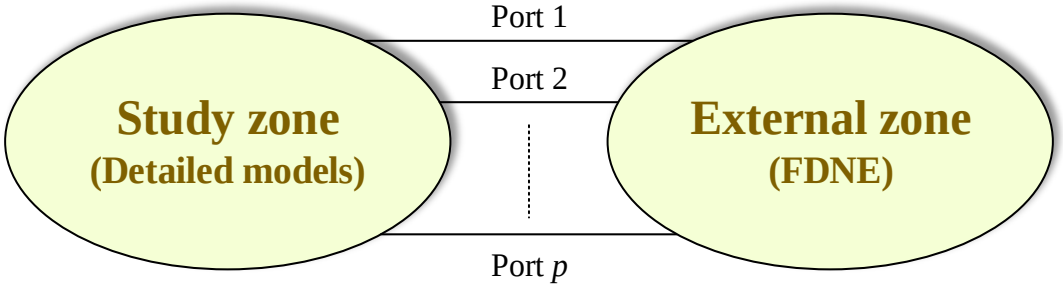

Figure 1.1. Application of the FDNE approach.

1.1 Literature review

Since the decade of 1950, some techniques to calculate the parameters of transfer functions of electrical systems from experimentally-obtained frequency responses have been developed; for example, [1-3] in the field of automatic control. In the field of power systems, those techniques were developed two decades later. In 1970, a Transient Network Analyzer (TNA) combined with digital computer for the simulation of open-end switching lines was developed [4]. The TNA consisted of a small-scale physical implementation used with a similar purpose than FDNEs. However, with the development of computers, the TNA looks impractical at present.

The calculation of FDNEs has emerged together with the necessity of accurately representing system components with distributed-parameters nature, such as transmission lines and transformers. In the decade of 1970, for example, a combination of resistive, inductive, and capacitive (RLC) elements in the form of interconnected cascade modules, were used for the representation of transmission lines [5, 6]. This technique was enhanced in 1980 and 1981 for lossless and lossy models, respectively [7, 8]. The same concept was utilized for the modeling of network equivalents for transient analysis in 1983, as reported in [9]. Using the same idea (RLC branches), but with a different procedure for the parameters determination, an alternative approach was proposed in 1984 in [10], and later extended to multiport systems in 1993 in [11].

A different approach for the computation of FDNEs, consisting of difference-equation models was proposed in [12] and [13, 14], published in 1993 and 2004, respectively. The difference-equation models are, however, limited to single-port systems, and for this reason they have never been very popular.

In 1993, an alternative technique to interface equivalent models by means of the Fast Fourier Transform (FFT) was proposed in [15]. This approach takes advantage of the delay produced by a transmission line to connect the study- with the external-zone. This technique is, however, very restrictive since a transmission line must be the breakpoint between the study- and external-zone.

The Vector Fitting (VF) technique first appeared in 1998 for the modeling of transmission lines [16, 17]. In the same year, the application of the VF technique was extended to power transformers [18], and finally to FDNEs in 1999 [19]. A further analysis of the VF method, given in [20], recognizes the VF technique as an improved version of Sanathanan and Koerner method published

in 1963 [21]. Some improvements for the application of VF to multiport systems were published in 2002 for the fitting of admittance matrices in [22]. An alternative application of the VF technique in the *z*-domain was also proposed in 2007 in [23].

In 2003, a two-layer network equivalent was proposed [24]. In this approach, the external-zone is divided in two layers: a surface layer, consisting of a transmission line connected directly to the study-zone, and an inner layer, containing the rest of the network. The restriction of this technique is that it requires the surface layer to be a transmission line modeled as in [25].

Frequency-band partitioning was proposed in 2005 as an alternative fitting technique [26]. This frequency partitioning allows the computation of rational models via the solution of simple overdetermined system of equations. The reliability of this approach is however, dependent on the user's expertise to define the frequency partitions.

In addition to the above-mentioned frequency-domain identification methods, dynamic equivalents can also be computed from time-domain responses. This is the case of the Matrix Pencil Method (MPM) [27], which was published in 1995, as an extension of [28]. Alternative time-domain identification approaches are the Prony method [29] and the TD-VF method [30], published in 1995 and 2003, respectively.

One of the most important questions in the computation of FDNEs is how to determine the fitting model order. Since 2010, a partial solution to this question was given by applying the MPM method in FD, as proposed in [31, 32]. Also, different Loewner-matrix based methods as reported in [33-35] include the model order identification feature. These techniques utilise singular value decomposition (SVD) to find a suitable model order. Moreover, these two techniques are non-iterative. Another model order identification method was proposed in 2016 [36]. This method consists of a combination of the Prony method with SVD.

As mentioned before, an essential requirement of FDNEs to perform numerically stable simulations is passivity. Passivity-guaranteed fitting methods are reported in [37] and [38], published in 2011 and 2017, respectively. In [37], genetic algorithms are applied to identify the coefficients of the equivalent model. On the other hand, the method in [38] consists of Brune's realizations, which is an old approach, appeared around 1931 [39]. These passivity-guaranteed approaches are, however, only available for single-port systems.

Since the rest of existing fitting techniques cannot guarantee the passivity of FDNEs, a passivity assessment is always necessary, and if passivity violations are revealed, passivity must be enforced. Passivity can be assessed by computing the eigenvalues of the Hamiltonian matrix associated to the FDNE (state-space) model [40]. Alternatively, passivity can be assessed via the singularity test matrix [41]. As its name indicates, this matrix is half-size of the Hamiltonian matrix, then, it is computationally more efficient.

In the context of passivity enforcement, several methods have been reported in the literature. One of the most popular is the Fast-Residue Perturbation (FRP) technique, which consists of the solution of an optimisation problem via quadratic programming [42]. Another popular technique is the perturbation of the Hamiltonian matrix associated to the state-space representation of the rational model, which in turn, results in the perturbation of the state-space FDNE model [40]. Also, Positive Real Lemma (PRL) -based techniques have been proposed for passivity enforcement. Under this approach, the resulting optimization problem can be solved via Semidefinite Programming (SDP) as in [43]. A more recent approach was proposed in [44], which is an improved version of the SDP technique.

To conclude this literature review, it is remarked that there exist surveys about the computation of dynamic equivalents, some of them are given in [45-48], and chapter 10 of [49]. These references have been the primary source of information for this thesis.

1.2 Motivation

Although the use of FDNEs has been widely reported in the literature, and several approaches exist, the accuracy of the equivalent models relies on both, the techniques applied, and the user's expertise. For example, a common user may utilize a very accurate fitting technique but a bad model order estimation, which can result in a poor accuracy of the approximation. Also, since FDNEs are prone to violate passivity, a suitable passivity enforcement technique should be selected and appropriately applied for accurate and stable solution. As it will be later demonstrated, in some cases, the existing passivity enforcement methods require large CPU times to enforce passivity, or in the worst scenario, they are unable to find a solution due to the large computational burden required. These issues constitute the main challenges and motivation of this thesis to create improved methods for the computation of FDNEs.

1.3 Scope

In this section, some important facts about the use of FDNEs are shown. Firstly, it is highlighted that with the development of computers and simulation software, some problems that used to be challenging in the past, are much easier to be solved nowadays. As preliminary example, the 500-kV transmission network used in [26] for the calculation of an FDNE, has been reproduced in EMTP [50]. The resulting draw is presented in Figure 1.2.

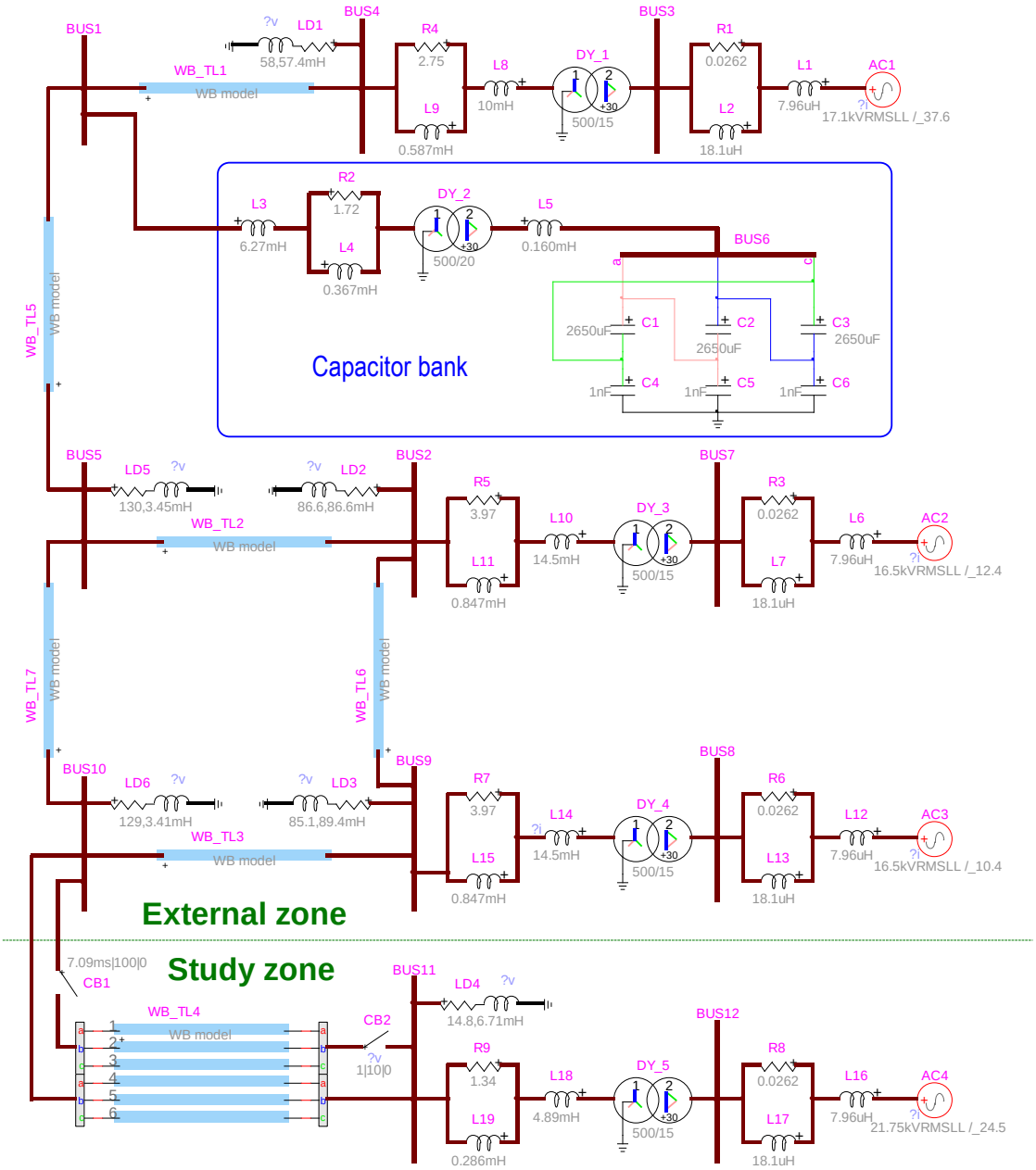

Figure 1.2. 500-kV transmission network studied in [26], redrawn in EMTP.

Computing the TD simulation for the example of Figure 1.2 using a simulation time of 30 ms and a time-step of 5 μs, the resulting CPU simulation time is 0.32 s. Thus, it can be seen that the use of an FDNE is not worth it for this example since the simulation can be achieved very quickly.

Another case where the application of FDNEs is not meaningful is the simulation of networks with highly-complex devices that cannot be included into the FDNE model, such as windfarms (WF) and HVDC systems. An example of such cases is the 345-kV network of Figure 1.3.

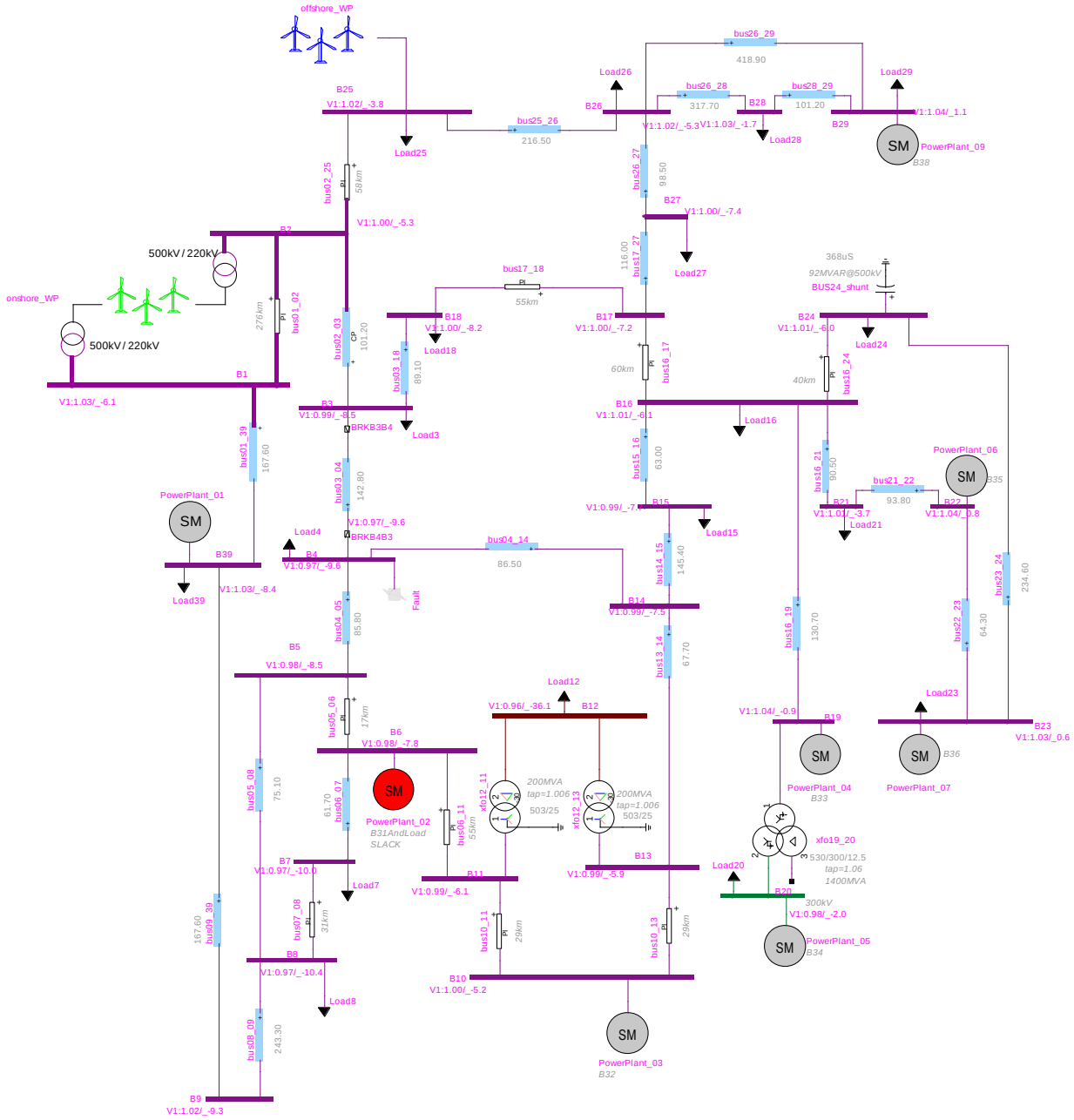

Figure 1.3. 345-kV transmission network.

For the application of the FDNE approach in the test network of Figure 1.3, the study-zone must necessarily contain the WFs since those are nonlinear devices and they cannot be modeled by FDNEs. Different tests using FDNEs have been applied to this network; however, no substantial computational saving is achieved. The reason is that, most of the computational burden is demanded by the nonlinear devices, and since those are kept modeled in detail (inside the study-zone), the application of an FDNE cannot substantially accelerate the simulation.

An example that demonstrates the capabilities of FDNEs is the 225-kV cross-bonded cable system studied in [51] and shown in Figure 1.4. The cross-bonded cable of Figure 1.4 consists of 17 blocks, each of them containing 3 sections of the frequency dependent cable model based on [52]. The total cable length is 64 km and the shortest cable section propagation delay is 4.87×10^{-5} s. Further details about the cable modeling are given in [51, 53] and in section 4.6 of this thesis. For this example, it is important to remark that the simulation time-step cannot be larger than the above-mentioned (shortest) propagation delay.

Unlike other cable modelling techniques, such as the homogeneous model [52], the FDNE technique allows to tune the accuracy of the model by selecting the desired fitting frequency band and model order. Additionally, the use of an FDNE eliminates the restriction of the largest possible time-step, imposed by the shortest time-delay of the cable model.

Using a FDNE fitted for a frequency band from 1 Hz to 5 kHz, for a simulation time of 0.1 s and time-step of 4 μs, the CPU simulation time is reduced from 13 s to 0.59 s, i.e., an acceleration factor of 21 is obtained. Alternatively, using a time-step of 20 μs, the simulation CPU time can be reduced to 0.22 s, i.e. an acceleration factor of 58 is obtained.

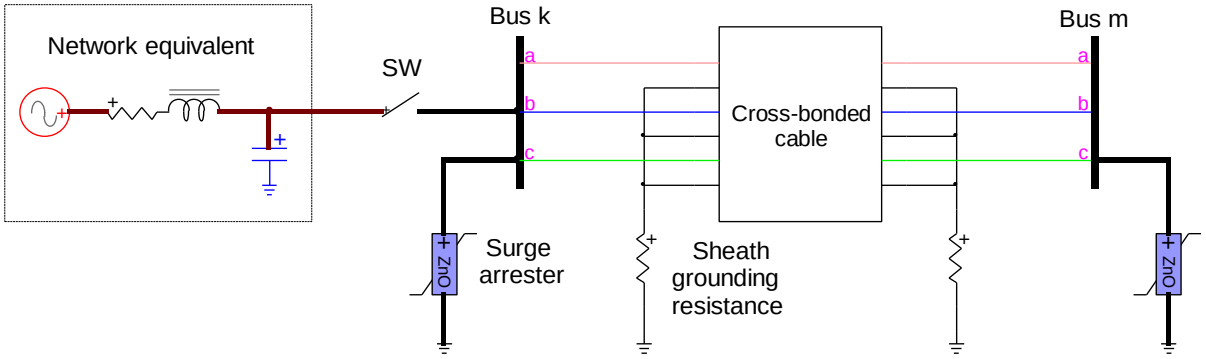

Figure 1.4. 225-kV Cross-bonded transmission cable system.

Moreover, the use of FDNEs is especially advantageous for statistical studies. To cite an example, statistical studies are used for the determination of the maximum overvoltage due to a breaker switching, for which the simulations are repeated several times (50 times or more, for example) with different closing instants to find the critical voltage values.

The examples presented above show that the computational savings obtained by using FDNEs depend on several factors, such as number of nodes of the network, complexity of the models involved, number of connections ports, fitting frequency band, FDNE model order, simulation time, simulation time-step, among others. Therefore, it is emphasized that this thesis does not focus on the computational savings by using FDNEs since they depend on all the abovementioned factors. The scope of this thesis relies on the study of the FDNE modeling requirements, and the methodologies involved in the computation of FDNEs, such as fitting techniques, model order determination, and passivity enforcement.

Note that the simulation results presented in this chapter and all the simulation results presented in this thesis are achieved using a 16-GB of RAM, i7-4900MQ@2.80 GHz processor and 64-bit Windows operating system computer.

1.4 Contributions

The first contribution of this thesis consists of the proposal of a novel fitting procedure based on the Loewner-Matrix (LM) method. This new methodology is more straightforward than the traditional one in terms of extraction of unstable poles. Furthermore, the sparsity of the model obtained by the proposed strategy allows better computational efficiency in time-domain than the traditional LM technique. Subsequently, a comparative study of existing fitting techniques is presented. This study reveals some discoveries that had not been reported in the literature.

The second contribution of this thesis consists of a new fitting method that combines the Vector Fitting (VF) technique with either LM or the Matrix-Pencil-Method (MPM), which allows an easy model order identification and high fitting accuracy. The proposed technique achieves improved computational performance than the existing methods.

The third contribution of this thesis is the proposal of a novel passivity enforcement technique. Unlike existing methods, the proposed technique requires minimal computational effort, which make it advantageous for FDNEs with substantial number of connection ports and model order.

1.5 Thesis outline

Chapter 1 introduces the research topic, including a brief analysis about the computational savings by using FDNEs. This analysis defines the scope of the research.

In Chapter 2, the theoretical background for the calculation of FDNEs is presented, including: a study on the physical and mathematical requirements for FDNE modeling, such as linearity, causality and passivity.

Chapter 3 presents a review on: 1. Vector Fitting (VF), Matrix Pencil Method (MPM) and Loewner Matrix (LM) fitting techniques; 2. passivity assessment methods; and, 3. passivity enforcement techniques, such as the Fast Residue Perturbation (FRP), Hamiltonian Matrix Perturbation (HMP) and Semidefinite Programming (SDP) methods.

In Chapter 4, numerical analysis and comparisons between the VF, MPM and LM fitting techniques are presented. These studies reveal the capabilities and weakness of each technique. Also, some recommendations are given for the efficient application of the outlined methods. Different frequency-domain functions are fitted and analyzed in this chapter.

Based on the discoveries obtained in Chapter 4, a new fitting technique is proposed in Chapter 5. The proposed technique consists of a combination of the MPM or the LM method with the VF technique. The proposed technique is demonstrated to achieve better computational performance than the involved techniques applied individually.

In Chapter 6, the passivity enforcement techniques Fast Residue Perturbation (FRP), Hamiltonian Matrix Perturbations (HMP) and Semidefinite Programming, are first evaluated with some numerical examples, revealing their limitations. Then, a novel passivity enforcement technique, named Pole-Selective Residue Perturbation (PSRP) is presented. The proposed technique is demonstrated to achieve similar (slight) deviation of the rational model after passivity enforcement, while achieving a much better computational performance.

Finally, a summary of the work presented in this thesis is given in Chapter 7, followed by some ideas for future work.

CHAPTER 2 PRELIMINARIES ON RATIONAL MODELING

Rational modeling constitutes a powerful tool for reliable representation of dynamic systems in time-domain simulations. Dynamic systems can be usually represented by differential equations in time-domain. Sometimes, however, the determination of the differential equations for some devices/systems is not straightforward, such as the case of devices with distributed parameters nature. For those cases, rational modeling is an effective alternative.

The process of calculating the coefficients of the rational model is known as identification process. This identification process is usually achieved by fitting the curve drawn by the frequency-response of the device/system under study. In the field of power systems, rational modeling is usually applied to frequency-dependent elements such as transmission lines/cables and transformers and to obtain frequency dependent network equivalents (FDNEs).

As revealed in the literature review given in Chapter 1, several fitting approaches have been proposed for the identification of dynamic systems; however, it is a tremendous task to study all the existing methods. This thesis focuses on the study of three of them: the VF, MPM and LM techniques. The VF is primarily considered since its use is very popular in both, research and industry applications. Moreover, the VF technique has been continuously improved. On the other hand, recent papers have been published about the MPM and LM methods, which demonstrate attractive features, such as, automatic model order determination, no need of initial poles guessing, and no need of iterative methods.

The VF, MPM and LM techniques produce rational/state-space models whose transfer function match the frequency response of the subnetwork or device being modeled over a finite frequency band. This frequency response can be given in admittance-, impedance-, scattering-parameters or transfer functions. Since this thesis focuses on FDNE modeling for EMT-simulations, admittance-parameters are of especial interest for compatibility with the EMTP software [50]. The rational models computed in this thesis are obtained using Matlab [54]. Note that the definitions given in this thesis for admittance-parameters also apply to impedance-parameters functions, whereas for transfer functions and scattering-parameters some definitions and/or modeling requirements, such as passivity may be slightly different.

Under the abovementioned considerations, the input data to the VF, MPM and LM techniques is the frequency-sampled admittance matrix

$$\mathbf{Y}(s)=\begin{bmatrix} y_{11}(s) & \cdots & y_{1p}(s) \\ \vdots & \ddots & \vdots \\ y_{p1}(s) & \cdots & y_{pp}(s) \end{bmatrix}, \tag{2.1}$$

where p denotes the number of ports, and the corresponding frequency points

$$s=\begin{bmatrix} s_1 & \cdots & s_{N_s} \end{bmatrix}, \tag{2.2}$$

where $s=j\omega$, $\omega=2\pi f$ being f the frequency in Hz and N_s is the number of frequency samples.

The output model given by the VF and MPM fitting techniques is the rational model

$$\mathbf{Y}_{fitted}(s)=\sum_{n=1}^{N}\frac{\mathbf{R}_n}{s-a_n}+\mathbf{D}+s\mathbf{E}, \tag{2.3}$$

where coefficients a_n and $\mathbf{R}_n$ are denoted as the poles and residue matrices, respectively; $\mathbf{D}$ and $\mathbf{E}$ are constant matrices, which define the asymptotic frequency-response of the model; and N denotes the order of the model.

The rational model in (2.3) can equivalently be expressed in state-space form, which is also the model obtained by the LM method as

$$\dot{\mathbf{x}}(t)=\mathbf{A}\mathbf{x}(t)+\mathbf{B}\mathbf{v}(t), \tag{2.4}$$

$$\mathbf{i}(t)=\mathbf{C}\mathbf{x}(t)+\mathbf{D}\mathbf{v}(t)+\mathbf{E}\dot{\mathbf{v}}(t), \tag{2.5}$$

where the input vector $\mathbf{v}(t)$ denotes node voltages and the output vector $\mathbf{i}(t)$ denotes branch currents. Thus, the fitted frequency-response can equivalently be expressed as the transfer function of the outlined state-space model as

$$\mathbf{Y}_{fitted}(s)=\mathbf{C}(s\mathbf{I}-\mathbf{A})^{-1}\mathbf{B}+\mathbf{D}+s\mathbf{E}, \tag{2.6}$$

where $\mathbf{I}$ denotes the identity matrix. The conversion from the rational model (2.3) to the state-space form (2.4)-(2.5) is given in Appendix A.

2.1 Modeling requirements

Both, the subnetwork or device to be modeled by a rational function as given in (2.3), or equivalently, by the state-space model as given in (2.4)-(2.5), and the equivalent model, must fulfill certain requirements for a realistic physical representation, such as time invariance, linearity, causality, stability, and passivity. These requirements are revisited next.

2.1.1 Time invariance

A system that produces an output signal $y(t)$ due the input signal $x(t)$ is time invariant if the response due to a time-shifted input $x(t-\tau)$ is also time-shifted by the same period interval [55]. The time-invariance property is illustrated in Figure 2.1.

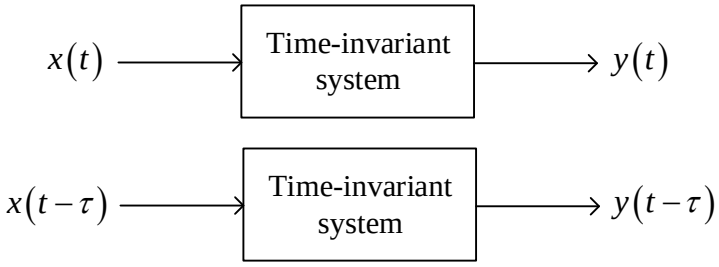

Figure 2.1. Time-invariant system.

2.1.2 Linearity

A given system is linear if it satisfies the superposition principle [55]. To recall the superposition principle, let us consider that a given system produces the output signals $y_1(t)$ and $y_2(t)$ due to the input signals $x_1(t)$ and $x_2(t)$, respectively. Then, the system is linear if it produces an output $y_1(t)+y_2(t)$ due to the input $x_1(t)+x_2(t)$. Also, the system must satisfy the scalability condition, i.e., if the system receives an input signal $kx(t)$, the output produced must be $ky(t)$, being k an arbitrary scalar value. The linearity property is illustrated in Figure 2.2.

The systems studied in this thesis are both linear and time invariant, which are usually referred in the literature as LTI systems.

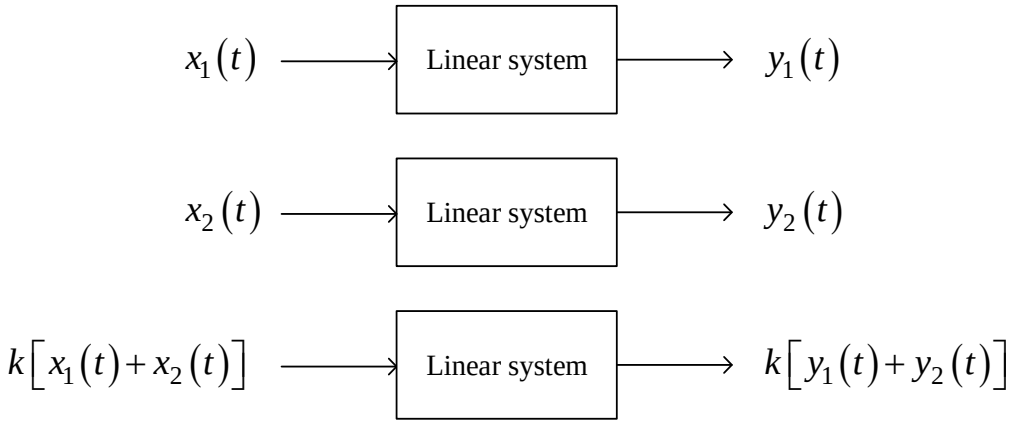

Figure 2.2. Responses of a linear system.

2.1.3 Causality

Another important property of the systems studied in this thesis is causality. An LTI system is causal if it produces output signals that only depend on instantaneous and past (history) values of the applied input signal(s). In other words, a causal system cannot anticipate the response due to future input values [55].

The time-domain output of a single-port LTI system is given by the convolution integral

$$y(t)=\int_{-\infty}^{+\infty} h(\tau)\,x(t-\tau)\,d\tau\,, \tag{2.7}$$

where $x(t)$ and $y(t)$ denote the input and output signals, respectively, and $h(t)$ denotes the impulse response of the system. For a causal system, $h(t)$ must respect the following condition

$$h(t)=0\,,\ \ \forall t<0\,. \tag{2.8}$$

Supossing that an input is applied to the system at time $t=0$, the causality condition in (2.8) ensures that the system will have null response for negative times in (2.7). For multiport systems, this condition applies to every element of the corresponding impulse response matrix, also referred in the literature as transfer matrix.

The bilateral Laplace transform of $h(t)$, denoted in this thesis as $H(s)$ is the transfer function

$$H(s)=\int_{-\infty}^{+\infty} h(t)\ e^{-st}dt\,. \tag{2.9}$$

It is recalled that the Laplace transform of any TD signal exists, if and only if, the integral given at the right side in (2.9) converges to a finite value. Thus, the Laplace transform of any signal may be defined for certain values of $s \in \mathbb{C}$ and not for others. The set of values of s for which the Laplace transform integral converges is known as the region of convergence (ROC).

For time-domain signals whose response is zero for $t < 0$, such as $h(t)$ of a causal system, the ROC only comprises the right half side of the complex plane ($\Re\{s\} > 0 : s \in \mathbb{C}$), the demonstration is given in Appendix B of this thesis. This condition implies that the transfer function $H(s)$ of a causal system must be defined for $\Re\{s\} > 0 : s \in \mathbb{C}$. Non-causal systems are unrealizable in real-life systems, and they are not considered in this thesis. Furthermore, the rational model studied in this thesis, as defined in (2.3), is always defined for $\Re\{s\} > 0 : s \in \mathbb{C}$. Moreover, when this model is discretized and implemented in time-domain simulations, the output of the model at every time-step is only dependent on past (history) and present values of the input(s). Thus, the system described by the rational model (2.3) is considered causal.

2.1.4 Stability

2.1.4.1 Input-output stability

An LTI system is said to be stable if for any magnitude-bounded input, defined as

$$|x(t)| < K < \infty, \quad \forall t, \tag{2.10}$$

a magnitude-bounded output is obtained at any time, i.e.,

$$|y(t)| < M < \infty, \quad \forall t, \tag{2.11}$$

where K and M are real scalar values. This condition is also known as BIBO (bounded-input bounded-output) stability [55].

The requirement for an LTI system to be BIBO stable is that its impulse response $h(t)$ must be bounded and finite as $t \to \infty$. This is equivalent to state that the impulse response of a BIBO system is integrable, i.e.,

$$\int_{-\infty}^{+\infty} h(t)\,dt < \infty . \tag{2.12}$$

This condition guarantees that for any bounded input $x(t)$ with finite duration (applied up to a certain time $t < \infty$), the output will be bounded and it will have a transient nature, i.e., it will vanish as $t \to \infty$.

The condition for BIBO stability given in (2.12), can be also analyzed in the frequency-domain by analyzing the Laplace-Transform ROC of $h(t)$. As demonstrated in Appendix B, the ROC of $h(t)$ of a causal system only includes the right-half complex plane without including the imaginary axis; however, if causality and BIBO stability features are combined, the ROC also includes the imaginary axis. The proof is also provided in Appendix B.

Then, a necessary condition for causal and BIBO stable systems is that the transfer function $H(s)$ or $\mathbf{H}(s)$ for multiport systems, must be defined, analytic and bounded for $\Re\{s\} \geq 0 : s \in \mathbb{C}$.

Note that in this section we use $\mathbf{H}(s)$ as a generic transfer function, although the transfer function studied in this thesis is an admittance-parameters matrix, denoted as $\mathbf{Y}(s)$.

2.1.4.2 Internal stability

Another (equivalent) stability analysis can be achieved in terms of the internal constitution of the state-space model as given in (2.4)-(2.5) or, equivalently, the rational model given in (2.3). The requirement for this model to be stable is that all the poles must have negative real part.

To demonstrate the importance of this fact, let us use a generic residue-pole element of the rational model (2.3) for an arbitrary entry of the generic transfer function $\mathbf{H}(s)$, i.e.

$$H(s) = \frac{r}{s-a} \tag{2.13}$$

and its time-domain representation (according to the inverse Laplace transform) as

$$h(t) = re^{at} . \tag{2.14}$$

Then, if a sinusoidal input is applied

$$u(t) = e^{j\omega_0 t}, \tag{2.15}$$

where ω_0 is the angular frequency, the resulting output becomes

$$y(t) = h(t) * u(t) = re^{at} * e^{j\omega_0 t}. \tag{2.16}$$

where $*$ denotes convolution.

From (2.16), it can be inferred that the requirement for the output $y(t)$ to be bounded is that the convoluted signals $h(t)$ and $u(t)$ must be both, bounded. Since the input signal has been set as a sinusoidal function, it is bounded. On the other hand, the condition for $h(t)$ to be bounded, considering the general case in which a is a complex value, is that the real part of a must be negative, otherwise, $h(t)$ would be an exponentially growing function (unbounded).

This condition can be alternatively analyzed from (2.14) as follows. If the real part of a is negative, the impulse response (2.14) vanishes for $t \to \infty$, such that $h(t)$ is integrable, satisfying the condition in (2.12) for BIBO stability.

2.1.5 Passivity

The most challenging requirement to fulfill when computing rational models, such as for FDNEs, is passivity. A passive system is defined as a system that can absorb energy at any time, but it can only deliver energy if some energy was previously stored in it, and this delivered energy cannot exceed the amount of energy previously stored in it at any time [56]. This definition can be analyzed in terms of power and energy as follows.

The instantaneous power absorbed by the dynamic system given in (2.4)-(2.5) is:

$$p(t) = \mathbf{v}(t)^T \mathbf{i}(t). \tag{2.17}$$

Based on (2.17), the cumulative energy absorbed by the system up to the arbitrary time t_a is

$$E(t) = \int_{-\infty}^{t_a} p(t)\, dt. \tag{2.18}$$

Then, according to the abovementioned definition, the system is passive if

$$E(t) \geq 0, \quad \forall t . \tag{2.19}$$

This definition is, however, useless in practice since it requires analyzing specific pairs of input and output signals, and it is impossible to analyze all the possible inputs to a given system. Also, it is important to consider that for a non-passive model, the time-domain simulation can be numerically unstable, such that output variables can be meaningless.

Alternatively, the instantaneous power entering a generic multiport system as given in (2.17) can be expressed in terms of frequency-domain variables, i.e.

$$p(t) = \Re\left\{\mathbf{V}(s)^H \mathbf{I}(s)\right\} = \Re\left\{\mathbf{V}(s)^H \mathbf{Y}(s)\mathbf{V}(s)\right\}. \tag{2.20}$$

where $\mathbf{V}(s)$ and $\mathbf{I}(s)$ are the vectors of voltages and currents, respectively, and $\mathbf{Y}(s)$ is the admittance matrix represented by a rational model. This expression can be rewritten as

$$p(t) = \Re\left\{\left|\mathbf{V}(s)^T\right| e^{s^* t} \mathbf{Y}(s) \left|\mathbf{V}(s)\right| e^{st}\right\}, \tag{2.21}$$

or, in a simpler form

$$p(t) = \Re\left\{\mathbf{u}^T \mathbf{Y}(s)\mathbf{u}\right\} e^{2\Re\{s\}t}, \tag{2.22}$$

where

$$\mathbf{u} = \left|\mathbf{V}(s)\right|. \tag{2.23}$$

Considering (2.22), the cumulative energy up to an arbitrary time t_a as defined in (2.18) is

$$E(t) = \int_{-\infty}^{t_a} p(t)\, dt = \Re\left\{\mathbf{u}^T \mathbf{Y}(s)\mathbf{u}\right\} \frac{e^{2\Re\{s\}t}}{2\Re\{s\}}, \tag{2.24}$$

where the condition $\Re\{s\} > 0$ must be respected to guarantee the integral's convergence. According to (2.19), the system represented by $\mathbf{Y}(s)$ is passive if and only if its cumulative energy is nonnegative at any time. From (2.24), it can be observed that neither the term $\frac{e^{2\Re\{s\}t}}{2\Re\{s\}}$, nor $\mathbf{u}$

can make $E(t) < 0$. Thus, the passivity condition relies on the nonnegative definiteness of the admittance matrix $\mathbf{Y}(s)$ [56]. This condition can be mathematically defined as

$$\frac{1}{2}\left[\mathbf{Y}(s) + \mathbf{Y}(s)^H\right] \geq 0, \quad \Re\{s\} > 0. \tag{2.25}$$

The left side of the inequality in (2.25) denotes the Hermitian part of $\mathbf{Y}(s)$. In the case of $\mathbf{Y}(s)$ being symmetric, the Hermitian part of $\mathbf{Y}(s)$ is equal to its real part, or equivalently the conductance matrix $\mathbf{G}(s)$. From (2.25), it can be stated that a multiport system represented by the admittance matrix $\mathbf{Y}(s)$ is passive if and only if its Hermitian part is nonnegative definite for the right-half side of the complex plane.

The nonnegative definiteness of $\mathbf{Y}(s)$ as indicated in (2.25) is equivalent to requiring the Hermitian part of $\mathbf{Y}(s)$ to have all its eigenvalues nonnegative, i.e.,

$$\text{eig}\left\{\mathbf{Y}(s) + \mathbf{Y}(s)^H\right\} \geq 0, \quad \forall \Re\{s\} > 0. \tag{2.26}$$

2.1.6 Positive real matrix theorem

So far, the conditions for causality, stability, and passivity of rational models based on the Laplace transform have been revisited. These conditions can be equivalently verified using the Fourier transform [56, 57], which is a particular case of the Laplace transform where the real part of the complex variable $s = \sigma + j\omega$ is zero, i.e., $s = j\omega$. Using the Fourier transform the conditions for causality, stability and passivity stand as for the Laplace domain, but they must be fulfilled only for the imaginary axis, i.e., $s = j\omega$, instead of all the right-half complex plane.

Considering the Fourier transform, the positive real theorem for rational matrices englobes the previously studied conditions for causality, stability and passivity as follows.

A rational matrix represented by $\mathbf{Y}(s)$, where $s = j\omega$, is positive real if and only if

1. $\mathbf{Y}(s)$ is defined and analytic for $\omega \geq 0$
2. $\mathbf{Y}(s)$ does not contain poles in the right half complex plane.

3. $\mathbf{Y}(s)^{*} = \mathbf{Y}(-s)$

4. $\mathbf{Y}(s) + \mathbf{Y}(s)^{H} \geq 0, \quad \forall \omega \in \mathbb{R}$

5. $\mathbf{Y}(s) \to s\mathbf{E}$ when $s \to \infty$, $\mathbf{E}$ being constant, real, symmetric and nonnegative definite.

A quick analysis of the positive real matrix theorem reveals that the first and second points imply stability and causality of the rational model denoted by $\mathbf{Y}(s)$; the third point guarantees that the impulse response is only real; the fourth point is the requirement for the rational model to be passive; finally, the fifth point establishes the asymptotic behaviour of the system.

Then, the positive real theorem summarizes the requirements of rational models for stable, causal and passive characterization of LTI systems, as required for FDNE modeling. Each point of this theorem is, however, not necessarily tested when computing a rational model. The fitting techniques studied in this thesis guarantee the symmetry of the model; also, the generated poles are forced to have negative real part. On the other hand, the nonnegative definiteness of the model (fourth point), which is the condition for passivity, cannot be guaranteed.

It is important to mention that the positive real theorem stands for rational model without purely imaginary poles, such case requires a special treatment [56]. The methodologies presented in this thesis do not produce rational models with purely imaginary poles.

2.1.7 Positive real lemma

The positive real lemma gives an alternative method for evaluating the passivity of a state-space model from a point of view of dissipative energy. Let us consider a generic function $V(\mathbf{x}(t))$ as the function of the energy storage by a system at any time. According to (2.18), the change of energy (or cumulative energy) in the system for a period of time $[t_0 \quad t_1]$ can be expressed as

$$V[\mathbf{x}(t_1)] - V[\mathbf{x}(t_0)] \leq \int_{t_0}^{t_1} p(t)\, dt = E(t_1) - E(t_0), \quad \forall\ t_0 \leq t_1 \tag{2.27}$$

where $\mathbf{x}(t)$ denotes the state vector of the state-space model under study. Equation (2.27) implies that the energy stored during a given period of time can never exceed the cumulative energy $E(t)$ during that period. This definition is consistent with the passivity definition given in section 2.1.5.

Then, dividing (2.27) by the time interval $(t_1 - t_0) \to 0$ the following expression is obtained

$$\frac{dV\left[\mathbf{x}(t)\right]}{dt} \le p(t). \tag{2.28}$$

According to the Lyapunov stability criterion [56], it is sufficient to consider the quadratic storage function

$$V\left[\mathbf{x}(t)\right] = \mathbf{x}(t)^T \mathbf{P}\mathbf{x}(t) \quad : \mathbf{P} = \mathbf{P}^T > 0 \tag{2.29}$$

to evaluate the system passivity. Then, the derivative of (2.29), as required in the left side of (2.28) becomes

$$\frac{dV\left[\mathbf{x}(t)\right]}{dt} = \frac{1}{2}\left(\dot{\mathbf{x}}^T(t)\mathbf{P}\mathbf{x}(t) + \mathbf{x}(t)^T \mathbf{P}\dot{\mathbf{x}}(t)\right), \tag{2.30}$$

and the power absorbed by the system, as given at the right side of (2.28) can be expressed as

$$p(t) = \frac{1}{2}\left[\mathbf{v}(t)^T \mathbf{i}(t) + \mathbf{i}(t)^T \mathbf{v}(t)\right]. \tag{2.31}$$

Substituting (2.30) and (2.31) in (2.28) results into

$$\dot{\mathbf{x}}^T(t)\mathbf{P}\mathbf{x}(t) + \mathbf{x}(t)^T \mathbf{P}\dot{\mathbf{x}}(t) \le \mathbf{v}(t)^T \mathbf{i}(t) + \mathbf{i}(t)^T \mathbf{v}(t), \tag{2.32}$$

Substituting the state-space model equations (2.4) and (2.5) in (2.32), the inequality becomes

$$\left[\mathbf{A}\mathbf{x} + \mathbf{B}\mathbf{v}\right]^T \mathbf{P}\mathbf{x} + \mathbf{x}^T\mathbf{P}\left[\mathbf{A}\mathbf{x} + \mathbf{B}\mathbf{v}\right] \le \mathbf{v}^T\left[\mathbf{C}\mathbf{x} + \mathbf{D}\mathbf{v}\right] + \left[\mathbf{C}\mathbf{x} + \mathbf{D}\mathbf{v}\right]^T \mathbf{v}. \tag{2.33}$$

After some algebraic manipulations, (2.33) can be written as

$$\begin{bmatrix}\mathbf{x}^T & \mathbf{v}^T\end{bmatrix}\begin{bmatrix}\mathbf{A}^T\mathbf{P} + \mathbf{P}\mathbf{A} & \mathbf{P}\mathbf{B} - \mathbf{C}^T \\ \mathbf{B}^T\mathbf{P} - \mathbf{C} & -\left(\mathbf{D} + \mathbf{D}^T\right)\end{bmatrix}\begin{bmatrix}\mathbf{x} \\ \mathbf{v}\end{bmatrix} \le 0. \tag{2.34}$$

Finally, considering (2.34) and the constraint condition $\mathbf{P} = \mathbf{P}^T > 0$ in (2.29), the positive real lemma is derived as follows:

The system described by the state space model (2.4)-(2.5) is passive, if and only if

$$\exists \mathbf{P} = \mathbf{P}^T > 0 \quad \text{such that} \quad \begin{bmatrix} \mathbf{A}^T\mathbf{P} + \mathbf{P}\mathbf{A} & \mathbf{P}\mathbf{B} - \mathbf{C}^T \\ \mathbf{B}^T\mathbf{P} - \mathbf{C} & -\left(\mathbf{D} + \mathbf{D}^T\right) \end{bmatrix} \leq 0 \,. \tag{2.35}$$

Both, the positive real matrix theorem and the positive real lemma, give sufficiency conditions to claim passivity of rational models.

2.2 Conclusions

This chapter presents an overview on the physical and mathematic requirements for rational modeling, such as linearity, causality, stability and passivity. As it is studied in this chapter, the most challenging requirement to fulfill is passivity, which can be guaranteed if the rational model respects the positive real matrix theorem or the positive real lemma, which give sufficient conditions for passivity.

CHAPTER 3 RATIONAL MODELING TECHNIQUES

3.1 Fitting techniques

In this section, the theories of Vector Fitting (VF), Matrix Pencil Method (MPM), and Loewner matrix (LM) techniques are reviewed. This review sets the basis for further studies about fitting presented in Chapter 4.

3.1.1 Vector Fitting Technique

To start with the analysis of the VF method, the fitting of a generic scalar function $f(s)$ is first analyzed. This case is equivalent to the fitting of the frequency-response of a single-port system. The corresponding fitted model (scalar case of (2.3)) is

$$f_{fitted}(s) = \sum_{n=1}^{N} \frac{r_n}{s - a_n} + d + se. \tag{3.1}$$

The VF technique computes the rational model (3.1) in two stages. In the first stage, the poles of the system (a_n) are computed, in the second stage, the residues r_n, and asymptotic terms d and e are obtained.

3.1.1.1 Poles computation

In the first stage of the original VF technique [19], the poles of the system are obtained in an iterative relocation process from an initial (guessed) set of poles, denoted in this thesis as $\bar{a}_n$. As for this first version of the VF technique, VF introduces the auxiliary function

$$\sigma(s) = \sum_{n=1}^{N} \frac{c_n}{s - \bar{a}_n} + 1, \tag{3.2}$$

to create the augmented problem

$$\left(\sum_{n=1}^{N} \frac{r_n}{s - \bar{a}_n} + d + se \right) = \left(\sum_{n=1}^{N} \frac{c_n}{s - \bar{a}_n} + 1 \right) f(s), \tag{3.3}$$

The expression given in (3.3) suggests that the initial approximation (as given by the left side) equals the function being fitted $f(s)$ with the factor $\sigma(s)$ multiplied. Thus, the auxiliary function $\sigma(s)$ can be interpreted as the error of the approximation. The VF technique first identifies $\sigma(s)$ to finally extract it from (3.3) to obtain a more refined set of poles.

Evaluating (3.3) for the given set frequency samples as indicated in (2.2), permits obtaining an overdetermined system of equations of the form

$$\mathbf{M}\mathbf{w} = \mathbf{q}, \tag{3.4}$$

where the k^{th} row of $\mathbf{M}$ is

$$\mathbf{M}_k = \left[\frac{1}{s_k - \bar{a}_1} \quad \cdots \quad \frac{1}{s_k - \bar{a}_N} \quad 1 \quad s_k \quad \frac{-f(s_k)}{s_k - \bar{a}_1} \quad \cdots \quad \frac{-f(s_k)}{s_k - \bar{a}_N} \right], \tag{3.5}$$

the unknowns' vector $\mathbf{w}$ is

$$\mathbf{w} = \left[r_1 \quad \cdots \quad r_N \quad d \quad e \quad c_1 \quad \cdots \quad c_N \right]^T, \tag{3.6}$$

and vector $\mathbf{q}$ is

$$\mathbf{q} = f(s). \tag{3.7}$$

where $f(s)$ denotes the function being fitted with a finit number of samples.

The solution of (3.4) is achieved as follows. First, matrix $\mathbf{M}$ in (3.4) is decomposed by applying QR factorization, i.e.,

$$\mathbf{M} = \mathbf{Q}\mathbf{R}, \tag{3.8}$$

where $\mathbf{Q}$ is a unitary matrix, i.e., $\mathbf{Q}^{-1} = \mathbf{Q}^H$, and $\mathbf{R}$ is an upper triangular matrix. This factorization permits reformulating (3.4) as

$$\mathbf{R}\mathbf{w} = \mathbf{n}, \tag{3.9}$$

where

$$\mathbf{n} = \mathbf{Q}^H \mathbf{q}. \tag{3.10}$$

After this reformulation, it can be inferred that (3.9) has the following structure

$$\begin{bmatrix} \mathbf{R}_{11} & \mathbf{R}_{12} \\ \mathbf{0} & \mathbf{R}_{22} \end{bmatrix} \begin{bmatrix} \mathbf{w}_1 \\ \mathbf{w}_2 \end{bmatrix} = \begin{bmatrix} \mathbf{n}_1 \\ \mathbf{n}_2 \end{bmatrix}, \tag{3.11}$$

where vector $\mathbf{w}_1$ contains the residues r_n, d and e coefficients, and $\mathbf{w}_2$ contains the coefficients c_n corresponding to the numerator of $\sigma(s)$ in (3.2). Since the coefficients of $\mathbf{w}_1$ are not required for the identification of $\sigma(s)$, only the independent subsystem of equations

$$\mathbf{R}_{22}\mathbf{w}_2 = \mathbf{n}_2, \tag{3.12}$$

needs to be solved.

By solving (3.12), the auxiliary function $\sigma(s)$ becomes fully identified. The next step to calculate an improved set of poles consists of the extraction of $\sigma(s)$ from (3.3). Considering that the functions within parentheses in (3.3) can be expressed as a ratio of two polynomial functions, (3.3) can be rewritten as

$$\begin{bmatrix} \prod_{n=1}^{N+1}(s-z_n) \\ e\dfrac{n=1}{\prod_{n=1}^{N}(s-\bar{a}_n)} \end{bmatrix} = \begin{bmatrix} \prod_{n=1}^{N}(s-\bar{z}_n) \\ \dfrac{n=1}{\prod_{n=1}^{N}(s-\bar{a}_n)} \end{bmatrix} f(s), \tag{3.13}$$

where the coefficients z_k and $\bar{z}_k$ are the zeros of the initial approximation and of the auxiliary function $\sigma(s)$, respectively. Isolating $f(s)$ in (3.13), the following expression is obtained

$$f(s) = \begin{bmatrix} \prod_{n=1}^{N+1}(s-z_n) \\ e\dfrac{n=1}{\prod_{n=1}^{N}(s-\bar{z}_n)} \end{bmatrix} = \sum_{n=1}^{N} \frac{r_n}{s-\bar{z}_n} + d + se\,. \tag{3.14}$$

From (3.14), it is observed that the initial poles $\bar{a}_n$ become replaced by the coefficients $\bar{z}_n$, i.e., the new set of poles is given by the zeros of $\sigma(s)$.

An initial set of poles can be easily obtained by using *N* uniformly- or logarithmically-spaced samples of the fitting frequency band.

Considering $\sigma(s)$ known (from the solution of (3.12)) in the from of (3.2), $\sigma(s)$ must be transformed to the required zeros/poles form as given at the right side of (3.13). To do so, $\sigma(s)$ is first expressed as a state-space model following the rational- to state-space-model transformation given in Appendix A. The resulting state-space model is

$$\dot{\tilde{\mathbf{x}}}(t) = \tilde{\mathbf{A}}\tilde{\mathbf{x}}(t) + \tilde{\mathbf{b}}\tilde{u}(t), \tag{3.15}$$

$$\tilde{y}(t) = \tilde{\mathbf{c}}\tilde{\mathbf{x}}(t) + \tilde{u}(t). \tag{3.16}$$

Inverting the input and output of the state-space model (3.15)-(3.16) results in

$$\dot{\tilde{\mathbf{x}}}(t) = \left(\tilde{\mathbf{A}} - \tilde{\mathbf{b}}\tilde{\mathbf{c}}\right)\tilde{\mathbf{x}}(t) + \tilde{\mathbf{b}}\tilde{y}(t), \tag{3.17}$$

$$\tilde{u}(t) = -\tilde{\mathbf{c}}\tilde{\mathbf{x}}(t) + \tilde{y}(t). \tag{3.18}$$

Then, the zeros of $\sigma(s)$, or equivalently, the new set of poles, are computed as the eigenvalues of the state-matrix in (3.17), i.e.,

$$\bar{\mathbf{z}} = \mathrm{eig}\left(\tilde{\mathbf{A}} - \tilde{\mathbf{b}}\tilde{\mathbf{c}}\right). \tag{3.19}$$

The outlined process is repeated iteratively for a predefined number of iterations or until reaching a certain convergence criterion (for instance by selecting a RMS error limit). A further study about the required number of iterations is presented later in Chapter 5, section 5.1.

3.1.1.2 Residues and asymptotic terms computation

For the second stage of the VF method, the poles of the system (a_n) are known. Then, the residues r_n, and asymptotic terms d and e are obtained by solving an overdetermined system of equations of the form

$$\mathbf{N}\mathbf{v} = \mathbf{k}, \tag{3.20}$$

where the k^{th} row of $\mathbf{N}$ is

$$\mathbf{N}_k = \left[\frac{1}{s_k - a_1} \quad \cdots \quad \frac{1}{s_k - a_N} \quad 1 \quad s_k\right], \tag{3.21}$$

the unknowns' vector $\mathbf{v}$ is

$$\mathbf{v} = \begin{bmatrix} r_1 & \cdots & r_N & d & e \end{bmatrix}^T, \tag{3.22}$$

and $\mathbf{k}$ constains the samples of the frequency response being fitted

$$\mathbf{k} = f(s). \tag{3.23}$$

Solving (3.20) via least-squares method, the fitting of the scalar function $f(s)$ is completed and the single-port model (3.1) is obtained.

3.1.1.3 Relaxed Vector Fitting

An improved version of the VF method, named 'relaxed VF' [58], consists of using the auxiliary function

$$\sigma(s) = \sum_{n=1}^{N} \frac{c_n}{s - \bar{a}_n} + \tilde{d}, \tag{3.24}$$

where $\tilde{d}$ is a real value, instead of (3.2). Using (3.24), the system of equations (3.4) requires the coefficient $\tilde{d}$ to be included into the unknowns' vector $\mathbf{w}$, defined in (3.6). At the same time, this causes the $\mathbf{q}$ vector in (3.4) to be a zero vector. To avoid a trivial solution of (3.4), the equation

$$\mathrm{Re}\left\{ \sum_{k=1}^{N_s} \left(\sum_{n=1}^{N} \frac{c_n}{s_k - \bar{a}_n} + \tilde{d} \right) \right\} = N_s, \tag{3.25}$$

is included into the system of equations (3.4).

Then, for the relaxed VF method, the k^{th} row of $\mathbf{M}$, with $k < (N_s + 1)$, in (3.4) becomes

$$\mathbf{M}_k = \left[\frac{1}{s_k - \bar{a}_1} \quad \cdots \quad \frac{1}{s_k - \bar{a}_N} \quad 1 \quad s_k \quad \frac{-f(s_k)}{s_k - \bar{a}_1} \quad \cdots \quad \frac{-f(s_k)}{s_k - \bar{a}_N} \quad -f(s_k) \right]; \tag{3.26}$$

the last row of $\mathbf{M}$ (corresponding to (3.25)) is

$$\mathbf{M}_{N_s+1} = \left[0 \quad \cdots \quad 0 \quad 0 \quad 0 \quad \sum_{k=1}^{N_s} \frac{1}{s_k - \bar{a}_1} \quad \cdots \quad \sum_{k=1}^{N_s} \frac{1}{s_k - \bar{a}_N} \quad N_s \right]; \tag{3.27}$$

the unknowns' vector becomes

$$\mathbf{w} = \begin{bmatrix} r_1 & \cdots & r_N & d & e & c_1 & \cdots & c_N & \tilde{d} \end{bmatrix}^T; \tag{3.28}$$

and vector $\mathbf{q}$ becomes

$$\mathbf{q} = \begin{bmatrix} 0 & \cdots & 0 & N_s \end{bmatrix}^T. \tag{3.29}$$

As for the relaxed VF approach, the methodology explained before to identify the auxiliary function $\sigma(s)$ is also applied with the following slight modification, the new poles at each iteration are computed as

$$\bar{\mathbf{z}} = \text{eig}\left(\tilde{\mathbf{A}} - \tilde{\mathbf{b}}\tilde{d}^{-1}\tilde{\mathbf{c}}\right). \tag{3.30}$$

The second stage of VF is not modified, i.e., residues and asymptotic components of the rational model are computed as described in section 3.1.1.2. The relaxed VF approach is said to be more robust than the initially proposed VF method [58].

3.1.1.4 Fitting of multiport systems by Vector Fitting

For the fitting of multiport systems, the VF method, as its name indicates, does not fit matrices. Then, assuming the admittance matrix (2.1) is symmetric, the VF technique first stacks the elements of the lower triangular part of this matrix to form a vector, i.e.,

$$\mathbf{f}(s) = \begin{bmatrix} \underbrace{y_{11}(s) & \cdots & y_{p1}(s)}_{1^{\text{st}}\text{ column}} & \underbrace{y_{22}(s) & \cdots & y_{p2}(s)}_{2^{\text{nd}}\text{ column}} & \cdots & \underbrace{y_{pp}(s)}_{\cdots\ p^{\text{th}}\text{ column}} \end{bmatrix}, \tag{3.31}$$

As it can be deducted from (3.31), the number of elements of $\mathbf{f}(s)$ is

$$N_e = p(p+1)/2. \tag{3.32}$$

Note that for the fitting of $\mathbf{f}(s)$, equation (3.3) stands for every element of $\mathbf{f}(s)$. Then, the subsystems of equations (3.12) corresponding to every element of $\mathbf{f}(s)$ are assembled and solved to identify the corresponding auxiliary function $\sigma(s)$. The improved set of poles is obtained from the solution of (3.19) or (3.30) for the traditional or the relaxed VF, respectively. The pole relocation process is repeated iteratively as for the scalar case. Note that a common set of poles is

obtained for all the elements of $\mathbf{f}(s)$. Finally, the residues and asymptotic terms are obtained solving (3.20) for each element of $\mathbf{f}(s)$.

Once the rational models for the elements of $\mathbf{f}(s)$ have been obtained, the elements above the diagonal of the fitted matrix are repeated according to the symmetry of the fitted matrix to obtain the complete matrix rational model (2.3).

An alternative approach for the fitting of multiport systems (matrices), is the so-called column-wise approach. The column-wise fitting approach consists of fitting each column of the input admittance matrix as explained above for $\mathbf{f}(s)$. Under this approach, a common set of poles is obtained for the elements of each column of the fitted matrix. Finally, the individual rational models are arranged accordingly to obtain (2.3). Using the column-wise fitting approach, however, the symmetry of the model is not preserved.

3.1.2 Matrix Pencil Method

3.1.2.1 MPM in the time-domain

The original MPM technique, as presented in [27], consists of the identification of a system by approximating its transient response $y(t)$ in discrete form as a sum of complex exponentials, i.e.,

$$y(k\Delta t) = \sum_{n=1}^{N} r_n e^{a_n k\Delta t} \,. \tag{3.33}$$

where coefficients r_n and a_n are equivalent to the residues and poles as in (3.1), respectively, when applying the inverse Laplace transform to the individual rational elements in (3.1).

The MPM technique computes the poles a_n by solving the generalized eigenvalue problem:

$$\mathbf{Y}_1\mathbf{r}_n = \lambda_n \mathbf{Y}_2\mathbf{r}_n \,. \tag{3.34}$$

Note that (3.34) can be alternatively solved as

$$\left[\mathbf{Y}_2^{\dagger}\mathbf{Y}_1 - \lambda_n \mathbf{I}\right]\mathbf{r}_n = 0 \,, \tag{3.35}$$

where λ_n and $\mathbf{r}_n$ denote the n^{th} eigenvalue and right eigenvector, respectively; † denotes the Moore-Penrose pseudoinverse; $\mathbf{I}$ denotes the identity matrix; and $\mathbf{Y}_1$, $\mathbf{Y}_2$ are the pencil matrices, defined as

$$\mathbf{Y}_1 = \begin{bmatrix} y_1 & y_2 & \cdots & y_L \\ y_2 & y_3 & \cdots & y_{L+1} \\ \vdots & \vdots & \ddots & \vdots \\ y_{N_t-L} & y_{N_t-L+1} & \cdots & y_{N_t-1} \end{bmatrix}, \tag{3.36}$$

$$\mathbf{Y}_2 = \begin{bmatrix} y_0 & y_1 & \cdots & y_{L-1} \\ y_1 & y_2 & \cdots & y_L \\ \vdots & \vdots & \ddots & \vdots \\ y_{N_t-L-1} & y_{N_t-L} & \cdots & y_{N_t-2} \end{bmatrix}, \tag{3.37}$$

where $y_1,...,y_{N_t}$ denote the samples of the transient response $y(t)$, and L denotes the pencil term, usually defined as

$$L = N_t/2\,, \tag{3.38}$$

with N_t being the number of samples of $y(t)$.

Using the MPM approach, the terms $e^{a_n \Delta t}$ at the right side of (3.33) are found as the eigenvalues λ_n in (3.35), i.e.,

$$\lambda_n = e^{a_n \Delta t}\,, \tag{3.39}$$

such that the poles of the rational model are computed from the solution of (3.35) and (3.39) as

$$a_n = \log_e(\lambda_n)/\Delta t\,, \tag{3.40}$$

3.1.2.2 Model order identification via MPM

To obtain the appropriate order of the rational approximation N as in (2.3), singular value decomposition (SVD) is applied to the pencil matrices, i.e.,

$$\mathbf{Y}_1 = \mathbf{U}_1 \mathbf{Z}_1 \mathbf{V}_1\,. \tag{3.41}$$

$$\mathbf{Y}_2 = \mathbf{U}_2 \mathbf{Z}_2 \mathbf{V}_2\,. \tag{3.42}$$

where $\mathbf{Z}_1$ and $\mathbf{Z}_2$ are diagonal matrices containing the singular values z_i in descending order according to its magnitude; $\mathbf{U}_1$, $\mathbf{U}_2$ and $\mathbf{V}_1$, $\mathbf{V}_2$ are matrices containing the left-singular and right-singular vectors, respectively.

To identify the model order, the singular values are normalized by the largest one, i.e.,

$$\overline{z}_i = z_i / z_1 . \tag{3.43}$$

The appropriate model order can be determined by identifying an abrupt drop between consecutive singular values. The singular values above this abrupt drop are considered as dominant, and the number of them denotes the model order N.

Another strategy for model order determination is to consider as dominant singular values those with magnitude above a predefined threshold value ξ. In this case, the threshold value ξ determines the fitting order N. Alternatively, if the function order is known beforehand, the first N singular values can be selected directly to compute the solution of (3.35) as follows.

Considering only the *N* dominant singular values revealed in (3.41) and (3.42), equation (3.35) can be equivalently solved as

$$\left[\hat{\mathbf{V}}_2^{\dagger}\hat{\mathbf{V}}_1 - \lambda_n \mathbf{I}\right]\mathbf{r}_n = 0 , \tag{3.44}$$

where $\hat{\mathbf{V}}_1$ and $\hat{\mathbf{V}}_2$ are matrices containing only the N dominant right-singular vectors of $\mathbf{V}_1$ and $\mathbf{V}_2$ as given in (3.41) and (3.42), respectively.

For a noise-contaminated transient response $y(t)$, the total-least-squares matrix pencil

$$\mathbf{M} = \begin{bmatrix} y_0 & y_1 & \cdots & y_L \\ y_1 & y_2 & \cdots & y_{L+1} \\ \vdots & \vdots & \ddots & \vdots \\ y_{N_t-L-1} & y_{N_t-L} & \cdots & y_{N_t-1} \end{bmatrix} \tag{3.45}$$

can be used instead of $\mathbf{Y}_1$ and $\mathbf{Y}_2$ [27]. In this case, the corresponding SVD is applied to $\mathbf{M}$ as

$$\mathbf{M} = \mathbf{UZV} \tag{3.46}$$

and the system's pencil eigenvalues are calculated by solving (3.44), with

$$\hat{\mathbf{V}}_1 = \begin{bmatrix} v_1 & v_2 & \cdots & v_{N-1} \end{bmatrix}, \tag{3.47}$$

$$\hat{\mathbf{V}}_2 = \begin{bmatrix} v_2 & v_3 & \cdots & v_N \end{bmatrix}, \tag{3.48}$$

where $v_{1,2,\ldots N}$ denote the dominant right-singular eigenvectors (columns of $\mathbf{V}$) from (3.46). This approach is later adopted in Chapter 4 for numerical studies.

Once the poles of the approximation are known, either by using ($\mathbf{Y}_1$ and $\mathbf{Y}_2$) or $\mathbf{M}$, the residues r_n, and asymptotic coefficients d and e as given in (3.1) are calculated solving the least-squares problem as indicated in section 3.1.1.2, as for the VF technique.

3.1.2.3 MPM in the frequency domain

Because the outlined original MPM technique uses a transient response as input, the frequency-domain application requires the transformation of the input frequency-response to the time-domain [31, 32]. This transformation can be achieved, for instance, by applying the Closed-Form Inverse Fourier Transform (CFIFT) as reported in [32]. However, using the CFIFT, the MPM approximation must be applied twice, i.e., first in the frequency-domain and then in the time-domain [32]. Alternatively, the outlined transformation can be achieved via the Inverse Fast Fourier Transform (IFFT). This approach requires a single application of the MPM technique, thus, accelerating the fitting process. In this thesis, the IFFT is applied via the built-in Matlab [54] function *IFFT*. Since the application of the *IFFT* algorithm requires the number of samples to be a power of two for efficient computation, in this thesis, this number is calculated as

$$N_t = 2^{nextpow2(N_s)+m}, \tag{3.49}$$

where the operator *nextpow2* calculates the next power of base two of its argument, in this case the number of frequency-domain samples N_s; and m is an integer number that is added to ensure an accurate time-domain function representation. Note that the number of samples of the resulting time-domain function is N_t. As it is demonstrated later in Chapter 4, in most cases a number $m > 0$ is necessary for an accurate curve fitting. Moreover, as it will be shown in Chapter 4, this transformation plays a very important role in the fitting process for the MPM technique.

The abovementioned TD to FD transformation delimits the MPM technique to only linearly-spaced sampled functions for the fitting of FD functions, unless, some interpolation technique is used.

3.1.2.4 Fitting of multiport systems via MPM

To address the fitting of multiport systems, the above described MPM technique formulated in FD can be applied to each element of the matrix function (2.1), obtaining individual rational models. Then, individual rational models can be assembled for obtaining a matrix-format rational model as given by (2.3). This approach is however, impractical since each element will have a different set of poles, resulting in a state-space model with very large dimensions.

Considering that the diagonal elements of an admittance matrix are equal to the sum of all the branches' admittances connected to the nodes of the network, all the information related to the system is contained in the trace of the admittance matrix. Taking advantage of this fact the trace of the matrix function (2.1) is used in this thesis as input for the MPM technique in FD. Finally, the residues r_n, and asymptotic terms d and e are obtained as for the VF technique.

3.1.3 Loewner Matrix Technique

The LM fitting technique [59] uses the input admittance matrix (2.1) and the frequency samples (2.2), together with tangential interpolation data to construct the state-space model:

$$\mathbf{Q}\dot{\mathbf{x}}(t) = \mathbf{A}\mathbf{x}(t) + \mathbf{B}\mathbf{u}(t), \tag{3.50}$$

$$\mathbf{y}(t) = \mathbf{C}\mathbf{x}(t) + \mathbf{D}\mathbf{u}(t) + \mathbf{Y}^{\infty}\dot{\mathbf{u}}(t), \tag{3.51}$$

where $\mathbf{Q}$, $\mathbf{A} \in \mathbb{R}^{N\times N}$, $\mathbf{B} \in \mathbb{R}^{N\times p}$, $\mathbf{C} \in \mathbb{R}^{p\times N}$, $\mathbf{x} \in \mathbb{R}^{N\times 1}$, $\mathbf{y} \in \mathbb{R}^{p\times 1}$, $\mathbf{D}, \mathbf{Y}^{\infty} \in \mathbb{R}^{p\times p}$, with p being the number of inputs/outputs of the system and N the number of states. The outlined state-space model is obtained from the application of SVD to the Loewner matrix pencil function as follows:

$$\mathbf{\Lambda\Sigma\Psi} = \mathrm{SVD}\left(x\mathbf{L} - \mathbf{L}'\right), \tag{3.52}$$

where x can be set as any sample of the complex frequency (s_k) as given in (2.2); and $\mathbf{L}$, $\mathbf{L}'$ denote the Loewner and shifted-Loewner matrices, respectively. The only requirement for the selection of x is that it should not reduce the rank of the pencil function, i.e. $x \in s, \notin \mathrm{eig}\left(\mathbf{L}, \mathbf{L}'\right)$.

The Loewner and shifted-Loewner matrices are computed as

$$\mathbf{L}_{ij} = \frac{\mathbf{\Phi}_j\mathbf{r}_i - \mathbf{l}_j\mathbf{\Omega}_i}{\mu_j - \lambda_i}, \tag{3.53}$$

$$\mathbf{L}'_{ij} = \frac{\mu_j \boldsymbol{\Phi}_j \mathbf{r}_i - \lambda_i \mathbf{l}_j \boldsymbol{\Omega}_i}{\mu_j - \lambda_i}, \tag{3.54}$$

where the sets $\left\{\mu_j, \mathbf{l}_j, \boldsymbol{\Phi}_j\right\}$ and $\left\{\lambda_i, \mathbf{r}_i, \boldsymbol{\Omega}_i\right\}$ denote the left and right interpolation data, respectively. Tangential interpolation data can be obtained partitioning the input frequency samples in different manners, one of them is presented next.

According to [59], the input admittance matrix frequency-response and frequency samples are partitioned as follows:

$$\mu = \begin{bmatrix} s_1 & s_1^* & s_3 & s_3^* & \cdots & s_{N_s-1} & s_{N_s-1}^* \end{bmatrix}, \tag{3.55}$$

$$\lambda = \begin{bmatrix} s_2 & s_2^* & s_4 & s_4^* & \cdots & s_{N_s} & s_{N_s}^* \end{bmatrix}, \tag{3.56}$$

$$\boldsymbol{\Phi}_j = \mathbf{l}_j \mathbf{Y}\left(\mu_j\right), \tag{3.57}$$

$$\boldsymbol{\Omega}_i = \mathbf{Y}\left(\lambda_i\right)\mathbf{r}_i, \tag{3.58}$$

$$\mathbf{P} = \begin{bmatrix} \boldsymbol{\Phi}_1^T & \cdots & \boldsymbol{\Phi}_j^T & \cdots \end{bmatrix}^T, \tag{3.59}$$

$$\mathbf{W} = \begin{bmatrix} \boldsymbol{\Omega}_1 & \cdots & \boldsymbol{\Omega}_i & \cdots \end{bmatrix}, \tag{3.60}$$

where $\mathbf{Y}$ denotes the matrix function (2.1) to be fitted and $\mathbf{l}_j$, $\mathbf{r}_i$ are referred as left and right tangential directions, respectively. Tangential directions can be given in vector or matrix format, commonly referred in the literature as VFTI (vector-format tangential interpolation) or MFTI (matrix-format tangential interpolation) [59].

VFTI data can be obtained as follows:

$$\mathbf{l}_{2n-1} = \mathbf{l}_{2n} = \mathbf{I}_k, \tag{3.61}$$

$$\mathbf{r}_{2n-1} = \mathbf{r}_{2n} = \left(\mathbf{I}_k\right)^T, \tag{3.62}$$

where $n = 1, \cdots, N_s/2$, and $\mathbf{I}_k$ denotes the k^{th} column of the identity matrix of size $p \times p$. Index k is set as follows: if $\operatorname{mod}\left(n/p\right) = 0$, $k = n$; else, $k = \operatorname{mod}\left(n/p\right)$.

As for MFTI data, both, $\mathbf{l}_j$ and $\mathbf{r}_i$, are identity matrices.

The state-space model matrices given in (3.50)-(3.51) are finally computed as follows:

$$\mathbf{Q} = -\boldsymbol{\Lambda}_r^* \mathbf{L} \boldsymbol{\Psi}_r, \tag{3.63}$$

$$\mathbf{A} = -\boldsymbol{\Lambda}_r^* \mathbf{L}' \boldsymbol{\Psi}_r, \tag{3.64}$$

$$\mathbf{B} = \boldsymbol{\Lambda}_r^* \mathbf{P}_r, \tag{3.65}$$

$$\mathbf{C} = \mathbf{W}_r \boldsymbol{\Psi}_r, \tag{3.66}$$

where the subscript r denotes that only the N columns related to the dominant singular values revealed in (3.52) are considered. The dominant singular values are selected as explained in Section 3.1.2.2 for the MPM technique. The number of dominant singular values also determines the number of states (N) of the state-space model given in (3.50)-(3.51).

At this stage, matrices $\mathbf{D}$ and $\mathbf{Y}^{\infty}$ in (3.51) remain unknown, but they are embedded into $\mathbf{Q}$, $\mathbf{A}$, $\mathbf{B}$ and $\mathbf{C}$. Moreover, since $\mathbf{Y}^{\infty}$ contains unstable modes, it must be extracted from the model. To do so, different strategies have been proposed, some of them are reported in [34, 35, 59], however, in this thesis a novel approach is proposed as follows.

3.1.3.1 Modified Loewner Matrix technique

In this thesis, the poles of the model given by the system in (3.50)-(3.51) are extracted applying the built-in Matlab function *pole*(*sys*). Subsequently, the resulted unstable poles are removed or forced to be stable (setting its real part as negative). This process is equivalent to the extraction of $\mathbf{Y}^{\infty}$ in the traditional LM approach.

Then, using the obtained stable poles, the residues r_n, and asymptotic terms d and e are calculated as for the VF technique (Section 3.1.1.2). This novel implementation of the LM method allows a fair comparison with the VF and MPM techniques since the resulted model has the same structure. Furthermore, the model obtained is more efficient than the model given by the traditional LM method according to the following analysis.

To analyze the efficiency of the model obtained by the proposed modified LM technique, it is recalled that the size of the resulting $\mathbf{A}$ matrix using the traditional LM technique is $N \times N$, with

N being the number of dominant singular values. Since this matrix is full, it contains N^2 non-zero elements. On the other hand, in the proposed implementation, the size of the state matrix $\mathbf{A}$ is $Np \times Np$, similar to the model obtained via VF [22]. However, in the worst case (all poles being complex), the number of non-zero elements in matrix $\mathbf{A}$ is $2Np$ (see Appendix A). Since the number of inputs/outputs p is usually much lower than the order of the approximation N, the number of non-zero elements in $\mathbf{A}$ by the proposed approach ($2Np$) is usually much lower than N^2, given by the traditional LM method. A similar situation occurs with matrix $\mathbf{B}$, which is a sparse matrix (see appendix A) for the proposed approach, whereas it is a full matrix for the traditional LM method. Matrices $\mathbf{C}$ and $\mathbf{D}$ are full matrices in both cases.

Due to the sparsity feature of the model obtained by the proposed modified LM approach, the obtained model is computationally more efficient in transient simulations than the model obtained by the traditional LM method as sparsity techniques can be applied to the former.

3.2 Passivity assessment of rational models

In practical implementations of rational models, the passivity requirement (2.25) can be assessed by evaluating the eigenvalues of the Hermitian part of the fitted model, as stated in (2.26), for a set of discrete frequency points. However, the reliability of this method depends on the frequency range evaluated and the sampling rate used, i.e., passivity violations out of the frequency range evaluated, or between samples, can be ignored. For this reason, a more effective method such as the evaluation of the Hamiltonian matrix, introduced next, shall be used.

3.2.1 Hamiltonian matrix

According to the positive real matrix theorem given in section 2.1.6, passivity can be assessed only for the imaginary axis ($s = j\omega$) considering the Fourier transform. Under this condition, the conjugate transpose matrix required in (2.25) can be expressed as

$$\mathbf{Y}(s)^H = \mathbf{Y}(-s)^T, \tag{3.67}$$

such that passivity can be assessed by the condition

$$\mathbf{\Psi}(s) = \frac{1}{2}\left[\mathbf{Y}(s) + \mathbf{Y}(-s)^T\right] \geq 0, \quad \forall \omega > 0, \tag{3.68}$$

where $\boldsymbol{\Psi}(s)$ is known as the Popov function [56]. The nonnegative definiteness of $\boldsymbol{\Psi}(s)$ as indicated in (3.68) is equivalent to require the Popov function to have all its eigenvalues nonnegative, i.e.,

$$\text{eig}\left\{\boldsymbol{\Psi}(s)\right\} \geq 0\,, \quad \forall \omega > 0\,. \tag{3.69}$$

Since the eigenvalues of the Popov function $\boldsymbol{\Psi}(s)$ as defined in (3.68) are continuous functions of the frequency, an eigenvalue that is equal to zero at a certain frequency means that this eigenvalue is passing from positive to negative values, i.e., passivity violations. The frequencies at which the eigenvalues of $\boldsymbol{\Psi}(s)$ are zero can be found by computing the zeros of the Popov function, i.e., the values of $s = j\omega$ that make the function equal to zero. Mathematically, this is expressed as

$$\boldsymbol{\Psi}(s_0)\mathbf{u} = 0\,, \tag{3.70}$$

where $s_0 = j\omega_0$ and $\mathbf{u}$ is a non-zero vector.

From (3.70), $\mathbf{u}$ can be interpreted as the i^{th} right eigenvector of $\boldsymbol{\Psi}(s_0)$ associated to the i^{th} eigenvalue ($\lambda_i = 0$). From (3.68), it can be observed that the Popov function is constituted of the sum of the functions $\mathbf{Y}(s)$ and $\mathbf{Y}(-s)^T$. Taking into account (2.6), which denotes the transfer function for $\mathbf{Y}(s)$, the corresponding transfer function for $\mathbf{Y}(-s)^T$ is

$$\mathbf{Y}(-s)^T = -\mathbf{B}^T\left(s\mathbf{I} - \left[-\mathbf{A}^T\right]\right)^{-1}\mathbf{C}^T + \mathbf{D}^T - s\mathbf{E}^T\,, \tag{3.71}$$

for which the following state-space form can be given:

$$\dot{\bar{\mathbf{x}}}(t) = -\mathbf{A}^T\bar{\mathbf{x}}(t) + \mathbf{C}^T\mathbf{u}(t)\,, \tag{3.72}$$

$$\bar{\mathbf{y}}(t) = -\mathbf{B}^T\bar{\mathbf{x}}(t) + \mathbf{D}^T\mathbf{u}(t) - \mathbf{E}^T\dot{\mathbf{u}}(t)\,. \tag{3.73}$$

Thus, a state-space model representation of the Popov function can be obtained by assembling the state-space models of $\mathbf{Y}(s)$ and $\mathbf{Y}(-s)^T$, the resulting model is given by

$$\dot{\mathbf{x}}_\Psi(t) = \mathbf{A}_\Psi\mathbf{x}_\Psi(t) + \mathbf{B}_\Psi\mathbf{u}(t)\,, \tag{3.74}$$

$$\mathbf{y}_{\Psi}(t)=\mathbf{C}_{\Psi}\mathbf{x}_{\Psi}(t)+\mathbf{D}_{\Psi}\mathbf{u}(t)+\mathbf{E}_{\Psi}\mathbf{u}(t), \tag{3.75}$$

where:

$$\mathbf{x}_{\Psi}(t)=\begin{bmatrix}\mathbf{x}(t) & \bar{\mathbf{x}}(t)\end{bmatrix}^{T}, \tag{3.76}$$

$$\mathbf{y}_{\Psi}(t)=\frac{1}{2}\begin{bmatrix}\mathbf{y}(t)+\bar{\mathbf{y}}(t)\end{bmatrix}, \tag{3.77}$$

$$\mathbf{A}_{\Psi}=\begin{bmatrix}\mathbf{A} & \mathbf{0}\\ \mathbf{0} & -\mathbf{A}^{T}\end{bmatrix}, \tag{3.78}$$

$$\mathbf{B}_{\Psi}=\begin{bmatrix}\mathbf{B}\\ -\mathbf{C}^{T}\end{bmatrix}, \tag{3.79}$$

$$\mathbf{C}_{\Psi}=\frac{1}{2}\begin{bmatrix}\mathbf{C} & \mathbf{B}^{T}\end{bmatrix}, \tag{3.80}$$

$$\mathbf{D}_{\Psi}=\frac{1}{2}\begin{bmatrix}\mathbf{D}+\mathbf{D}^{T}\end{bmatrix}, \tag{3.81}$$

$$\mathbf{E}_{\Psi}=\frac{1}{2}\begin{bmatrix}\mathbf{E}-\mathbf{E}^{T}\end{bmatrix}. \tag{3.82}$$

Note that for a symmetrical system $\mathbf{E}_{\Psi}=\mathbf{0}$.

To compute the zeros of $\boldsymbol{\Psi}(s)$, the input and output of the state-space model given by (3.74)-(3.75) are inversed. The resulted system is

$$\dot{\mathbf{x}}_{\Psi}(t)=\left(\mathbf{A}_{\Psi}-\mathbf{B}_{\Psi}\mathbf{D}_{\Psi}^{-1}\mathbf{C}_{\Psi}\right)\mathbf{x}_{\Psi}(t)+\left(\mathbf{B}_{\Psi}\mathbf{D}_{\Psi}^{-1}\right)\mathbf{y}_{\Psi}(t), \tag{3.83}$$

$$\mathbf{u}(t)=\left(-\mathbf{D}_{\Psi}^{-1}\mathbf{C}_{\Psi}\right)\mathbf{x}_{\Psi}(t)+\mathbf{D}_{\Psi}^{-1}\mathbf{y}(t). \tag{3.84}$$

Then, the zeros of $\boldsymbol{\Psi}(s)$ can be obtained as the poles of the system described by (3.83)-(3.84), or equivalently, as the eigenvalues of the state matrix in (3.83), i.e.,

$$\mathbf{z}=\mathrm{eig}\left(\mathbf{A}_{\Psi}-\mathbf{B}_{\Psi}\mathbf{D}_{\Psi}^{-1}\mathbf{C}_{\Psi}\right). \tag{3.85}$$

Considering the assembled system as described in (3.76)-(3.82), the state matrix in (3.83) can be expressed as

$$\mathbf{H} = \mathbf{A}_{\Psi} - \mathbf{B}_{\Psi}\mathbf{D}_{\Psi}^{-1}\mathbf{C}_{\Psi} = \begin{bmatrix} \mathbf{A} & \mathbf{0} \\ \mathbf{0} & -\mathbf{A}^T \end{bmatrix} - \begin{bmatrix} \mathbf{B} \\ -\mathbf{C}^T \end{bmatrix} \left[\frac{1}{2}\left(\mathbf{D} + \mathbf{D}^T\right) \right]^{-1} \frac{1}{2} \begin{bmatrix} \mathbf{C} & \mathbf{B}^T \end{bmatrix}. \tag{3.86}$$

After solving for the matrix operations in (3.86), the following matrix is obtained

$$\mathbf{H} = \begin{bmatrix} \mathbf{A} - \mathbf{B}\left(\mathbf{D} + \mathbf{D}^T\right)^{-1}\mathbf{C} & -\mathbf{B}\left(\mathbf{D} + \mathbf{D}^T\right)^{-1}\mathbf{B}^T \\ \mathbf{C}^T\left(\mathbf{D} + \mathbf{D}^T\right)^{-1}\mathbf{C} & -\mathbf{A}^T + \mathbf{C}^T\left(\mathbf{D} + \mathbf{D}^T\right)^{-1}\mathbf{B}^T \end{bmatrix}. \tag{3.87}$$

The resulting matrix $\mathbf{H}$ is a Hamiltonian matrix, defined as follows.

A generic matrix $\boldsymbol{\Xi}$ is a Hamiltonian matrix if and only if

$$\mathbf{J}\boldsymbol{\Xi} = \left(\mathbf{J}\boldsymbol{\Xi}\right)^T, \tag{3.88}$$

where

$$\mathbf{J} = \begin{bmatrix} 0 & \mathbf{I} \\ -\mathbf{I} & 0 \end{bmatrix} \tag{3.89}$$

with $\mathbf{I}$ being the identity matrix.

Since the purely imaginary eigenvalues of the $\mathbf{H}$, denote the zeros of the Popov function according to (3.70), i.e., the frequencies at which the eigenvalues of $\boldsymbol{\Psi}(s)$ are zero (boundaries of passivity violations). Thus, in the case that none of the eigenvalues of $\mathbf{H}$ is purely imaginary, the evaluated system is passive.

An important characteristic of Hamiltonian matrices is the eigenvalues four-quadrant symmetry. To explain this characteristic, let us assume that λ is a complex-valued eigenvalue of $\boldsymbol{\Psi}(s)$, then, the eigenvalues $-\lambda$, λ^* and $-\lambda^*$ are also eigenvalues of $\boldsymbol{\Psi}(s)$. In the case of a purely imaginary eigenvalue λ, λ^* is also an eigenvalue of $\boldsymbol{\Psi}(s)$. This characteristic of Hamiltonian matrices suggests that the information obtained from its eigenvalues is redundant. Also, note that the size of $\mathbf{H}$ in (3.87) is $2N \times 2N$, being N the number of states of the state-space model (2.4)-(2.5).

3.2.2 Singularity test matrix

Instead of computing the eigenvalues of the Hamiltonian matrix $\mathbf{H}$, as defined in (3.87), an alternative (more efficient) method is the use of the so-called half-size singularity test matrix. As its name indicates, dimension of this matrix is half the size of $\mathbf{H}$, which allows a more efficient passivity evaluation. This alternative method is of especial interest for large-order models.

To derive the half-size singularity test matrix, the complex conjugate transpose matrix $\mathbf{Y}(s)^H$, as required in (2.25), is expressed as

$$\mathbf{Y}(s)^H = \mathbf{Y}(-s). \tag{3.90}$$

Note that (3.90) is valid considering $s = j\omega$.

Then, taking into account (3.90), a similar process as for the derivation of $\mathbf{H}$ is applied. In this case, the function $\mathbf{Y}(-s)$ is represented by the alternative state-space model

$$\dot{\overline{\mathbf{x}}}(t) = -\mathbf{A}\overline{\mathbf{x}}(t) - \mathbf{B}\mathbf{u}(t), \tag{3.91}$$

$$\overline{\mathbf{y}}(t) = \mathbf{C}\overline{\mathbf{x}}(t) + \mathbf{D}\mathbf{u}(t). \tag{3.92}$$

Then, an augmented state-space model is created using the subsystems denoted by (2.4)-(2.5) and (3.91)-(3.92). The following augmented matrices are obtained

$$\tilde{\mathbf{A}} = \begin{bmatrix} \mathbf{A} & \mathbf{0} \\ \mathbf{0} & -\mathbf{A} \end{bmatrix}, \tag{3.93}$$

$$\tilde{\mathbf{B}} = \begin{bmatrix} \mathbf{B} \\ -\mathbf{B} \end{bmatrix}, \tag{3.94}$$

$$\tilde{\mathbf{C}} = \frac{1}{2}\begin{bmatrix} \mathbf{C} & \mathbf{C} \end{bmatrix}, \tag{3.95}$$

$$\tilde{\mathbf{D}} = \mathbf{D}, \tag{3.96}$$

As for the derivation of the Hamiltonian matrix $\mathbf{H}$, the input and output of the resulting augmented state-space model are inversed, the result is analogous to (3.83)-(3.84). Finally, the state matrix of the resulting system with input and output inversed (analogous to (3.86) for $\mathbf{H}$) is

$$\mathbf{P} = \tilde{\mathbf{A}} - \tilde{\mathbf{B}}\tilde{\mathbf{D}}^{-1}\tilde{\mathbf{C}} = \begin{bmatrix} \mathbf{A} - \tfrac{1}{2}\mathbf{B}\mathbf{D}^{-1}\mathbf{C} & -\tfrac{1}{2}\mathbf{B}\mathbf{D}^{-1}\mathbf{C} \\ \tfrac{1}{2}\mathbf{B}\mathbf{D}^{-1}\mathbf{C} & -\mathbf{A} + \tfrac{1}{2}\mathbf{B}\mathbf{D}^{-1}\mathbf{C} \end{bmatrix}. \tag{3.97}$$

The resulting matrix $\mathbf{P}$ is not a Hamiltonian matrix; however, since it is derived from an equivalent state-space representation than for $\mathbf{H}$, matrix $\mathbf{P}$ contains the same eigenvalues than the Hamiltonian matrix $\mathbf{H}$.

The next step for the derivation of the singularity test matrix is the application of a similarity transformation to $\mathbf{P}$ as follows

$$\hat{\mathbf{P}} = \mathbf{T}\mathbf{P}\mathbf{T}^{-1} = \begin{bmatrix} \mathbf{0} & \mathbf{A} \\ \mathbf{A} - \mathbf{B}\mathbf{D}^{-1}\mathbf{C} & \mathbf{0} \end{bmatrix}. \tag{3.98}$$

where

$$\mathbf{T} = \frac{1}{\sqrt{2}} \begin{bmatrix} \mathbf{I} & \mathbf{I} \\ \mathbf{I} & -\mathbf{I} \end{bmatrix}, \tag{3.99}$$

being $\mathbf{I}$ the identity matrix. Note that this transformation does not modify the eigenvalues of $\mathbf{P}$.

Finally, by calculating the square of $\hat{\mathbf{P}}$, one obtains

$$\hat{\mathbf{P}}^2 = \begin{bmatrix} \mathbf{A}\left(\mathbf{A} - \mathbf{B}\mathbf{D}^{-1}\mathbf{C}\right) & \mathbf{0} \\ \mathbf{0} & \left(\mathbf{A} - \mathbf{B}\mathbf{D}^{-1}\mathbf{C}\right)\mathbf{A} \end{bmatrix} = \begin{bmatrix} \mathbf{S} & \mathbf{0} \\ \mathbf{0} & \mathbf{S}' \end{bmatrix}. \tag{3.100}$$

Due to its block-diagonal composition, matrix $\hat{\mathbf{P}}^2$ constitutes a spectral factorization of $\mathbf{P}$. In other words, the eigenvalues of $\mathbf{P}$ become split into the eigenvalues of the two non-zero matrix blocks in (3.100). This factorization permits the extraction of the essential information of $\mathbf{P}$ from any of the two submatrices, $\mathbf{S}$ or $\mathbf{S}'$ in (3.100).

Then, the half-size singularity test matrix is defined as

$$\mathbf{S} = \mathbf{A}\left(\mathbf{A} - \mathbf{B}\mathbf{D}^{-1}\mathbf{C}\right). \tag{3.101}$$

Note that the eigenvalues of $\mathbf{P}$ (or equivalently, the eigenvalues of $\mathbf{H}$) and those of $\hat{\mathbf{P}}^2$ (or $\mathbf{S}$) are related by the power of two as

$$\text{eig}\left(\mathbf{P}\right)^2 = \text{eig}\left(\hat{\mathbf{P}}^2\right). \tag{3.102}$$

Thus, the purely imaginary eigenvalues of $\mathbf{H}$ (which denote passivity violations) are equivalently found in $\mathbf{S}$ but to the power of two.

To complement this analysis, let us consider that the n^{th} eigenvalue of $\mathbf{H}$ is purely imaginary, i.e.

$$\lambda_n = j\omega_0, \quad : \lambda_n \in \text{eig}\left(\mathbf{H}\right), \tag{3.103}$$

then, the power of two of this eigenvalue is one of the eigenvalues of $\mathbf{S}$, i.e.,

$$\lambda_i = \lambda_n^2 = -\omega_0^2, \quad : \lambda_i \in \text{eig}\left(\mathbf{S}\right), \tag{3.104}$$

From (3.104), it can be observed that the eigenvalues of $\mathbf{S}$ that reveal passivity violations, are purely real and negative. Also, it is observed that the zero-crossing frequencies (boundaries of passivity violations) are given by the square root of these eigenvalues.

3.3 Passivity enforcement of rational models

Firstly, in this section some general facts about the passivity enforcement of rational models are analyzed. Then, a brief review of existent passivity enforcement techniques is presented.

In general, a non-passive rational model can be forced to be passive by perturbing any of its parameters, such as, poles, residues and/or asymptotic matrices. The model perturbation should, however, be as small as possible to avoid corrupting its frequency-response, which has been fitted to match the frequency-response of the device or subsystem being modeled.

Since the rational model is constituted as a sum of pole/residue pairs and asymptotic matrices $\mathbf{D}$ and $\mathbf{E}$, it is possible to split the problem in two parts, i.e., the enforcement of the rational part (poles and residues) and the enforcement of asymptotic matrices.

In the case of the rational part of the model, it is possible to perturb each pole-residue pair to be passive, so that the overall rational part of the model is guaranteed to be passive. This approach is, however, impractical since individual residue-pole pairs may violate passivity at frequencies where the overall rational part of the model is passive. Thus, the model could be perturbed more than necessary, and in turn, the frequency-response of the model may substantially be disturbed.

Also, it is important to realize that the perturbation of the poles and residues of the rational model (2.3), is equivalent to the perturbation of matrices $\mathbf{A}$ and $\mathbf{C}$ of the model in state-space form (2.4) -(2.5), respectively, according to the model equivalencing given in Appendix A. Moreover, note that perturbation of matrix $\mathbf{B}$ is meaningless since $\mathbf{B}$ is a matrix representing a unitary contribution of the input signal(s) over the states of the system (see Appendix A). A significant contribution of the input(s) to the output(s) of the system is given by matrix $\mathbf{C}$.

Therefore, by analyzing the two possible matrices for perturbing the rational part of the model ($\mathbf{A}$ and $\mathbf{C}$), it can be noticed that perturbing the poles of the system is equivalent to modify the system dynamics, or the natural frequencies of the model, which are very important properties. Also, since the computation of the poles is the most challenging step in the fitting process, a passivity enforcement method based on poles perturbation might be even more challenging. Due to these reasons, the perturbation of the residues of the model or equivalently, the perturbation of matrix $\mathbf{C}$ of the model is preferred.

By perturbing matrix $\mathbf{C}$, a matrix perturbation $\Delta\mathbf{C}$ should be calculated and applied, producing a perturbation of the frequency response as given by

$$\Delta\mathbf{Y}(s) = \Delta\mathbf{C}(s\mathbf{I} - \mathbf{A})^{-1}\mathbf{B}, \tag{3.105}$$

such that the perturbed model

$$\hat{\mathbf{Y}}(s) = \mathbf{Y}(s) + \Delta\mathbf{Y}(s) \tag{3.106}$$

becomes passive.

In the case of the asymptotic matrices $\mathbf{D}$ and $\mathbf{E}$, these matrices can be treated separately to enforce the passivity of the model for $s \to \infty$. Also, note that from the passivity condition given in (2.26), if $\mathbf{Y}(s)$ is a symmetric matrix (such as the cases studied in this thesis), the passivity of the model only relies on the real part of $\mathbf{Y}(s)$, for which matrix $\mathbf{E}$ does not have any contribution. However, the passivity enforcement of $\mathbf{E}$ is also necessary, otherwise, the capacitance matrix $\mathbf{E}$ may denote a non-passive subsystem.

Since the passivity enforcement of the asymptotic matrices $\mathbf{D}$ and/or $\mathbf{E}$ is straightforward, a simple but effective method to do so is first presented; subsequently, different methodologies for the passivity enforcement of the rational part of the model are presented.

3.3.1 Passivity enforcement of asymptotic matrices

As for the overall rational model, the condition to ensure the asymptotic passivity of the rational model is that $\mathbf{D}$ and $\mathbf{E}$ must be nonnegative definite. This condition is equivalent to require all its eigenvalues to be nonnegative. Then, let us suppose that the i^{th} eigenvalue of $\mathbf{D}$ (or $\mathbf{E}$) is negative, i.e.,

$$\lambda_i < 0, \quad : \lambda_i \in \text{eig}(\mathbf{D}), \tag{3.107}$$

and the eigenvalues of $\mathbf{D}$ can be calculated as

$$\mathbf{\Lambda} = \mathbf{T}\mathbf{D}\mathbf{T}^{-1}, \tag{3.108}$$

where $\mathbf{\Lambda}$ is a diagonal matrix containing the eigenvalues of the $\mathbf{D}$, and $\mathbf{T}$ is a full matrix containing the right eigenvectors.

The negative eigenvalues of matrix $\mathbf{D}$, can be simply replaced by 0, or by a predefined positive value, such that a new, nonnegative definite matrix $\mathbf{D}^+$ can be obtained as

$$\mathbf{D}^+ = \mathbf{T}^{-1}\mathbf{\Lambda}_{enforced}\mathbf{T}, \tag{3.109}$$

where $\mathbf{\Lambda}_{enforced}$ is a diagonal matrix containing the eigenvalues of the $\mathbf{D}$ matrix with only nonnegative entries (enforced).

Since this action may cause considerably deviation of the frequency-response of the rational model, the residues of the model must be recalculated using the modified function

$$\mathbf{Y}_{modified}(s) = \mathbf{Y}(s) - \mathbf{D}^+, \tag{3.110}$$

if only matrix $\mathbf{D}$ has been perturbed, or

$$\mathbf{Y}_{modified}(s) = \mathbf{Y}(s) - \mathbf{D}^+ - s\mathbf{E}^+, \tag{3.111}$$

if both $\mathbf{D}$ and $\mathbf{E}$ have been perturbed. Alternatively, only the contribution of $s\mathbf{E}^{+}$ can be subtracted if only $\mathbf{E}$ matrix has been perturbed. Note that the fitting of $\mathbf{Y}_{modified}(s)$ must be achieved without $\mathbf{D}$ and/or $\mathbf{E}$, depending on the case, as follows.

Only matrix $\mathbf{D}$ has been perturbed:

$$\mathbf{Y}_{modified}(s) \simeq \sum_{n=1}^{N} \frac{\mathbf{R}_n}{s-a_n} + s\mathbf{E}\,. \tag{3.112}$$

Both $\mathbf{D}$ and $\mathbf{E}$ have been perturbed:

$$\mathbf{Y}_{modified}(s) \simeq \sum_{n=1}^{N} \frac{\mathbf{R}_n}{s-a_n}\,. \tag{3.113}$$

Only matrix $\mathbf{E}$ has been perturbed:

$$\mathbf{Y}_{modified}(s) \simeq \sum_{n=1}^{N} \frac{\mathbf{R}_n}{s-a_n} + \mathbf{D}\,. \tag{3.114}$$

Then, the new rational function (3.112), (3.113) or (3.114) in addition to the enforced matrix $\mathbf{D}^{+}$ and/or $\mathbf{E}^{+}$, form a new (asymptotically passive) model.

Finally, a new passivity assessment must be performed for the asymptotically passive model, and, if passivity violations persist, the pole-residue elements of the system must be enforced by one of the methodologies presented next.

3.3.2 Fast residue perturbation technique

The original idea about perturbing the residues of the rational model for passivity enforcement is given in [60]. Since this approach considers the symmetry of the model, perturbations are calculated only for the upper triangular elements of the residue matrices. Thus, the number of variables to be perturbed is

$$N_{unknownsRP} = N(p+1)\,p/2\,, \tag{3.115}$$

where N and p denote the order and the number of input/outputs of the rational model, respectively.

Later, this approach was improved by proposing only the perturbation of the eigenvalues of the residue matrices, instead of all the upper triangular elements. This second approach is named Fast Residue Perturbation (FRP) [42]. The advantage of the FRP method over the original residue perturbation technique is the reduction of the number of perturbed variables to

$$N_{unknownsFRP} = Np\,. \tag{3.116}$$

To start with the study of the FRP method, first, let us considered that every residue matrix ($\mathbf{R}_i$) can be diagonalized as follows

$$\mathbf{R}_i = \mathbf{VMW} = \begin{bmatrix} \mathbf{v}_1 & \cdots & \mathbf{v}_p \end{bmatrix} \begin{bmatrix} \mu_1 & & \\ & \ddots & \\ & & \mu_p \end{bmatrix} \begin{bmatrix} \mathbf{w}_1 \\ \vdots \\ \mathbf{w}_p \end{bmatrix}. \tag{3.117}$$

where $\mathbf{v}_n$, $\mathbf{w}_n$ and μ_n are the n^{th} right-eigenvector, left-eigenvector and eigenvalue, respectively. Note that equivalent to (3.117), each residue matrix can be factorized as follows:

$$\mathbf{R}_i = \mathbf{v}_1\mathbf{w}_1\mu_1 + \cdots + \mathbf{v}_p\mathbf{w}_p\mu_p = \begin{bmatrix} \gamma_{11,1} & \cdots & \gamma_{1p,1} \\ \vdots & \ddots & \vdots \\ \gamma_{p1,1} & \cdots & \mu_{pp,1} \end{bmatrix} \mu_1 + \cdots + \begin{bmatrix} \gamma_{11,p} & \cdots & \gamma_{1p,p} \\ \vdots & \ddots & \vdots \\ \gamma_{p1,p} & \cdots & \mu_{pp,p} \end{bmatrix} \mu_p\,. \tag{3.118}$$

or in compact form,

$$\mathbf{R}_i = \sum_{k=1}^{p} \mathbf{\Gamma}_{ki}\mu_{ki}\,, \tag{3.119}$$

where each matrix $\mathbf{\Gamma}_{ki}$ consists of the product of the k^{th} right- and left-eigenvector, for the i^{th} residue matrix, i.e.,

$$\mathbf{\Gamma}_{ki} = \mathbf{v}_k\mathbf{w}_k = \begin{bmatrix} \gamma_{11,i} & \cdots & \gamma_{1p,i} \\ \vdots & \ddots & \vdots \\ \gamma_{p1,i} & \cdots & \mu_{pp,i} \end{bmatrix}. \tag{3.120}$$

In the case of complex conjugate residue matrices, the real and imaginary parts are considered as two independent matrices.

Substituting (3.119) into the original rational model (2.3), the rational model can be expressed as

$$\mathbf{Y}_{fitted}(s)=\sum_{n=1}^{N}\sum_{k=1}^{p}\frac{\mathbf{\Gamma}_{kn}\mu_{kn}}{s-a_n}+\mathbf{D}+s\mathbf{E}\,. \tag{3.121}$$

Considering (3.121), the upper triangular elements of $\mathbf{Y}_{fitted}(s)$ stacked in a column vector as given in (3.31), can be expressed as a function of the eigenvalues of the residue matrices, i.e.,

$$\begin{bmatrix} \frac{\gamma_{11,1,1}}{s-a_1} & \cdots & \frac{\gamma_{11,p,1}}{s-a_1} & \cdots & \frac{\gamma_{11,1,N}}{s-a_N} & \cdots & \frac{\gamma_{11,p,N}}{s-a_N} \\ \vdots & & \vdots & & \vdots & & \vdots \\ \frac{\gamma_{1p,1,1}}{s-a_1} & \cdots & \frac{\gamma_{1p,p,1}}{s-a_1} & \cdots & \frac{\gamma_{1p,1,N}}{s-a_N} & \cdots & \frac{\gamma_{1p,p,N}}{s-a_N} \\ \vdots & & \vdots & & \vdots & & \vdots \\ \frac{\gamma_{p1,1,1}}{s-a_1} & \cdots & \frac{\gamma_{p1,p,1}}{s-a_1} & \cdots & \frac{\gamma_{p1,1,N}}{s-a_N} & \cdots & \frac{\gamma_{p1,p,N}}{s-a_N} \\ \vdots & & \vdots & & \vdots & & \vdots \\ \frac{\gamma_{pp,1,1}}{s-a_1} & \cdots & \frac{\gamma_{pp,p,1}}{s-a_1} & \cdots & \frac{\gamma_{pp,1,N}}{s-a_N} & \cdots & \frac{\gamma_{pp,p,N}}{s-a_N} \end{bmatrix} \begin{bmatrix} \mu_{1,1} \\ \vdots \\ \mu_{p,1} \\ \vdots \\ \mu_{1,N} \\ \vdots \\ \mu_{p,N} \end{bmatrix} + \begin{bmatrix} d_{11} \\ \vdots \\ d_{1p} \\ \vdots \\ d_{p1} \\ \vdots \\ d_{pp} \end{bmatrix} + s\begin{bmatrix} e_{11} \\ \vdots \\ e_{1p} \\ \vdots \\ e_{p1} \\ \vdots \\ e_{pp} \end{bmatrix} = \begin{bmatrix} y_{11}(s) \\ \vdots \\ y_{1p}(s) \\ \vdots \\ y_{p1}(s) \\ \vdots \\ y_{pp}(s) \end{bmatrix}, \tag{3.122}$$

or in compact form

$$\mathbf{A}(s)\mathbf{x}+\mathbf{d}+s\mathbf{e}=\mathbf{y}(s)\,. \tag{3.123}$$

where , $\mathbf{x}\in\mathbb{C}^{Np\times 1}$ and $\mathbf{d},\mathbf{e},\mathbf{y}\in\mathbb{C}^{p(p+1)/2\times 1}$.

3.3.2.1 Objective function

Writing (3.122) for every frequency sample of the fitting band and stacking the resulting matrices, an augmented system of equations is obtained as follows

$$\begin{bmatrix} \mathbf{A}(s_1) \\ \vdots \\ \mathbf{A}(s_{N_s}) \end{bmatrix}\mathbf{x}+\begin{bmatrix} \mathbf{d} \\ \vdots \\ \mathbf{d} \end{bmatrix}+\begin{bmatrix} s_1\mathbf{e} \\ \vdots \\ s_{N_s}\mathbf{e} \end{bmatrix}=\begin{bmatrix} \mathbf{y}(s_1) \\ \vdots \\ \mathbf{y}(s_{N_s}) \end{bmatrix}, \tag{3.124}$$

or in compact form

$$\bar{\mathbf{A}}\mathbf{x}+\bar{\mathbf{d}}+\bar{\mathbf{e}}=\bar{\mathbf{y}}\,. \tag{3.125}$$

Since the objective is to perturb the eigenvalues of the residue matrices (contained in $\mathbf{x}$), equation (3.125) is linearized considering an increment of $\mathbf{x}$, i.e.,

$$\bar{\mathbf{A}}\Delta\mathbf{x} = \Delta\bar{\mathbf{y}}\,. \tag{3.126}$$

It should be noted that the increment induced to the fitted model $\Delta\bar{\mathbf{y}}$ by the perturbation $\Delta\mathbf{x}$, should be as minimal as possible to avoid corrupting the fitting accuracy of the rational model, i.e., it is required that $\Delta\bar{\mathbf{y}} \to 0$. In other words, the perturbation $\Delta\mathbf{x}$ is searched, such that the model perturbation $\Delta\bar{\mathbf{y}}$ is minimized. Thus, the following objective function is obtained

$$\min\ f\left(\Delta\mathbf{x}\right) = \bar{\mathbf{A}}\Delta\mathbf{x} = \Delta\mathbf{y}\,. \tag{3.127}$$

3.3.2.2 Constraints

The solution of (3.127) must, at the same time, produce an increment in the eigenvalues of the Hermitian part of the model to fulfill to the passivity condition given in (2.25). This requirement is used to write the constraints for the FRP method.

Since only symmetrical systems are studied in this thesis, the Hermitian part of the model is equal to the conductance matrix $\mathbf{G}\left(s\right)$, which is used henceforth for simplicity. Now, let us consider that the frequency s_k has been identified as the frequency at which the worst passivity violation occurs within a violation interval, and the eigenvalue $\lambda_i \in \mathrm{eig}\left[\mathbf{G}\left(s_k\right)\right]$ has the most negative value. For this eigenvalue, the following equation can be written

$$\mathbf{G}\left(s_k\right)\mathbf{v}_i = \lambda_i\mathbf{v}_i\,, \tag{3.128}$$

where $\mathbf{v}_i$ is the corresponding right eigenvector.

Multiplying (3.128) by the corresponding left eigenvector ($\mathbf{w}_i$) to the left side results into

$$\mathbf{w}_i\mathbf{G}\mathbf{v}_i = \mathbf{w}_i\lambda_i\mathbf{v}_i\,. \tag{3.129}$$

Note that in (3.129) the frequency dependence is omitted for brevity. Considering that the left- and right-eigenvalues have unitary norm and are not orthogonal, (3.129) can be simplified as

$$\lambda_i = \mathbf{w}_i \mathbf{G} \mathbf{v}_i = \begin{bmatrix} w_{i1} & \cdots & w_{ip} \end{bmatrix} \begin{bmatrix} g_{11} & \cdots & g_{1p} \\ \vdots & \ddots & \vdots \\ g_{p1} & \cdots & g_{pp} \end{bmatrix} \begin{bmatrix} v_{1i} \\ \vdots \\ v_{pi} \end{bmatrix}. \tag{3.130}$$

Expanding the matrix-vector products in (3.130) results into

$$\lambda_i = w_{i1} v_{1i} g_{11} + \cdots + w_{i1} v_{pi} g_{1p} + \cdots + w_{ip} v_{1i} g_{p1} + \cdots + w_{ip} v_{pi} g_{pp}. \tag{3.131}$$

Applying the same procedure for every eigenvalue of $\mathbf{G}(s_k)$ and assembling the equations, the following system of equations is obtained

$$\begin{bmatrix} \lambda_1 \\ \vdots \\ \lambda_p \end{bmatrix} = \begin{bmatrix} w_{11} v_{11} & \cdots & w_{11} v_{p1} & \cdots & w_{1p} v_{11} & \cdots & w_{1p} v_{p1} \\ \vdots & & \vdots & & \vdots & & \vdots \\ w_{p1} v_{1p} & \cdots & w_{p1} v_{pp} & \cdots & w_{pp} v_{1p} & \cdots & w_{pp} v_{pp} \end{bmatrix} \begin{bmatrix} g_{11} \\ \vdots \\ g_{1p} \\ \vdots \\ g_{p1} \\ \vdots \\ g_{pp} \end{bmatrix}, \tag{3.132}$$

or in compact form

$$\boldsymbol{\lambda}(s_k) = \mathbf{K}(s_k)\mathbf{g}(s_k), \tag{3.133}$$

Now, considering (3.123) the following relationship results:

$$\mathbf{g}(s_k) = \Re\{\mathbf{y}(s_k)\} = \Re\{\mathbf{A}(s_k)\}\mathbf{x} + \mathbf{d}. \tag{3.134}$$

Then, by substituting (3.134) into (3.133), the following expression is obtained

$$\boldsymbol{\lambda}(s_k) = \mathbf{Q}(s_k)\mathbf{x} + \mathbf{d}, \tag{3.135}$$

where

$$\mathbf{Q}(s_k) = \mathbf{K}(s_k)\Re\{\mathbf{A}(s_k)\}. \tag{3.136}$$

It is important to emphasize that not necessarily all the eigenvalues of $\mathbf{G}(s_k)$ are negative, and this is usually the case. Then, extracting the rows in (3.135) corresponding to the negative eigenvalues of $\mathbf{G}(s_k)$, the following subsystem of equations is obtained:

$$\boldsymbol{\lambda}_{neg}\left(s_k\right)=\mathbf{Q}_{neg}\left(s_k\right)\mathbf{x}+\mathbf{d}_{neg}\,, \tag{3.137}$$

such that $\boldsymbol{\lambda}_{neg}\left(s_k\right)$, contains only the negative eigenvalues of $\mathbf{G}\left(s_k\right)$.

Repeating the process for every violation interval, with worst passivity violation at the set of frequencies $\left\{s_{k1} \quad \cdots \quad s_{kn}\right\}$, an augmented system of equations

$$\begin{bmatrix}\boldsymbol{\lambda}_{neg}\left(s_{k1}\right)\\ \vdots \\ \boldsymbol{\lambda}_{neg}\left(s_{kn}\right)\end{bmatrix}=\begin{bmatrix}\mathbf{Q}_{neg}\left(s_{k1}\right)\\ \vdots \\ \mathbf{Q}_{neg}\left(s_{kn}\right)\end{bmatrix}\mathbf{x}+\begin{bmatrix}\mathbf{d}_{neg,k1}\\ \vdots \\ \mathbf{d}_{neg,kn}\end{bmatrix}, \tag{3.138}$$

is obtained. In a simpler form (3.138) can be expressed as

$$\bar{\boldsymbol{\lambda}}_{neg}=\bar{\mathbf{Q}}_{neg}\mathbf{x}+\bar{\mathbf{d}}_{neg}\,. \tag{3.139}$$

Then, applying linearization to (3.139) one obtains

$$\Delta\bar{\boldsymbol{\lambda}}_{neg}=\bar{\mathbf{Q}}_{neg}\Delta\mathbf{x}\,. \tag{3.140}$$

Since the objective of the perturbation in (3.140) is to make the negative eigenvalues positive, the following inequality can be set

$$\bar{\boldsymbol{\lambda}}_{neg}+\Delta\bar{\boldsymbol{\lambda}}_{neg}=\bar{\boldsymbol{\lambda}}_{neg}+\bar{\mathbf{Q}}_{neg}\Delta\mathbf{x}\geq 0\,, \tag{3.141}$$

which is the condition for the perturbed system to become passive at the selected frequencies (frequencies with worst passivity violations). Equation (3.141) constitutes the inequality constraint to be used next for the FRP solution.

3.3.2.3 Quadratic programming solution

The FRP technique [42] consists of solving the objective function (3.127) subject to the passivity constraint (3.141) via Quadratic Programming (QP). To do so, the objective function in (3.127) and inequality constraint in (3.141) must be modified as follows.

Multiplying (3.127) by its own transposed function to the left side, the objective function for the FRP technique becomes

$$\min\, f\left(\Delta\mathbf{x}\right)=\Delta\mathbf{x}^T\bar{\mathbf{A}}^T\bar{\mathbf{A}}\Delta\mathbf{x}\,. \tag{3.142}$$

On the other hand, (3.141) can be rewritten as

$$-\bar{\mathbf{Q}}_{neg}\Delta\mathbf{x} \le \bar{\boldsymbol{\lambda}}_{neg} - \varepsilon\,, \tag{3.143}$$

where ε is a tolerance value (assumed as very small, 10^{-5} for example), used to avoid that the perturbed eigenvalues become equal to zero but take a small positive value.

Finally, (3.142) and (3.143) can be solved as the generic QP minimization problem

$$\min\, f\left(\mathbf{x}\right) = \mathbf{x}^T\boldsymbol{\Phi}\mathbf{x} + \Upsilon^T\mathbf{x} \tag{3.144}$$

$$\text{s.t.}\quad \boldsymbol{\Psi}\mathbf{x} \le \mathbf{c} \tag{3.145}$$

where

$$\mathbf{x} = \Delta\mathbf{x}\,, \tag{3.146}$$

$$\boldsymbol{\Phi} = \bar{\mathbf{A}}^T\bar{\mathbf{A}}\,, \tag{3.147}$$

$$\Upsilon^T = \mathbf{0}\,. \tag{3.148}$$

$$\boldsymbol{\Psi} = -\bar{\mathbf{Q}}_{neg}\,, \tag{3.149}$$

$$\mathbf{c} = \bar{\boldsymbol{\lambda}}_{neg} - \varepsilon\,. \tag{3.150}$$

The solution of (3.144)-(3.145), given by (3.146) (increment of the eigenvalues of the residue matrices) is finally used to calculate the corresponding residue matrix perturbation via (3.117) in linearized form, i.e.,

$$\Delta\mathbf{R}_i = \mathbf{V}_i\Delta\mathbf{M}_i\mathbf{W}_i\,. \tag{3.151}$$

Since the resulting $\Delta\mathbf{R}_i$ matrices are non-symmetric, the perturbation can be set as the Hermitian part (symmetric part) of (3.151), to maintain the symmetry of the model, i.e.,

$$\Delta\mathbf{R}_{i,sym} = \frac{1}{2}\left(\Delta\mathbf{R}_i + \Delta\mathbf{R}_i^T\right). \tag{3.152}$$

It should be recalled that the outlined perturbation scheme by the FRP method forces the eigenvalues of the conductance matrix to be positive only at the worst passivity violation frequencies. Thus, this perturbation does not guarantee the overall system passivity. For that reason, perturbations must be applied iteratively until the overall system passivity is enforced.

3.3.3 Hamiltonian matrix perturbation technique

The Hamiltonian matrix perturbation (HMP) technique for the passivity enforcement of rational models studied in this thesis is based on [40]. The HMP technique consists of the perturbation the Hamiltonian matrix $\mathbf{H}$, defined in (3.87), which is associated to the equivalent state-space model representation of the fitted rational model.

As discussed in section 3.3, perturbations to the rational model are preferably applied over its residues, or equivalently, to the $\mathbf{C}$ matrix of the state-space model. Under this premise, the corresponding Hamiltonian matrix perturbation is given by

$$\Delta\mathbf{H} = \begin{bmatrix} -\mathbf{B}\left(\mathbf{D}+\mathbf{D}^T\right)^{-1}\Delta\mathbf{C} & \mathbf{0} \\ \mathbf{C}^T\left(\mathbf{D}+\mathbf{D}^T\right)^{-1}\Delta\mathbf{C} + \Delta\mathbf{C}^T\left(\mathbf{D}+\mathbf{D}^T\right)^{-1}\mathbf{C} & \Delta\mathbf{C}^T\left(\mathbf{D}+\mathbf{D}^T\right)^{-1}\mathbf{B}^T \end{bmatrix}. \tag{3.153}$$

The perturbation matrix $\Delta\mathbf{H}$ as given in (3.153) is calculated such that each pair of eigenvalues of the Hamiltonian matrix

$$\left\{\lambda_n = j\omega_i, \lambda_{n+1} = j\omega_{i+1}\right\} \in \mathrm{eig}\left(\mathbf{H}\right), \tag{3.154}$$

that denote a pair of zero-crossing frequencies for an eigenvalue $\lambda_k \in \mathrm{eig}\left[\mathbf{G}(s)\right]$, are displaced along the frequency axis to reduce the frequency interval of passivity violations, as illustrated in Figure 3.1.

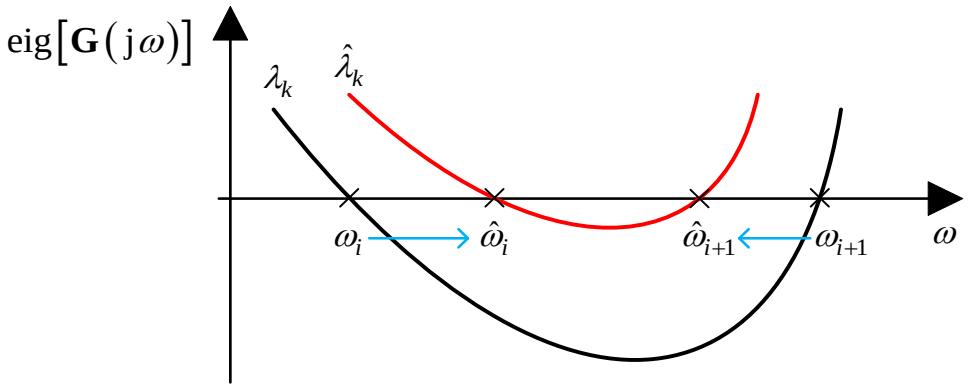

Figure 3.1. Hamiltonian matrix perturbation scheme.

In Figure 3.1, the eigenvalues of the perturbed Hamiltonian matrix $\hat{\mathbf{H}}$ are denoted as

$$\left\{\hat{\lambda}_n = j\hat{\omega}_i, \hat{\lambda}_{n+1} = j\hat{\omega}_{i+1}\right\} \in \mathrm{eig}\left(\hat{\mathbf{H}}\right). \tag{3.155}$$

where

$$\hat{\mathbf{H}} = \mathbf{H} + \Delta\mathbf{H}. \tag{3.156}$$

$$\hat{\lambda}_n = \lambda_n + \Delta\lambda_n. \tag{3.157}$$

To obtain the required $\Delta\mathbf{H}$, let us consider a single eigenvalue $\left\{\lambda_n = j\omega_i\right\} \in \mathrm{eig}\left(\mathbf{H}\right)$. For this eigenvalue the following relationships stand

$$\mathbf{H}\mathbf{v}_n = \lambda_n \mathbf{v}_n, \tag{3.158}$$

$$\mathbf{w}_n^H \mathbf{H} = \mathbf{w}_n^H \lambda_n, \tag{3.159}$$

where $\mathbf{v}_n$ and $\mathbf{w}_n$ are the associated right and left eigenvectors, respectively.

Then, considering a first order perturbation, the increment of the studied eigenvalue is given by

$$\Delta\lambda_n = \frac{\mathbf{w}_n^H \Delta\mathbf{H}\mathbf{v}_n}{\mathbf{w}_n^H \mathbf{v}_n}, \tag{3.160}$$

whenever $\mathbf{v}_n$ and $\mathbf{w}_n$ are not orthogonal. Also, without loss of generality, it can be considered that these vectors have been normalized, such that

$$\left\|\mathbf{v}_n\right\| = \left\|\mathbf{w}_n\right\| = 1. \tag{3.161}$$

For imaginary eigenvalues of $\mathbf{H}$ (the eigenvalues of interest), the corresponding eigenvectors are related as follows

$$\mathbf{w}_n = -\mathbf{J}\mathbf{v}_n, \tag{3.162}$$

where

$$\mathbf{J} = -\mathbf{J}^T = -\mathbf{J}^{-1} = \begin{bmatrix} \mathbf{0} & \mathbf{I} \\ -\mathbf{I} & \mathbf{0} \end{bmatrix}. \tag{3.163}$$

By substituting (3.162) into (3.160), the following expression is obtained

$$\Delta\lambda_n = \frac{\mathbf{v}_n^H \mathbf{J}\Delta\mathbf{H}\mathbf{v}_n}{\mathbf{v}_n^H \mathbf{J}\mathbf{v}_n}. \tag{3.164}$$

Then, partitioning the right eigenvector as

$$\mathbf{v}_n = \begin{bmatrix}\mathbf{v}_{n1} & \mathbf{v}_{n2}\end{bmatrix}^T, \tag{3.165}$$

the denominator in (3.164) becomes

$$\mathbf{v}_n^H \mathbf{J}\mathbf{v}_n = \begin{bmatrix}\mathbf{v}_{n1}^H & \mathbf{v}_{n2}^H\end{bmatrix}\begin{bmatrix}\mathbf{0} & \mathbf{I} \\ -\mathbf{I} & \mathbf{0}\end{bmatrix}\begin{bmatrix}\mathbf{v}_{n1} \\ \mathbf{v}_{n2}\end{bmatrix} = j2\Im\left\{\mathbf{v}_{n1}^H \mathbf{v}_{n2}\right\}. \tag{3.166}$$

On the other hand, the numerator becomes

$$\mathbf{v}_n^H \mathbf{J}\Delta\mathbf{H}\mathbf{v}_n = \begin{bmatrix}\mathbf{v}_{n1}^H & \mathbf{v}_{n2}^H\end{bmatrix}\begin{bmatrix}\mathbf{0} & \mathbf{I} \\ -\mathbf{I} & \mathbf{0}\end{bmatrix}\begin{bmatrix}\Delta\mathbf{H}_{11} & \mathbf{0} \\ \Delta\mathbf{H}_{21} & \Delta\mathbf{H}_{22}\end{bmatrix}\begin{bmatrix}\mathbf{v}_{n1} \\ \mathbf{v}_{n2}\end{bmatrix}, \tag{3.167}$$

which, after some algebraic operations, can be reduced to

$$\mathbf{v}_n^H \mathbf{J}\Delta\mathbf{H}\mathbf{v}_n = 2\Re\left\{\mathbf{y}_n^H \Delta\mathbf{C}\mathbf{v}_n\right\}, \tag{3.168}$$

where

$$\mathbf{y}_n = \left(\mathbf{D} + \mathbf{D}^T\right)^{-1}\mathbf{C}\mathbf{v}_{n1} + \left(\mathbf{D} + \mathbf{D}^T\right)^{-1}\mathbf{B}^T\mathbf{v}_{n2}. \tag{3.169}$$

Assembling the obtained expressions (3.166) and (3.168) into (3.164), the following expression is obtained

$$\Delta\lambda_n = j\left(\hat{\omega}_i - \omega_i\right) = \frac{2\Re\left\{\mathbf{y}_n^H \Delta\mathbf{C}\mathbf{v}_n\right\}}{j2\Im\left\{\mathbf{v}_{n1}^H \mathbf{v}_{n2}\right\}}, \tag{3.170}$$

which can be simplified to

$$\left(\omega_i - \hat{\omega}_i\right)\Im\left\{\mathbf{v}_{n1}^H \mathbf{v}_{n2}\right\} = \Re\left\{\mathbf{y}_n^H \Delta\mathbf{C}\mathbf{v}_{n1}\right\}. \tag{3.171}$$

Since the objective is to find $\Delta\mathbf{C}$, the following factorization can be used to detach $\Delta\mathbf{C}$:

$$\Re\left\{\mathbf{y}_n^H \Delta\mathbf{C}\mathbf{v}_{n1}\right\} = \Re\left\{\mathbf{v}_{n1}^T \otimes \mathbf{y}_n^H\right\}\mathrm{vec}\left(\Delta\mathbf{C}\right), \tag{3.172}$$

where the operator $\otimes$ denotes the Kronecker product, and $\mathrm{vec}(\ )$ indicates vectorization (the columns of the matrix argument are stacked). Finally, (3.171) can be rewritten as

$$\Re\left\{\mathbf{v}_{n1}^{T}\otimes\mathbf{y}_{n}^{H}\right\}\mathrm{vec}\left(\Delta\mathbf{C}\right)=\left(\omega_i-\hat{\omega}_i\right)\Im\left\{\mathbf{v}_{n1}^{H}\mathbf{v}_{n2}\right\}. \tag{3.173}$$

By arbitrarily defining the new position of the eigenvalue $\lambda_n = j\omega_i$, given by $\hat{\omega}_i$ in (3.173), this equation is already in a suitable form to formulate the following optimization problem

$$\min\left\|\mathbf{x}\right\|,\ \text{subject to}\ \ \mathbf{A}\mathbf{x}=\mathbf{b} \tag{3.174}$$

where

$$\mathbf{A}=\Re\left\{\mathbf{v}_{n1}^{T}\otimes\mathbf{y}_{n}^{H}\right\}, \tag{3.175}$$

$$\mathbf{x}=\mathrm{vec}\left(\Delta\mathbf{C}\right), \tag{3.176}$$

$$\mathbf{b}=\left(\omega_i-\hat{\omega}_i\right)\Im\left\{\mathbf{v}_{n1}^{H}\mathbf{v}_{n2}\right\}. \tag{3.177}$$

In the HMP method, (3.173) is written for all eigenvalues of $\mathbf{H}$ that denote a zero-crossing of some eigenvalue of $\mathbf{G}(s)$. Thus, the optimization problem given in (3.174) can be augmented accordingly by adding the set of equations given by each eigenvalue to be displaced. Since the system of equations in (3.174) is underdetermined (it contains more unknowns than equations), the problem has a closed-form solution, given by

$$\mathbf{x}_{*}=\mathbf{A}^{T}\left(\mathbf{A}\mathbf{A}^{T}\right)^{-1}\mathbf{b}. \tag{3.178}$$

Note that the optimization problem in (3.174) is formulated to obtain the minimum norm of $\mathrm{vec}\left(\Delta\mathbf{C}\right)$, since the objective is to calculate the perturbation as minimal as possible, such that the deviation of the frequency-response of the fitted model is also minimal. An alternative formulation can be obtained by minimizing the energy of $\Delta\mathbf{H}$ as proposed in [40].

To identify the necessary directions for the displacement of the eigenvalues of $\mathbf{H}$, such that passivity violation intervals become reduced, the derivative of the eigenvalues can be used as follows. Let us use the example presented in Figure 3.1. In this figure, it can be observed that eigenvalue $\lambda_n = j\omega_i \in \mathrm{eig}\left(\mathbf{H}\right)$ must be displaced to the right of the $j\omega$ axis (towards higher

frequencies), and the derivative of the eigenvalue $\lambda_k \in \text{eig}\left[\mathbf{G}(s)\right]$ evaluated at frequency ω_i is negative. On the other hand, eigenvalue $\lambda_{n+1} = j\omega_{i+1} \in \text{eig}(\mathbf{H})$ must be displaced to the left side of the $j\omega$ axis, and the derivative of $\lambda_k \in \text{eig}\left[\mathbf{G}(s)\right]$ evaluated at frequency ω_i is positive. These directions are indicated by blue arrows in Figure 3.1.

For the new positions of the eigenvalues of the Hamiltonian matrix, different approaches can be used, for example, for the passivity violation illustrated in Figure 3.1, the violation interval can be divided in three parts, then, the new positions can be set as the old positions plus/minus one third of the violation interval according to the required direction. Alternative approaches for the derivation of the new positions for the eigenvalues of $\mathbf{H}$ are given in chapter 10 of [56].

As final remark, it should be considered that the outlined perturbation by the HMP method is based on a first order perturbation according to (3.160). This approximation is considered accurate for small perturbations. Also, note that the perturbation of matrix $\mathbf{C}$ as resulted from (3.174), must be applied iteratively until passivity violations are fully removed.

3.3.4 Semidefinite programming-based convex optimization technique

The semidefinite programming (SDP) passivity enforcement technique analyzed in this thesis is based on the approach presented in [43]. In this formulation, matrices $\mathbf{A}$ and $\mathbf{B}$ of the initially obtained (non-passive) state-space model are kept, whereas matrices $\mathbf{C}$, $\mathbf{D}$ and $\mathbf{E}$ are totally recalculated such that the positive real lemma (analyzed in section 2.1.7) is satisfied. The resulting optimization problem is solved using an SDP approach.

3.3.4.1 Convex optimization problem

The objective function by the SDP method is to minimize the weighted error between the frequency-response of the original model and that of the fitted state-space model. For the (i, j) entry of the fitted admittance matrix function, the weighted error is given by

$$\varepsilon_{i,j} = \sum_{k=1}^{N_S} w_{i,j,k} \left\| \mathbf{Y}_{fitted\ i,j}(s_k) - \mathbf{Y}_{i,j}(s_k) \right\|_2^2, \tag{3.179}$$

where $w_{i,j,k}$ denotes the weight for the (i, j) matrix entry and the k^{th} frequency sample. Equation (3.179) can be alternatively expressed as

$$\varepsilon_{i,j} = \left\| \mathbf{F}_{i,j}\mathbf{X}_i - \mathbf{G}_{i,j} \right\|, \tag{3.180}$$

where each row of $\mathbf{F}_{i,j}$ (row vector $\mathbf{f}_k$) is given by

$$\mathbf{f}_k = \begin{cases} w_{i,j,k}\,\mathrm{Re}\left\{ \mathbf{B}_j^T \left(s_k\mathbf{I} - \mathbf{A}^T \right)^{-1} \mathbf{I}_j^T s_k \mathbf{I}_j^T \right\} & k \le N_s \\ w_{i,j,(k-N_s)}\,\mathrm{Im}\left\{ \mathbf{B}_j^T \left(s_{(k-N_s)}\mathbf{I} - \mathbf{A}^T \right)^{-1} \mathbf{I}_j^T s_{(k-N_s)} \mathbf{I}_j^T \right\} & k > N_s \end{cases} \tag{3.181}$$

where $\mathbf{I}_j$ denotes the j^{th} column of the identity matrix; and $\mathbf{G}_{i,j}$ in (3.180) is given by

$$\mathbf{G}_{i,j} = \begin{cases} w_{i,j,k}\,\mathrm{Re}\left\{ \mathbf{Y}_{i,j}\left(s_k\right) \right\} & k \le N_s \\ w_{i,j,(k-N_s)}\,\mathrm{Im}\left\{ \mathbf{Y}_{i,j}\left(s_k\right) \right\} & k > N_s \end{cases}, \tag{3.182}$$

and the unknowns' vector $\mathbf{X}_i$ in (3.180) is denoted by

$$\mathbf{X}_i = \begin{bmatrix} \mathbf{C}_i^T \\ \mathbf{D}_i^T \\ \mathbf{E}_i^T \end{bmatrix}. \tag{3.183}$$

where the *i* subscript denotes the i^{th} column of the corresponding matrix.

From (3.180), an alternative expression can be obtained as

$$\left| \mathbf{F}_{i,j}\mathbf{X}_i - \mathbf{G}_{i,j} \right| = \left(\mathbf{F}_{i,j}\mathbf{X}_i - \mathbf{G}_{i,j} \right)^T \left(\mathbf{F}_{i,j}\mathbf{X}_i - \mathbf{G}_{i,j} \right), \tag{3.184}$$

and, by applying QR factorization

$$\mathbf{F}_{i,j} = \mathbf{Q}_{i,j}\mathbf{R}_{i,j}, \tag{3.185}$$

where $\mathbf{Q}_{i,j}$ is a unitary matrix, i.e.,

$$\mathbf{Q}_{i,j}\mathbf{Q}_{i,j}^T = \mathbf{I}, \tag{3.186}$$

equation (3.184) becomes

$$\left|\mathbf{F}_{i,j}\mathbf{X}_i - \mathbf{G}_{i,j}\right| = \mathbf{M}_{i,j}^T\mathbf{M}_{i,j} + \delta_{i,j}^2, \tag{3.187}$$

where

$$\delta_{i,j}^2 = \mathbf{G}_{i,j}^T\left(\mathbf{I} - \mathbf{Q}_{i,j}\mathbf{Q}_{i,j}^T\right)\mathbf{G}_{i,j}, \tag{3.188}$$

$$\mathbf{M}_{i,j} = \mathbf{R}_{i,j}\mathbf{X}_i - \mathbf{Q}_{i,j}^T\mathbf{G}_{i,j}. \tag{3.189}$$

Assembling the set of equations (3.187) for every (i, j) entry of the fitted matrix function, the objective function to be minimized becomes

$$\min\left(\varepsilon = \mathbf{M}^T\mathbf{M} + \delta^2\right). \tag{3.190}$$

On the other hand, the requirement of the existence of a positive real matrix $\mathbf{P}$ as given by the positive real lemma (see section 2.1.7), together with positive definiteness of asymptotic matrices result in the following optimization problem constraints

$$\text{s.t.} \quad \begin{bmatrix} \mathbf{A}^T\mathbf{P} + \mathbf{P}\mathbf{A} & \mathbf{P}\mathbf{B} - \mathbf{C}^T \\ \mathbf{B}^T\mathbf{P} - \mathbf{C} & -\left(\mathbf{D} + \mathbf{D}^T\right) \end{bmatrix} \le 0, \quad \mathbf{P}, \mathbf{D}, \mathbf{E} > 0 \tag{3.191}$$

Since both, the objective function and constraints are convex functions, they can be solved using semidefinite programming techniques [43]. In this thesis, the SDP-based passivity enforcement approach is adopted from [61], which uses the Matlab-based CVX optimization package [62, 63].

3.4 Conclusions

This chapter presents theoretical review of existing VF, MPM and LM fitting techniques. Additionally, a modified LM technique is proposed. Unlike the traditional LM method, the proposed technique is advantageous since the obtained model is sparse (more efficient in time-domain simulations). Also, the procedure for extracting unstable poles is more straightforward compared to traditional methodologies.

In addition to the review of fitting methods, existing passivity assessment methods such as, frequency sweeping, Hamiltonian matrix and singularity test matrix are revisited. Finally, existing passivity enforcement techniques, such as Fast Residue Perturbation (FRP), Hamiltonian Matrix Perturbation (HMP) and Semidefinite Programming (SDP)-based techniques are studied.

CHAPTER 4 NUMERICAL COMPARISONS OF FITTING TECHNIQUES

In this chapter, the VF, MPM and LM fitting techniques, introduced in Chapter 3, are compared via different case studies. As for the LM technique, the modified LM technique presented in Chapter 3 is used. The objective of this chapter is to demonstrate the capabilities of the studied techniques, and at the same time, to set a basis for a novel fitting methodology proposed in this thesis (presented in Chapter 5). The study of passivity is not covered in this chapter since no difference (in terms of passivity) has been observed among the studied techniques, i.e., all the studied techniques are prone to produce models with passivity violations. The study of passivity is covered in Chapter 6.

As mentioned in Chapter 1, the CPU performances given in this thesis are obtained using a 16-GB of RAM, i7-4900MQ@2.80 GHz processor and 64-bit Windows operating system computer.

4.1 Fitting accuracy

To evaluate the accuracy of the studied fitting techniques, the RMS and relative fitting errors are compared for each case study. The RMS (ε_{RMS}) and relative ($\varepsilon_{relative}$) fitting error are calculated as follows

$$\varepsilon_{RMS} = \sqrt{\sum_{k=1}^{N_s}\sum_{n=1}^{N_e}\left|\mathbf{f}_n(s_k) - \mathbf{f}'_n(s_k)\right|^2 / (N_s N_e)}, \tag{4.1}$$

$$\varepsilon_{relative} = \sum_{k=1}^{N_s}\sum_{n=1}^{N_e}\left[\frac{\mathbf{f}_n(s_k) - \mathbf{f}'_n(s_k)}{\mathbf{f}_n(s_k)} \times 100\right] / (N_s N_e), \tag{4.2}$$

where $\mathbf{f}$ is the vector containing the elements of the lower triangular part of the fitted matrix function, as defined in (3.31); N_e denotes the number of elements in $\mathbf{f}$, as given in (3.32); N_s denotes the number of frequency samples, as indicated in (2.2); and $\mathbf{f}'$ denotes the fitted function (analogous to $\mathbf{f}$).

4.2 Case study 1: analytical function

To start the numerical comparisons of the VF, MPM and LM methods, the analytical function

$$f(s)=\frac{2}{s+5}+\frac{30+j40}{s-(-100+j500)}+\frac{30-j40}{s-(-100-j500)}+0.5, \tag{4.3}$$

is first studied due to its simplicity. As it can be inferred from (4.3), such function contains a pair of complex conjugate poles and a real pole, in addition to an asymptotic term. Thus, the order of the function in (4.3) is $N=3$. This function is numerically evaluated from 0 to 1 kHz with 201 linearly spaced samples (the number of samples has been defined arbitrarily).

As first test, the frequency-samples of the function in (4.3) are fitted with VF, MPM and LM techniques using the correct model order $N=3$ and non-zero d coefficient. The resulting fitting magnitude curves are shown in Figure 4.1.

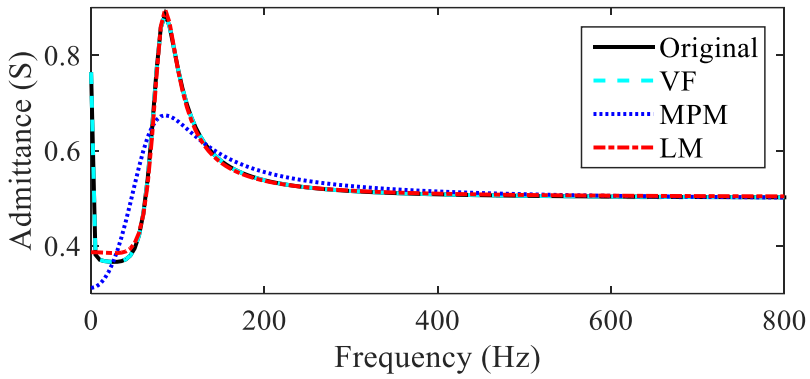

Figure 4.1. Magnitude of the frequency response of the analytical function (4.3) together with the fitted counterparts by VF, MPM and LM techniques.

The poles and residues obtained via the VF technique result in a perfect match with (4.3), whereas the residues/poles obtained via MPM are

$$f_{MPM}(s)=\frac{25}{s+2641}+\frac{34+j77}{s-(-259+j385)}+\frac{34-j77}{s-(-259-j385)}+0.496, \tag{4.4}$$

and those obtained via LM are

$$f_{LM}(s)=\frac{7\times10^{5}}{s+2\times10^{6}}+\frac{29+j36}{s-(-93+j506)}+\frac{29-j36}{s-(-93-j506)}+0.14. \tag{4.5}$$

From (4.4) and (4.5), it can be observed that the approximations given by MPM and LM are considerably different to the original function. The RMS and relative errors by the three techniques are listed in Table 4.1. Based on both fitting errors and function coefficients, it can be observed that VF performs the best fitting for the selected order $N=3$.

Table 4.1. Comparison of fitting accuracy for the analytical function (4.3) with $N=3$.

Technique	ε_{RMS}	$\varepsilon_{relative}$
VF	2.40×10^{-16}	4.45×10^{-14} %
MPM	2.81×10^{-2}	1.09 %
LM	6.15×10^{-2}	4.84 %

As studied in Chapter 3, the singular values obtained from the MPM and LM pencil functions can be used to identify the function order. For the current case study, the MPM and LM singular values are shown in Figure 4.2 (only the first forty singular values are shown for clarity). This figure reveals that the LM curve show an abrupt drop at the fourth singular value, revealing the order of the system (including the d coefficient). This result agrees with the observations reported in [59]. On the other hand, the singular values of the MPM pencil function show a monotonous downward curve, which makes difficult the identification of the function order.

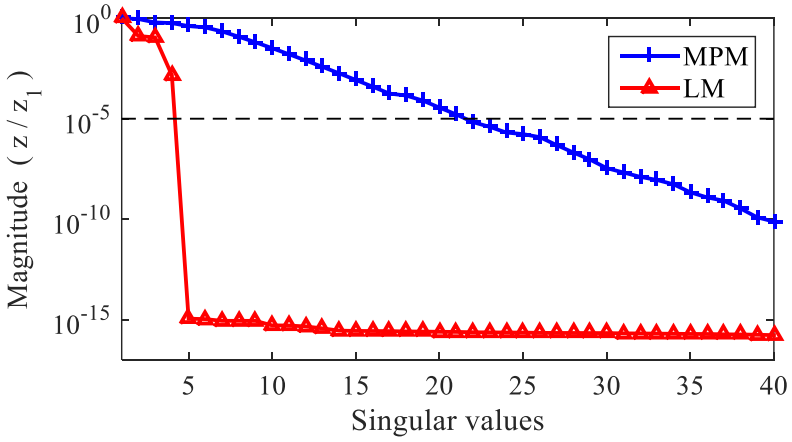

Figure 4.2. MPM- and LM-pencil singular values for the fitting of the function (4.3).

To illustrate the model order identification capabilities by using the parameter ξ for MPM and LM techniques, as discussed in Chapter 3, Figure 4.2 also shows the application of the threshold value $\xi=1\times10^{-5}$ as marked by the dashed-line. The resulting model orders by using this method are

$N = 4$ and $N = 21$ for LM and MPM techniques, respectively. These numbers correspond to the number of singular values with magnitude above the selected parameter ξ.

Using the model orders obtained from this test, the MPM fitting results considerably more accurate, but at the cost of a substantial increase of the model order ($N = 21$). On the other hand, the fitting by the LM method with order $N = 4$ becomes poorer in terms of accuracy. The corresponding fitting errors are given in Table 4.2. The conclusion of this numerical test for the LM technique is that the sudden drop in the singular values includes the asymptotic term d. This must be considered to appropriately determine the model order.

Table 4.2. Comparison of fitting accuracy for the analytical function (4.3) using $\xi = 1\times10^{-5}$ for model order identification via MPM and LM techniques.

Technique	**Order**	ε_{RMS}	$\varepsilon_{relative}$
MPM	21	1.08×10^{-6}	1.26×10^{-4} %
LM	4	7.7×10^{-2}	6.26 %

Further analysis for the MPM and LM techniques applied to the studied function (4.3) is presented next. From Chapter 3, it has been studied that the MPM technique consists of an approximation of a function as a sum of complex exponentials in TD, which is equivalent to the poles/residues approximation of the rational model in FD. The MPM technique, however, does not consider the asymptotic terms d and/or e, during the pole identification stage (section 3.1.2.1). Similarly, the LM method calculates a state-space model without considering the asymptotic matrices $\mathbf{D}$ and/or $\mathbf{E}$ (section 3.1.3). Then, a hypothesis is that the MPM and LM techniques try to fit the studied function (4.3) (and any function) by using only the residues and poles, and for this reason, when the contribution of asymptotic terms is substantial, large deviations are obtained.

A new test for the fitting of function (4.3) via MPM and LM is performed with the asymptotic term d (0.5) subtracted. This is achieved only for the pole identification stage. For this test, once the poles have been identified, the residues and d constant are calculated using the original function (4.3). The resulting fitting by MPM becomes

$$f_{MPM}(s) = \frac{1.62}{s+4.04} + \frac{29 + j39.25}{s-(-96.52 + j498.52)} + \frac{29 - j39.25}{s-(-96.52 - j498.28)} + 0.5\,. \qquad (4.6)$$

This new approximation is considerably closer to the original function than the first attempt (4.4). The new approximation by LM results into a perfect match with the original function (4.3). These results demonstrate that both, the MPM and LM techniques can be optimally applied by subtracting the asymptotic components (if possible) during the pole identification stage.

Subtracting the asymptotic component has another important consequence for the MPM technique, i.e., the singular values curve now reveals the correct function order as shown in Figure 4.3, where a drop at the third singular value is observed.

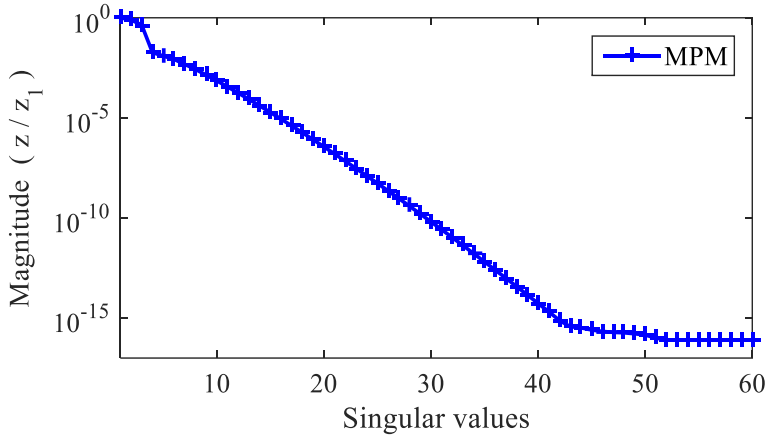

Figure 4.3. MPM-pencil singular values for the fitting of the function (4.3) with the asymptotic term d subtracted.

Finally, the RMS and relative errors for all the different fittings applied to the analytical function (4.3) are summarized in Table 4.3. This table shows that although the accuracies of MPM and LM techniques are considerably improved by applying subtraction of the asymptotic parameter d, the VF technique still achieves the most accurate fitting.

Table 4.3. Summary of the fitting errors for the analytical function (4.3) for different fitting techniques and model orders.

Technique	**Order**	ε_{RMS}	$\varepsilon_{relative}$
VF	3	2.40×10^{-16}	4.45×10^{-14} %
MPM	3	2.81×10^{-2}	1.09 %
	21	1.08×10^{-6}	1.26×10^{-4} %
MPM (d subtracted)	3	2.25×10^{-3}	0.27 %
LM	3	6.15×10^{-2}	4.84 %
	4	7.7×10^{-2}	6.26 %
LM (d subtracted)	3	6.29×10^{-16}	1.22×10^{-13} %

4.3 Case study 2: power transformer

As second case study, the zero-sequence admittance function of a 11kV/230V transformer, taken from [19], is fitted using the VF, MPM and LM techniques. First, to determine the model order, the MPM and LM pencil singular values are computed, the resulting curves are shown in Figure 4.4. This figure shows that for both, MPM and LM techniques, an abrupt drop is observed at the sixth singular value, suggesting the model order $N = 6$. Unlike the previous case study, the asymptotic d term is difficult to be determined (to be later subtracted) since the function vanishes too smoothly at high frequencies.

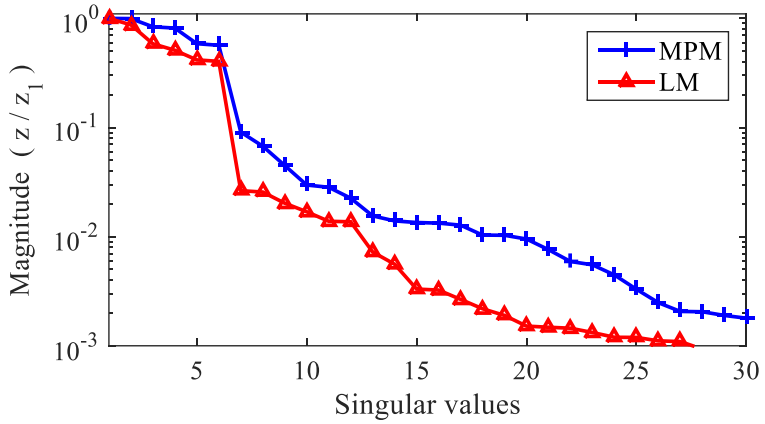

Figure 4.4. MPM- and LM-pencil singular values for the admittance function of the 11kV/230V transformer case study.

Fitting the outlined zero-sequence transformer admittance function with the obtained model order $N = 6$, the magnitude plot shown in Figure 4.5 is obtained. This figure shows that the VF and LM techniques achieve very accurate fittings while MPM fitting is noticeable less accurate.

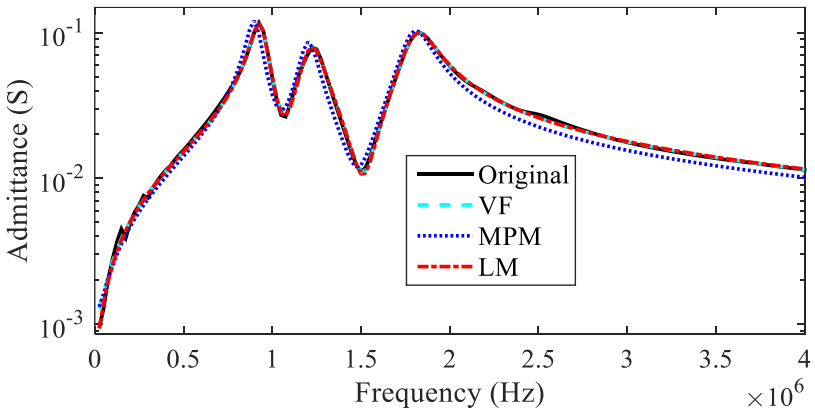

Figure 4.5. Magnitude fitting curves for the 11kV/230V transformer case study.

The corresponding RMS and relative fitting errors are listed in Table 4.4. From this table it is found that the LM method achieves the most accurate fitting for this case study, although both RMS and relative fitting errors given by VF are very close to those of the LM technique. Note that for this example, the application of the parameter ξ is not necessary since the model order is clearly revealed by the singular values, for both MPM and LM techniques.

Table 4.4. Comparison of fitting accuracy for the transformer case study with $N = 6$.

Technique	ε_{RMS}	$\varepsilon_{relative}$
VF	1.17×10^{-3}	6.32 %
MPM	8.68×10^{-2}	24.68 %
LM	1.09×10^{-2}	4.89 %

4.4 Case study 3: pi-circuit

The study of multiport systems is introduced by fitting the admittance matrix of the circuit of Figure 4.6, whose admittance matrix seen from nodes 1 and 2 is measured for a finite frequency band and fitted. The admittances Y_a, Y_b, and Y_c of the circuit are given in (4.7), (4.8), and (4.9), respectively. Since the set of admittances of the studied circuit contain a total of nine partial fractions, and a common set of poles is used for all the elements of the admittance matrix, the optimal fitting order is $N = 9$ for this case study.

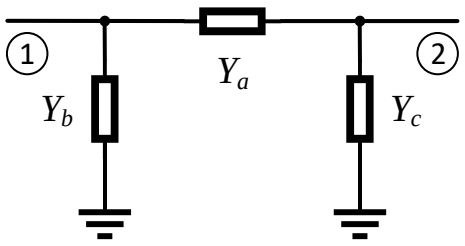

Figure 4.6. Pi circuit case study.

$$Y_a(s) = \frac{2}{s+5} + \frac{20+j50}{s-(-30+j1000)} + \frac{20-j50}{s-(-30-j1000)} + 0.4, \tag{4.7}$$

$$Y_b(s) = \frac{6}{s+12} + \frac{17+j30}{s-(-35+j3000)} + \frac{17-j30}{s-(-35-j3000)} + 0.2, \tag{4.8}$$

$$Y_c(s) = \frac{4}{s+10} + \frac{12+j24}{s-(-15+j5500)} + \frac{12-j24}{s-(-15-j5500)} + 0.3, \tag{4.9}$$

For model order identification via the LM technique, the LM-pencil singular values are expected to show an abrupt drop at the 12th singular value (considering the nine poles plus the three d constants of admittances Y_a, Y_b, and Y_c). However, the LM pencil singular values, shown in Figure 4.7, reveal its largest drop at the 11th singular value. Then, subtracting the three asymptotic terms, the resulting model order given by the LM technique is $N = 8$.

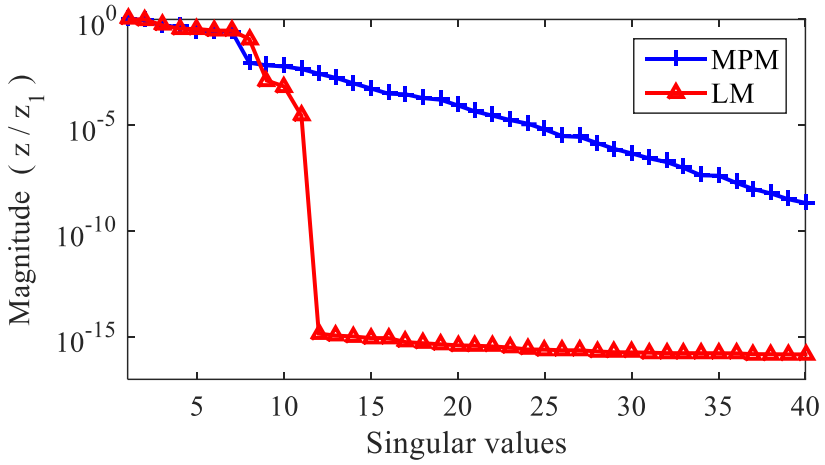

Figure 4.7. MPM- and LM-pencil singular values for the admittance matrix of the circuit of Figure 4.6.

As for the MPM technique, the singular values draw a smooth curve due to the presence of the asymptotic d constants in the function, as occurred for the fitting of the analytical function (case study 1). After the subtraction of these asymptotic terms, the MPM singular values (also shown in Figure 4.7), show a sudden drop at the seventh singular value, suggesting the order $N = 7$.

Then, in terms of model order identification for this example, it is concluded that, although neither the MPM nor the LM technique can exactly identify the model order, close estimations are obtained.

As a first fitting test by the VF, MPM and LM techniques, the admittance matrix of the circuit of Figure 4.6 with model order $N = 9$ and non-zero $\mathbf{D}$ matrix is achieved. The resulting magnitude plots are shown in Figure 4.8 (a), (b) and (c). These figures show that all the studied techniques can accurately fit the admittance matrix for the optimal model order.

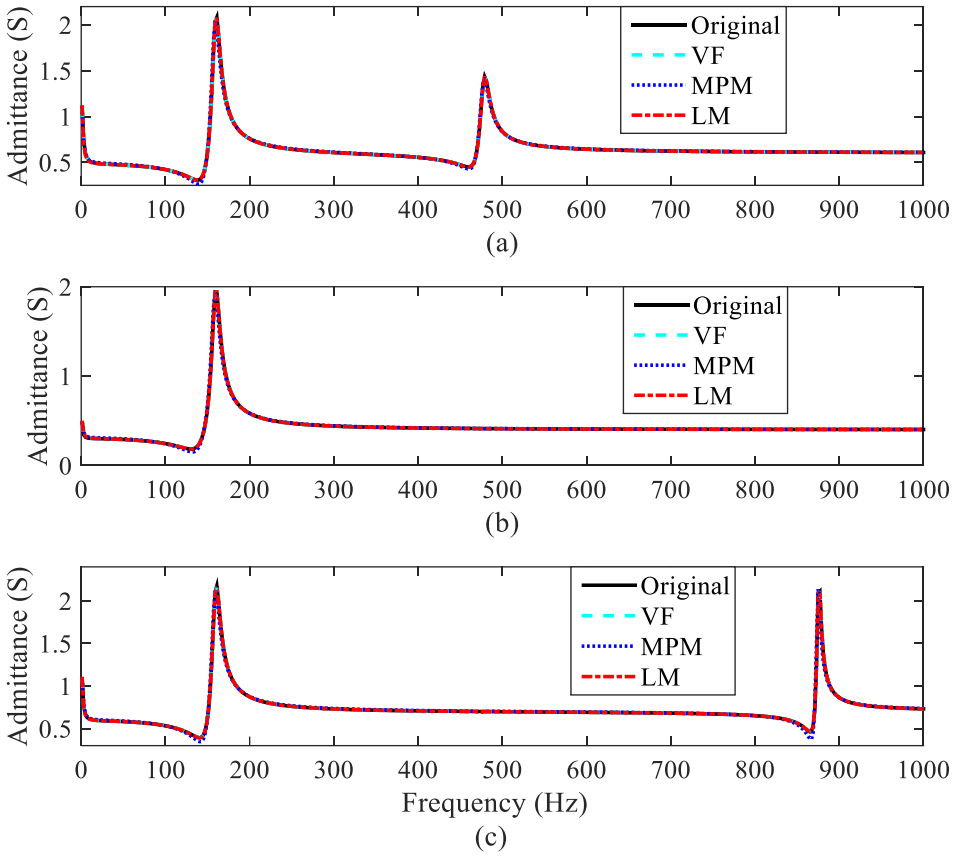

Figure 4.8. Magnitude of the elements of the admittance matrix of the circuit of Figure 4.6 and fitted counterparts by the VF, MPM and LM techniques, (a) element $\mathbf{Y}(1,1)$, (b) element $\mathbf{Y}(1,2)$ and (c) element $\mathbf{Y}(2,2)$.

To further assess the performance of the studied fitting techniques, the fitting is repeated using the model orders $N=7$ and $N=8$ as obtained from the singular values of the MPM and LM pencil functions, respectively. The RMS and relative errors for the different orders tested (including the first test $N=9$) are listed in Table 4.5. This table shows that although the three techniques achieve accurate fittings for the proposed model orders, the VF technique achieves the most accurate fittings in all cases. Special attention should be given to the fitting with the appropriate model order ($N=9$), for which the fitting accuracy by the VF technique is far better than MPM and LM techniques.

Table 4.5. Comparison of fitting techniques for the fitting of the admittance matrix of the circuit of Figure 4.6.

Technique	**Model order** (N)	ε_{RMS}	$\varepsilon_{relative}$
VF	7	2.20×10^{-3}	8.33×10^{-2} %
MPM		2.96×10^{-2}	2.04 %
LM		3.13×10^{-2}	1.37 %
VF	8	2.13×10^{-4}	1.0×10^{-2} %
MPM		2.66×10^{-2}	1.77 %
LM		2.77×10^{-2}	0.94 %
VF	9	**5.10×10^{-15}**	**2.69×10^{-13} %**
MPM		2.68×10^{-2}	1.72 %
LM		2.22×10^{-3}	8.6×10^{-2} %

4.5 Case study 4: distribution network

A more challenging case, such as the fitting of the frequency-response of the distribution network shown in Figure 4.9, is studied. This example is taken from [64] and illustrates the application of rational modeling for FDNEs. The magnitude plot of the elements of the admittance matrix of the network of Figure 4.9, measured from nodes **A** and **B**, is shown in Figure 4.10.

The MPM and LM techniques are used to determine the appropriate model order. Figure 4.11 shows the singular values by the MPM and LM techniques. This figure shows that neither the LM nor the MPM pencil singular values exhibit any large drop. Then, a numerical analysis for distinct threshold values ξ for model order identification is performed next.

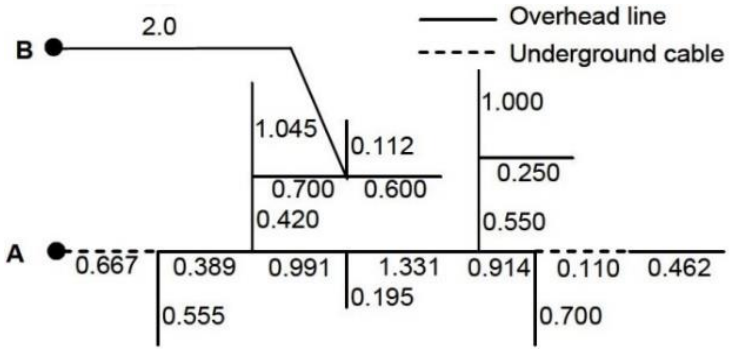

Figure 4.9. Distribution network case study, taken from [64].

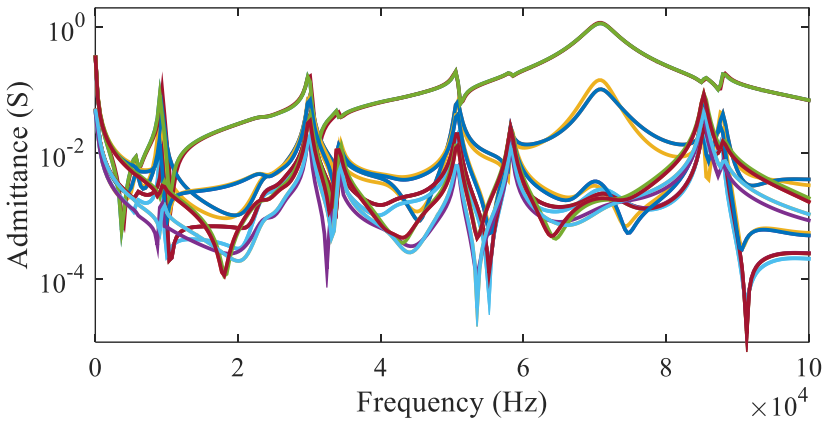

Figure 4.10. Magnitude of the elements of the admittance matrix of the distribution network of Figure 4.9 measured from nodes **A** and **B**.

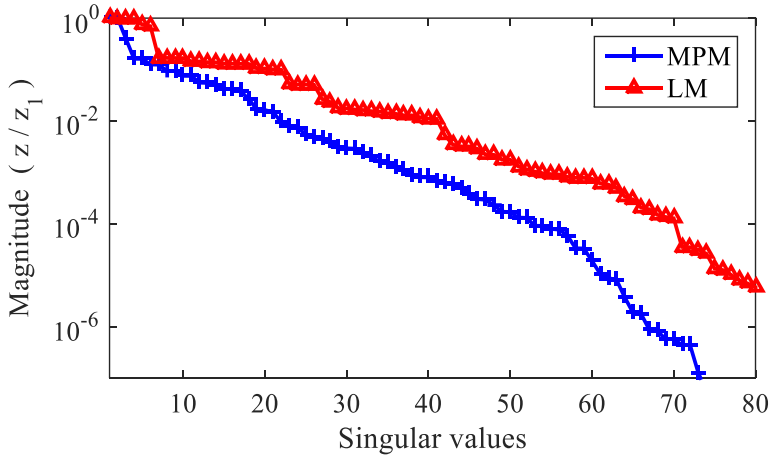

Figure 4.11. MPM- and LM-pencil singular values for the admittance matrix of the distribution network of Figure 4.9.

In theory, by reducing the tolerance value ξ, more singular values are considered as dominant, such that a higher model order is obtained, and consequently, a better fitting accuracy is expected. By applying different values of the parameter ξ, the fitting of the admittance matrix of the distribution network of Figure 4.9 is achieved using MPM and LM techniques. The resulting RMS errors are shown in Figure 4.12. This figure reveals that the RMS error by MPM converges to a certain value (about 1×10^{-3}) as ξ tends to zero (towards the left side in Figure 4.12), whereas for the LM method, the RMS error varies almost linearly with ξ. This fact suggests a better control of the fitting accuracy by the LM technique for this case study.

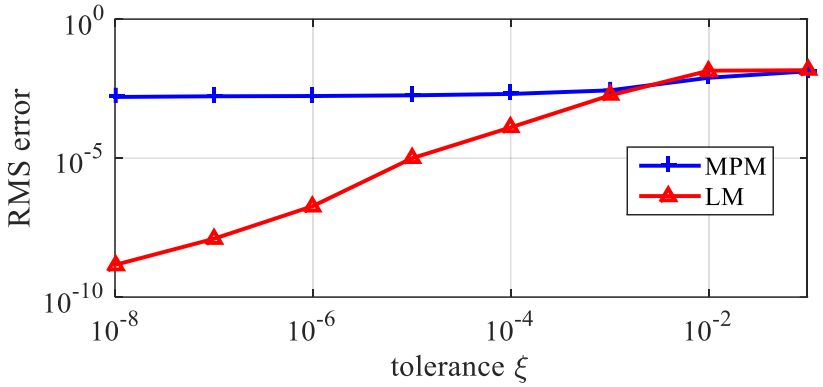

Figure 4.12. RMS error resulting from using different tolerance values ξ via MPM and LM for the fitting of the distribution network of Figure 4.9.

Another observation is pointed out for this example as follows. It has been confirmed that by reducing the tolerance value ξ for MPM and LM techniques, the model order is increased. The model order is, however, desired to be the lowest possible for better computational performance of the model in transient simulations. Then, it is interesting to observe the relationship between model order (N) and the fitting error, as shown in Figure 4.13. This figure reveals that for the model orders tested, the VF technique achieves the lowest fitting error in all cases. Note that for this test, the relative error has been used, although, a similar pattern is observed using the RMS error.

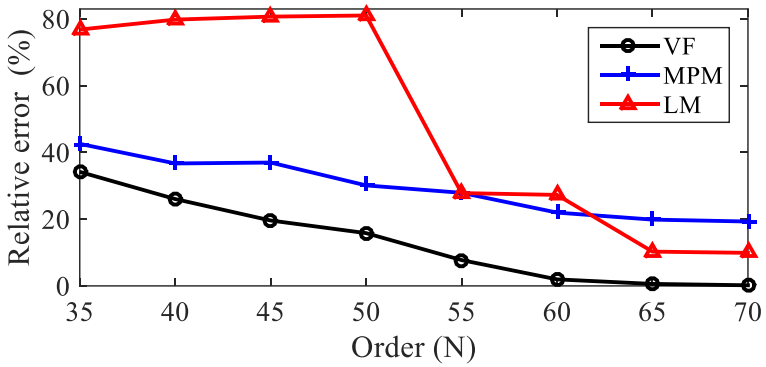

Figure 4.13. Relative fitting errors by VF, MPM and LM, for different fitting orders for the fitting of the admittance matrix of the distribution network of Figure 4.9.

4.6 Case study 5: cross-bonded cable system

As final case study for this chapter, the 225-kV cross-bonded transmission cable system introduced in Chapter 1 (Figure 1.4) is used for the computation of an equivalent transient model. The studied cross-bonded cable is constituted of 17 cable sections, each of them, built of three cable subsections with corresponding transpositions as shown in Figure 4.14. The geometry of the outlined 225-kV cable is shown in Figure 4.15 and its parameters are given in Table 4.6. Each cable subsection in Figure 4.14 is represented by the wideband model in EMTP, which is based on [52, 65, 66]. The total cable length is 64 km.

The magnitude plot of the elements of the admittance matrix of the studied cross-bonded cable, measured from sending and receiving terminals, is shown in Figure 4.16. The frequency-response of the outlined transmission cable system is measured from 0.1 Hz to 5 kHz with 2500 linearly spaced samples.

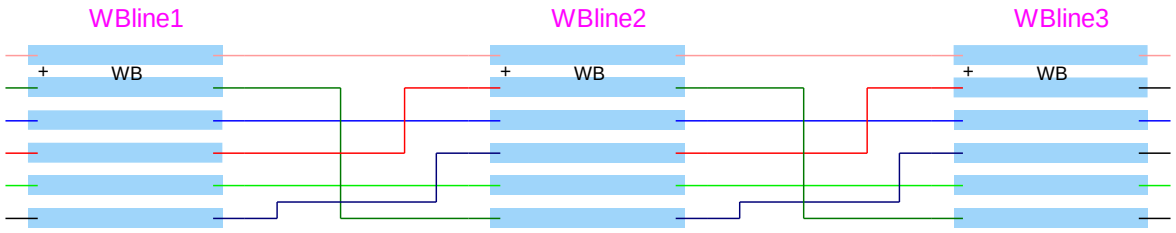

Figure 4.14. Cross-bonded cable subsection.

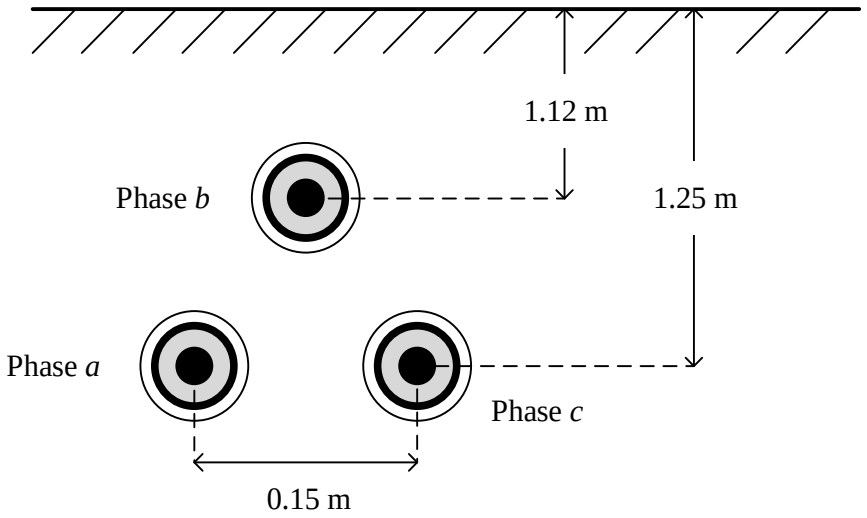

Figure 4.15. Geometry of the studied 225-kV cross-bonded cable system.

Table 4.6. Parameters of the 225-kV cable system of Figure 4.15.

Component	Parameter	Value
Core conductor	radius	28.4 mm
	resistivity	2.6×10^{-8} Ω·m
Core insulation	relative permittivity	3.23
Metallic sheath	internal radius	56.4 mm
	external radius	57.2 mm
	resistivity	2.84×10^{-8} Ω·m
Outer insulation	radius	62.2 mm
	relative permittivity	0.321
Soil	resistivity	100 Ω·m
Sheath grounding	resistance	5 Ω

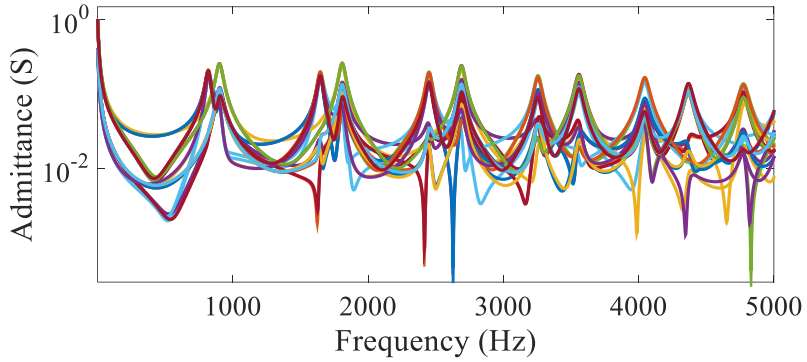

Figure 4.16. Magnitude of admittance matrix elements of the cross-bonded cable system.

The singular values obtained from the application of MPM and LM methods are shown in Figure 4.17. This figure shows smooth curves that do not reveal the order of the system. Then, different values for the parameter ξ are tested, the resulting model orders are listed in Table 4.7.

Table 4.7. Resulting model orders for different threshold values ξ for the 225-kV cable system of Figure 4.15.

Threshold (ξ)	MPM	LM
1×10^{-2}	27	42
1×10^{-3}	36	52
1×10^{-4}	46	67
1×10^{-5}	54	89
1×10^{-6}	62	117

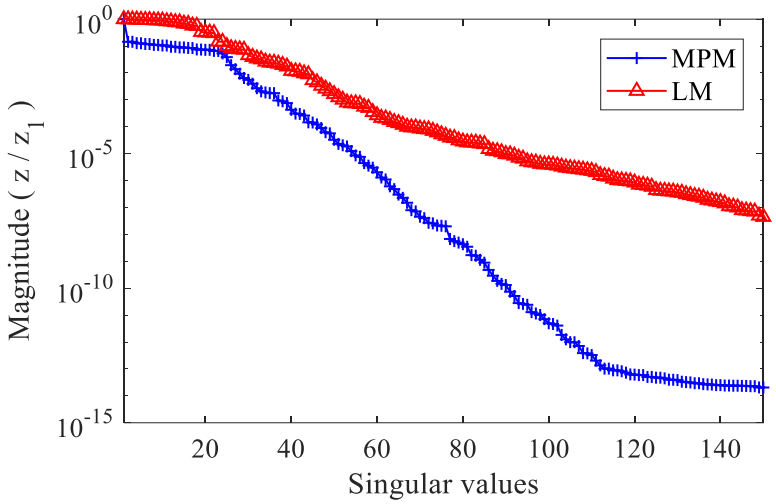

Figure 4.17. MPM- and LM-pencil singular values for the admittance matrix of the cable system of Figure 4.15.

This case study also unveils a disadvantage of the MPM and LM techniques, i.e., when the number of fitting frequency samples is substantial, the fitting CPU time may be excessively long. Then, some parameters intrinsic to these methods should be appropriately tuned as follows.

The resulting fitting errors and CPU times for the fitting of the studied transmission cable system with $N = 50$ (chosen arbitrarily) are listed in Table 4.8. As for the MPM method, Table 4.8 shows the fitting results for different values of the parameter k. As it is explained in Chapter 3, this parameter defines the number of samples of the inverse-Fourier-transformed function. In theory, the larger this value is, the more accurate TD function is obtained, and, consequently a more accurate fitting is expected. However, Table 4.8 shows that an overestimation of k causes excessively long computations. In previous case studies, k is set to 3, but for this case, setting $k = 1$ results in the best option for a reasonable CPU fitting time. Moreover, it is noted that selecting $k = 0$ is not a practical choice since a very poor fitting in terms of accuracy is obtained.

As for the LM fitting technique, Table 4.8 shows that using MFTI interpolation data results in substantially longer CPU fitting time compared to using VFTI data. Although in previous case studies, MFTI is used (because of a superior accuracy observed), for this case study, the VFTI is the best choice since it is considerably faster. Moreover, from Table 4.8, no significant difference is observed by using MFTI or VFTI data in terms of fitting error. Finally, by comparing both the RMS and the relative fitting errors of all cases in Table 4.8, it is observed that VF achieves the lowest error as in most case studies presented.

Table 4.8. Fitting errors and CPU times for the fitting of the cable system of Figure 4.16 with fitting order $N = 50$, applying the VF, MPM and LM techniques.

Technique	ε_{RMS}	$\varepsilon_{relative}$	**CPU** (s)
VF	1.40×10^{-5}	6.6×10^{-2} %	6.5
MPM $k = 4$	1.71×10^{-3}	2.53 %	473
MPM $k = 3$	1.71×10^{-3}	2.53 %	418
MPM $k = 2$	1.71×10^{-3}	2.51 %	57
MPM $k = 1$	1.71×10^{-3}	2.50 %	7.5
MPM $k = 0$	1.30×10^{-2}	25.09 %	1.5
LM MFTI	2.08×10^{-3}	1.27 %	1847
LM VFTI	2.09×10^{-3}	1.32 %	11.8

4.7 Discussion

From the presented numerical tests, the most important observation is that for most of the fittings achieved, the VF method is the most accurate among the studied techniques. It has been also verified that the MPM and LM techniques can reach similar fitting accuracy as the VF technique but at the cost of increasing the model order, which is undesirable for model efficiency in time-domain simulations. These facts suggest that the VF technique is the preferable option in terms of fitting accuracy.

A particular advantage of the MPM and LM techniques is that, in principle, they provide a tool for model order identification as dictated by the abrupt drops in the singular values. However, as it has been demonstrated with numerical examples, a clear abrupt drop in the singular values does not always appear. Then, fitting accuracy must be tuned by appropriate selection of the threshold parameter ξ.

For the fitting of low-order models, such as the synthetic function, pi-circuit and transformer examples presented, the MPM and LM singular values normally show a clear abrupt drop, which allows a straightforward model order identification. Also, it was found that the extraction of asymptotic components for smooth functions permits a better identification of the poles of the function, which consequently, improves the fitting accuracy. Additionally, in some cases, after the extraction of the asymptotic components, the function order can be better revealed by the singular values.

For highly resonant frequency responses, such as the distribution network and the cross-bonded cable system cases presented, both, the MPM and LM singular values usually draw monotonous downward curves. Then, for those cases, the model order should be determined by the application of the threshold parameter ξ. Using the parameter ξ, the LM technique was observed to be more sensitive controlling the fitting error as occurred with the distribution system FDNE case study.

As for the fitting of the cross-bonded cable system, it was demonstrated that when a substantial number of frequency samples is used for the MPM and LM techniques, the required computational burden could be prohibitively expensive under certain circumstances. In the case of the MPM technique, the number of samples required in the IFFT was found to have an important impact on the computational efficiency. As for the LM technique, the format of the tangential interpolation data (VFTI or MFTI) should be appropriately selected, being the VFTI format the most efficient option.

4.8 Conclusions

This chapter has presented a comparison of the VF, MPM, and LM fitting techniques through the fitting of different frequency-domain functions. The presented examples show that the VF technique achieves the best trade-off between accuracy and model order. Nonetheless, it is shown that the MPM and LM techniques are practical tools for model order identification. From this analysis, it is concluded that the fitting order obtained via MPM or LM can be used as input to the VF technique.

Moreover, the numerical analysis presented in this chapter reveal the capabilities and the possible issues encountered when applying the MPM and LM techniques, such as the extraction of asymptotic components and the selection of certain parameters for the optimal application of these techniques.

Also, the novel modified implementation of the LM technique proposed in Chapter 3 has been tested, showing an acceptable (slightly poorer) performance compared to the VF method in terms of fitting accuracy; the proposed LM technique resulted into a better performance compared to the MPM technique.

CHAPTER 5 A NOVEL FITTING APPROACH

In Chapter 4, the VF, MPM and LM fitting techniques are evaluated through numerical examples. Among these techniques, it was found that the VF method achieves the most accurate fittings. Also, it was demonstrated that the MPM and LM techniques are useful tools for model order identification. In this chapter, the capabilities of the studied fitting techniques are combined leading to two possible methods, named hereafter as MPM-VF and LM-VF methods.

Before presenting the proposed fitting techniques, some important facts of special interest for the derived methods are analyzed: 1. the convergence of the pole relocation process by the VF method; 2. the impact of the model order on the model passivity; and 3. model order determination by the MPM and LM techniques.

5.1 Convergence of the pole relocation process by the VF method

As reviewed in Chapter 3, the VF technique computes the poles of the rational model (2.3) in an iterative pole relocation process. Then, the following question arises: How many iterations should be applied in this process?

Unfortunately, there is no answer to this question that well suits all cases. However, in this thesis two cases are observed: 1. for low-order models (less than 20 poles), the pole relocation process usually converges after a few iterations (about 5 iterations); 2. for high-order models, the pole relocation process may not converge, or it may require many iterations to achieve convergence.

To evaluate the convergence of the VF pole relocation process, the Hausdorff distance between the poles of consecutive iterations can be evaluated as suggested in [56] (section 7.4.2.1). The Hausdorff distance is calculated as follows

$$Hdist = \max\left\{dist\left(\mathbf{a}_k, \mathbf{a}_{k-1}\right), dist\left(\mathbf{a}_{k-1}, \mathbf{a}_k\right)\right\}, \tag{5.1}$$

where $\mathbf{a}_k$ denotes the vector containing the poles of the k^{th} iteration, and the operator $dist(\ )$ denotes the one-sided distance between the elements of the first argument respect to those of the second. The one-sided distance is defined as

$$dist\left(\mathbf{a}_k, \mathbf{a}_{k-1}\right) = \max\left\{\mathrm{d}\left(a_i, \mathbf{a}_{k-1}\right), a_i \in \mathbf{a}_k\right\}. \tag{5.2}$$

The operator $\mathrm{d}(\ )$ in (5.2), represents the distance between a single pole respect to the other set of poles as follows

$$\mathrm{d}\left(a_i, \mathbf{a}_{k-1}\right) = \max\left\{\left|a_i - \bar{a}_i\right|, \bar{a}_i \in \mathbf{a}_{k-1}\right\}. \tag{5.3}$$

To illustrate the convergence of the VF technique for the first case (low-order functions), it is recalled the fitting of the analytical function (4.3) studied in Chapter 4. Applying the VF technique with initial poles set as linearly-spaced frequency samples of the fitting frequency band in rad/s, the initial poles ($\mathbf{a}_0$) and the poles obtained after the first pole relocation iteration ($\mathbf{a}_1$) are:

$$\begin{aligned} \mathbf{a}_0 &= \left[-0.6283 \quad -3.1419\times10^{3} \quad -6.2832\times10^{3}\right] \\ \mathbf{a}_1 &= \left[-5 \quad -100 - j500 \quad -100 + j500\right] \end{aligned}. \tag{5.4}$$

If one more iteration is applied, the resulting poles ($\mathbf{a}_2$) do not substantially change respect to those of $\mathbf{a}_1$. The Hausdorff distances resulting from the first and second pole relocation iterations are

$$\begin{aligned} Hdist_1 &= 6.95\times10^{3} \\ Hdist_2 &= 5.75\times10^{-11} \end{aligned}. \tag{5.5}$$

As it can be observed from (5.5), the Hausdorff distance at the second iteration is very small, then, convergence can be granted at this iteration. A pre-specified value can be set for the Hausdorff distance to declare convergence.

A similar situation occurs for the fitting of the zero-sequence transformer admittance function studied in Chapter 4, Section 4.3. For this example, the Hausdorff distances for the first 40 iterations of the pole relocation process are plotted in Figure 5.1 for model orders $N = 6$ and $N = 15$. As for the previous case, the initial poles have been selected as linearly spaced frequency samples of the fitting frequency band in rad/s. Figure 5.1 shows a clear convergence of the pole relocation process in both cases, however, it is observed that using the correct order $N = 6$ (as indicated by the drop in the singular values curve in Figure 4.4) convergence is achieved more rapidly. Also, it is interesting to observe that the Hausdorff distance does not fall below 1×10^{-10}.

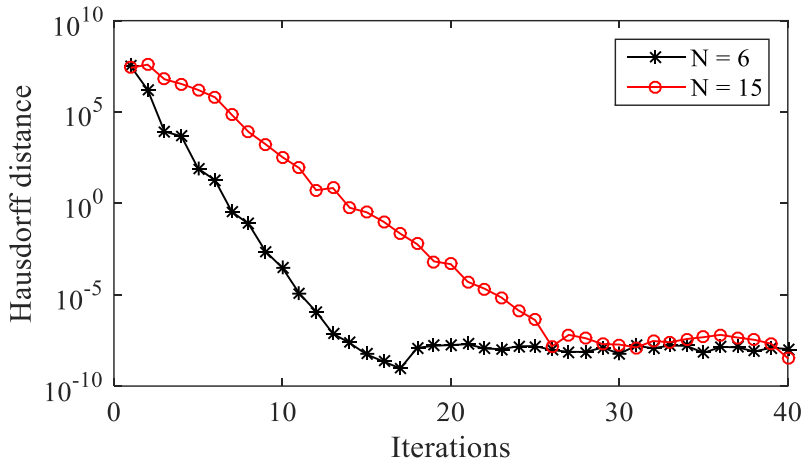

Figure 5.1. Convergence of the pole relocation process of the VF technique for the fitting of the transformer zero-sequence admittance.

To illustrate the case of high-order models, the fitting of the distribution system of Figure 4.9 is analyzed. For this example, the Hausdorff distances of the pole relocation process for model orders $N = 40$, $N = 60$ and $N = 80$ are shown in Figure 5.2. This figure shows that convergence is achieved more rapidly for the model order $N = 60$, which can be denoted as the appropriate model order. Also, it is observed that convergence for model orders $N = 40$ and $N = 80$ is achieved at a larger number of iterations compared to Figure 5.1.

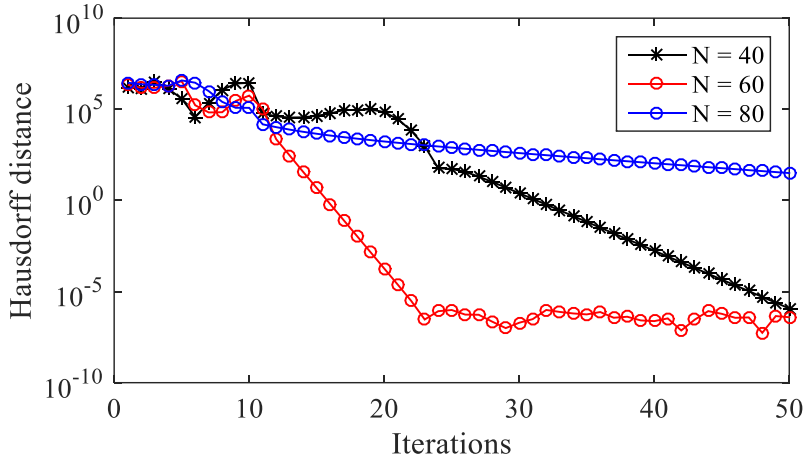

Figure 5.2. Convergence of the pole relocation process of the VF technique for the fitting of the distribution network of Figure 4.9 with different model orders.

The examples analyzed in this section reveal that the model order plays an important role in the convergence of the VF pole relocation process as follows. First, it has been observed that when the

model order has been appropriately selected, convergence is achieved more quickly than for poor model order estimations. Second, for high-order models, the number of iterations required to achieve convergence may be considerably larger.

5.2 Impact of the model order on passivity

To start with the analysis of the impact of the model order on the passivity of rational models, it is recalled from Chapter 4 that in most cases, by increasing the model order, higher fitting accuracy is obtained. This observation can be verified by inspecting Table 4.5 or Figure 4.13. To confirm this observation, a new numerical test for the fitting of the frequency-response of the distribution network of Figure 4.9, with different model orders, is achieved. The resulting RMS errors are listed in Table 5.1. This table confirms the abovementioned relationship between the model order and fitting error for the three techniques studied. From this analysis, one may think that the model order should be as high as possible to ensure high accuracy of the rational model. Nonetheless, by increasing the model order the computational burden in transient simulations is also increased. One more factor to consider is the passivity of the rational model as explained next.

Table 5.1. Comparison of the fitting accuracy by VF, MPM and LM for the fitting of the frequency-response of the distribution network of Figure 4.9 with different model orders.

Model order (N)	ε_{RMS}		
	VF	**MPM**	**LM**
45	1.78×10^{-4}	2.30×10^{-3}	1.39×10^{-2}
50	1.20×10^{-4}	2.06×10^{-3}	1.38×10^{-2}
55	1.83×10^{-5}	1.99×10^{-3}	1.78×10^{-3}
60	1.44×10^{-6}	1.86×10^{-3}	1.77×10^{-3}
65	1.34×10^{-7}	1.75×10^{-3}	1.31×10^{-4}

As studied in Chapter 3, the passivity of rational models can be evaluated by computing the Hamiltonian matrix defined in (3.87). The eigenvalues of the Hamiltonian matrix reveal the presence of negative eigenvalues of the Hermitian part of the model (conductance matrix for symmetrical systems) along the frequency axis, i.e., passivity violations. Non-passive rational models are prone to be numerically unstable in time-domain simulations.

Although passivity violations are unpredictable, in this thesis, it has been observed that using either a very-high or very-low model order, increases the probabilities of the model to violate the passivity condition (2.26). To illustrate this phenomenon, the fitting of the distribution network introduced in Chapter 4 is studied again. This time, the study is aimed to analyze the passivity violations resulting for different model orders. Then, the eigenvalues of the conductance matrix of the VF-fitted models with orders $N = 40$, $N = 60$ and $N = 80$ are shown in Figure 5.3.

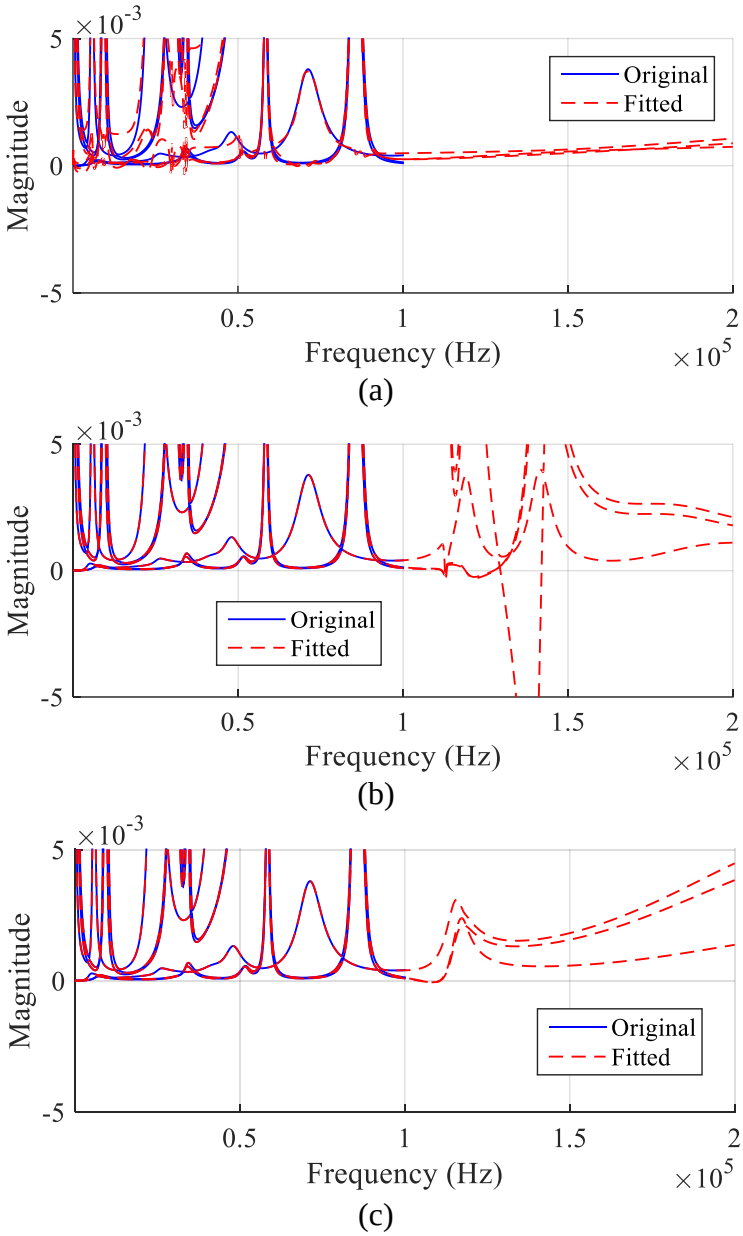

Figure 5.3. Eigenvalues of the conductance matrix of the VF-fitted model for the distribution network of Figure 4.9 with model orders: (a) $N = 40$, (b) $N = 80$ and (c) $N = 60$.

Figure 5.3 (a) illustrates the case with a very-low fitting order, such as $N = 40$. This figure shows that the eigenvalues of the fitted model barely match those of the original system (poor fitting). Also, it is observed that passivity violations appear anywhere along the fitting band (from 1 Hz to 100 kHz). Figure 5.3 (b) illustrates a very-high fitting order ($N = 80$). In this case, passivity violations appear outside of the fitting band (frequencies higher than 100 kHz). This occurs because of the presence of out-of-band poles, i.e., poles with resonant frequencies out of the fitting band. These poles produce uncontrolled behavior outside the fitting band. Finally, Figure 5.3 (c) shows that using a reasonable fitting order ($N = 60$), no passivity violations result. Although, in the worst scenario, slight passivity violations may appear, which are more likely to be easily removed by a suitable passivity enforcement method, such as those proposed in [40, 44, 67, 68]. Note that the model order found without passivity violations agrees with the optimal model order found in previous section regarding the convergence of the pole relocation process by the VF technique.

5.3 Model order determination by MPM and LM methods

As a complement of the two previous sections, using the same example (the distribution network of Figure 4.9), it is interesting to analyze the model order obtained by the MPM and LM techniques for different values of ξ, as given in Table 5.2. From this table, as it was shown in Chapter 3, it is confirmed that the resulting RMS fitting error decreases as the value ξ does. Also, it is observed that these two values show a very close agreement for the LM method (particularly for this case). This relationship suggest that the fitting accuracy can be controlled by adjusting the parameter ξ, making implicit the determination of the model order N.

Table 5.2. Model order identification by MPM and LM techniques applied to frequency-response of the distribution network of Figure 4.9.

Threshold value (ξ)	**MPM**		**LM**	
	N	ε_{RMS}	N	ε_{RMS}
1×10^{-2}	21	7.78×10^{-3}	41	1.39×10^{-2}
1×10^{-3}	37	2.61×10^{-3}	53	1.78×10^{-3}
1×10^{-4}	52	2.03×10^{-3}	70	1.29×10^{-4}
1×10^{-5}	61	1.84×10^{-3}	77	1.01×10^{-5}
1×10^{-6}	66	1.72×10^{-3}	91	1.97×10^{-7}

Additionally, considering the model order $N = 60$ as optimal in terms of both the convergence of the VF method and passivity violations, as demonstrated in previous sections, from Table 5.2, it can be found that the corresponding value for ξ to obtain that model order is about 5×10^{-4} and 1×10^{-5} for LM and MPM techniques, respectively. These values are taken as reference for the proposed fitting technique presented in next section.

5.4 Combined MPM-VF and LM-VF rational fitting approaches

Based on the analyses presented in previous sections of this chapter, a new fitting approach is proposed. The proposed approach constitutes a combination of either the MPM or the LM technique with the VF method as illustrated in the flowchart of Figure 5.4.

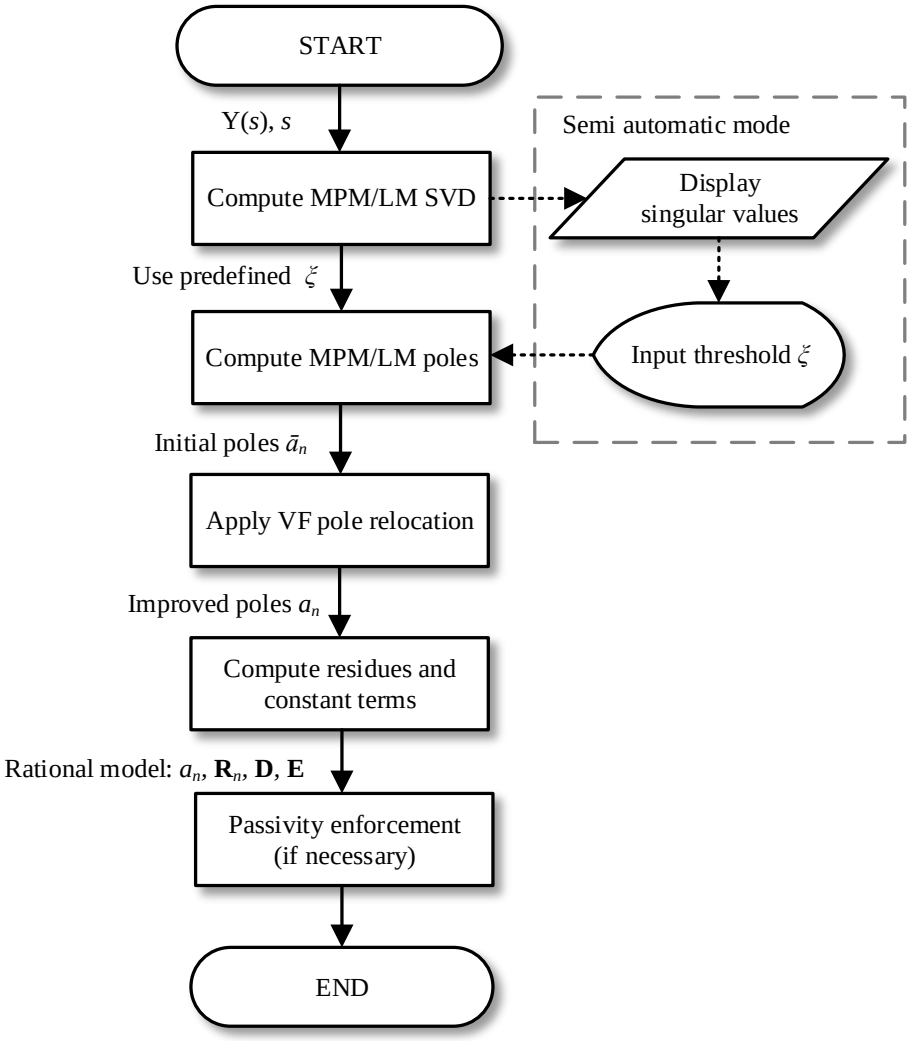

Figure 5.4. Flowchart of the proposed combined fitting approach.

As it can be observed in Figure 5.4, the proposed fitting methodology first computes the pencil function of either the MPM or the LM technique to identify the model order, subsequently, a set of initial poles is obtained by the previously selected technique. The resulting set of initial poles is, then, subject to the pole relocation process of the VF technique. Then, the residues and asymptotic components of the rational model are computed by applying the least-squares method as for the traditional VF technique. Finally, passivity enforcement is applied (if necessary).

From Figure 5.4, it can be observed that using a predefined threshold value ξ, the proposed technique determines the model order automatically. Alternatively, the proposed algorithm allows the inspection of the curve drawn by the corresponding pencil singular values and, based on the identification of an abrupt drop, to determine the appropriate model order. The alternative (semiautomatic) mode is illustrated by dashed lines in Figure 5.4.

As additional feature to the proposed method, the resulting RMS error can be compared with a tolerance value, then, if the RMS error is larger than the pre-defined tolerance, the fitting can be repeated with a smaller threshold value (ξ). The advantages and limitations of the proposed methodology are given next.

5.4.1 Advantages of the proposed technique

The proposed technique has the following advantages over the VF, MPM and LM techniques applied independently:

1. Unlike the VF method, there is no need of guessing the model order.
    a. In the automatic mode, the fitting accuracy is defined by ξ.
    b. In the semiautomatic mode, abrupt drops in the singular values can be identified to select the optimal value for ξ.
2. There is no need of selecting the nature of initial poles, i.e., they can be complex or real, and linearly or logarithmically spaced.
3. Since the poles obtained via MPM or LM are close to the final solution given by VF, fast convergence of the pole relocation process is achieved.
4. Since the initial poles (obtained either by the MPM or LM method) are relocated via VF, the high accuracy of the VF technique is preserved in the final solution.

5.4.2 Limitations of the proposed technique

In theory, the threshold value ξ used for model order identification is closely related to the final RMS fitting error as shown in Chapter 4 and confirmed experimentally in section 5.3. Unfortunately, this relationship is not always closely accomplished. Thus, there does not exist a value for ξ that is suitable for all cases.

On the other hand, like the existing fitting techniques, the proposed approach cannot guarantee passivity of the obtained rational models. However, as discussed in section 5.2, certain values for ξ achieve a good trade-off between the model order and passivity. Those values are further tested in the next section with numerical examples.

5.5 Evaluation of the proposed technique

5.5.1 Case study 1: overhead single-phase transmission line

The single-phase overhead transmission line presented in [69] is used here to evaluate the performance of the proposed fitting technique. The physical characteristics of this transmission line are given in Table 5.3.

Table 5.3. Single-phase transmission line physical characteristics.

Conductor radius	1.11 cm
DC resistance	0.1052 Ω/km
Height	11 m
Soil resistance	100 Ω·m
Length	25 km

The characteristic admittance $\mathbf{Y}_c(s)$ and propagation function $\mathbf{\Gamma}(s)$ of the studied transmission line are computed from 0.1 Hz to 10 MHz with 81 logarithmically-spaced samples using EMTP [50]. As for the $\mathbf{\Gamma}(s)$ function, the propagation delay $\tau = 8.41918\times10^{-5}$ s is extracted.

Using the proposed LM-VF fitting approach, both $\mathbf{Y}_c(s)$ and $\mathbf{\Gamma}(s)$ are fitted using the threshold value $\xi = 5\times10^{-4}$ for model order determination (as recommended in section 5.3). Note that the MPM technique is not suitable for logarithmically-spaced sampling. The resulting model orders are $N = 9$ and $N = 6$ for $\mathbf{Y}_c(s)$ and $\mathbf{\Gamma}(s)$, respectively.

The resulting magnitude plots are shown in Figure 5.5. This example shows the effectiveness of the proposed method for the automatic computation of rational models while achieving high fitting accuracy. Also, it is worth to mention that the poles obtained by the proposed LM-VF method are the same as those obtained via the VF technique, i.e., the high accuracy of the VF method is preserved.

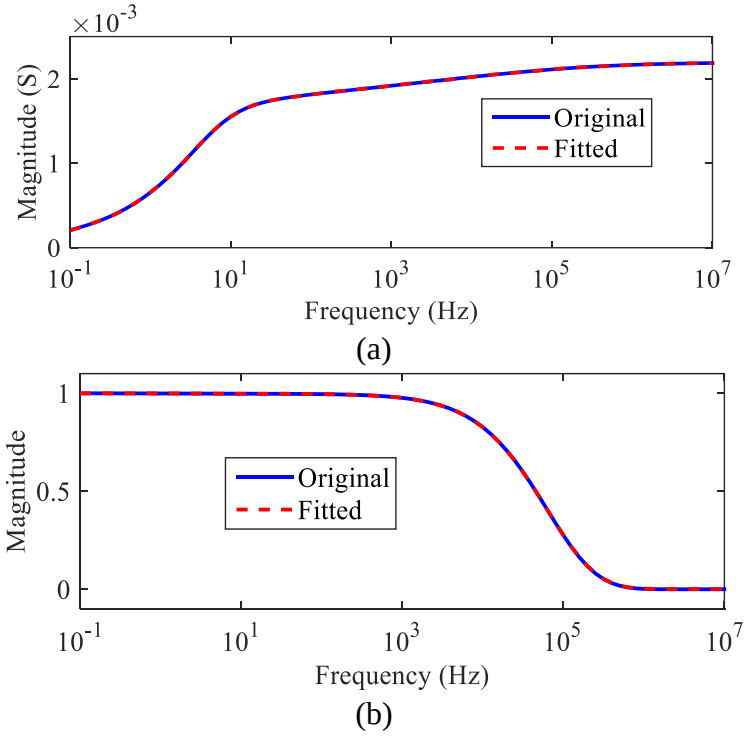

Figure 5.5. Magnitude plot by the proposed technique (LM-VF) for the transmission line case study, (a) characteristic admittance $\mathbf{Y}_c(s)$, (b) propagation function $\boldsymbol{\Gamma}(s)$.

To further demonstrate the efficiency of the proposed technique, Figure 5.6 shows the convergence of the pole relocation stage for the fitting of $\mathbf{Y}_c(s)$. The legends in Figure 5.6 indicate different possible types of initial poles using the stand-alone VF technique as follows: 1) real, linearly spaced (labeled VF 1), 2) real, logarithmically spaced (labeled VF 2), 3) complex, linearly spaced (labeled VF 3) and 4) complex, logarithmically spaced (labeled VF 4). This figure shows that, although in the first iteration the Hausdorff distance is very large by the proposed approach (LM-VF), it converges faster than the traditional VF method for any of the possible initial poles. Moreover, it should be noted that the model order is automatically determined by the proposed approach, whereas using the traditional VF, the user must guess the model order and the nature of the initial set of poles.

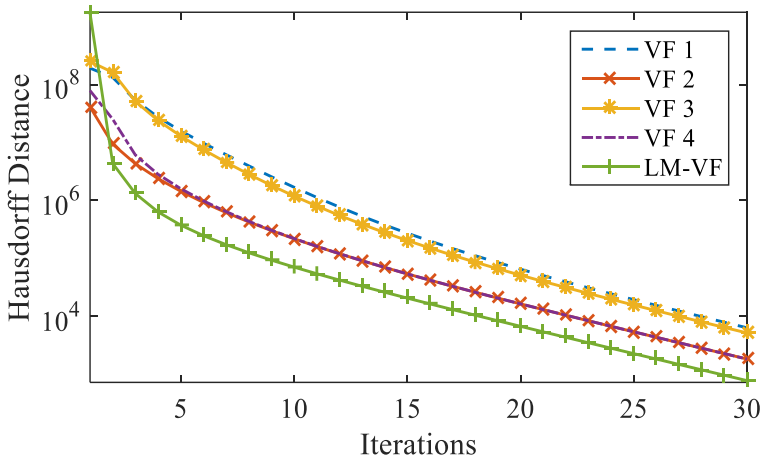

Figure 5.6. Comparison of the convergence of the pole relocation process by VF with different initial poles and the proposed approach (LM-VF), for the fitting of the characteristic admittance $\mathbf{Y}_c(s)$ of the transmission line case study.

5.5.2 Case study 2: distribution network

The performance of the proposed fitting approach is now evaluated using the distribution network of Figure 4.9. A comparison of the resulting RMS error by using the two possible combinations of the proposed fitting methodology (LM-VF and MPM-VF), against MPM and LM techniques for different values of ξ is shown in Table 5.4. From this table it is observed that the proposed methods LM-VF and MPM-VF achieve a more refined fitting accuracy than the stand-alone LM and MPM techniques, respectively, for all the values of ξ given.

Table 5.4. Evaluation of the proposed techniques (MPM-VF and LM-VF) against MPM and LM techniques applied to the distribution network case study of Figure 4.9.

Threshold value (ξ)	ε_{RMS}			
	LM	**LM-VF** (proposed)	**MPM**	**MPM-VF** (proposed)
1×10^{-2}	1.39×10^{-2}	3.16×10^{-4}	7.78×10^{-3}	2.11×10^{-3}
1×10^{-3}	1.78×10^{-3}	4.07×10^{-5}	2.61×10^{-3}	5.16×10^{-4}
1×10^{-4}	1.29×10^{-4}	6.44×10^{-8}	2.03×10^{-3}	4.60×10^{-5}
1×10^{-5}	1.01×10^{-5}	1.78×10^{-9}	1.84×10^{-3}	3.49×10^{-6}
1×10^{-6}	1.97×10^{-7}	1.61×10^{-9}	1.72×10^{-3}	8.10×10^{-8}

On the other hand, comparing the proposed technique against the stand-alone VF technique, the user should guess the model order and the nature of initial poles. Selecting for example logarithmically-spaced complex poles results in poor convergence of the VF technique as illustrated in Figure 5.7, where the convergence of the proposed approaches MPM-VF and LM-VF is noticeable faster.

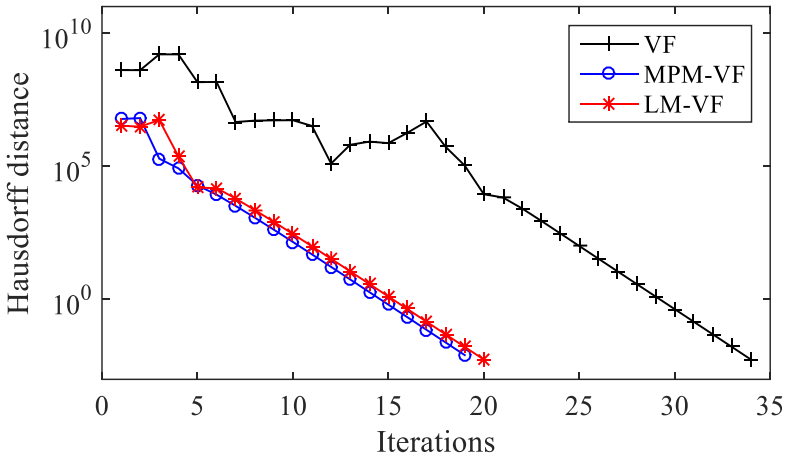

Figure 5.7. Comparison of the convergence of the pole relocation process by the proposed approach (MPM-VF and LM-VF) against VF.

5.5.3 Case study 3: 400-kV transmission network

The 400-kV transmission network of Figure 5.8 is used for the computation of an FDNE applying the proposed technique. The system of Figure 5.8 is constituted of 469 nodes, 58 overhead transmission lines represented by the Frequency Dependent (FD) model [25], 16 generation stations modeled as constant voltage sources behind RL impedances, 105 ideal transformer units and 280 linear RLC branches. The FDNE is calculated for the elements outside the enclosed region (study zone) in Figure 5.8.

The fitting of the measured 15×15 size admittance matrix of the external-zone is achieved using the parameter $\xi = 1\times10^{-5}$ for the proposed MPM-VF approach. The magnitudes of entries $\mathbf{Y}(1,1)$ and $\mathbf{Y}(1,2)$ of the measured admittance matrix are plotted in Figure 5.9 together with their fitted counterparts (only these two curves are shown for clarity). This figure demonstrates high fitting accuracy by the proposed technique.

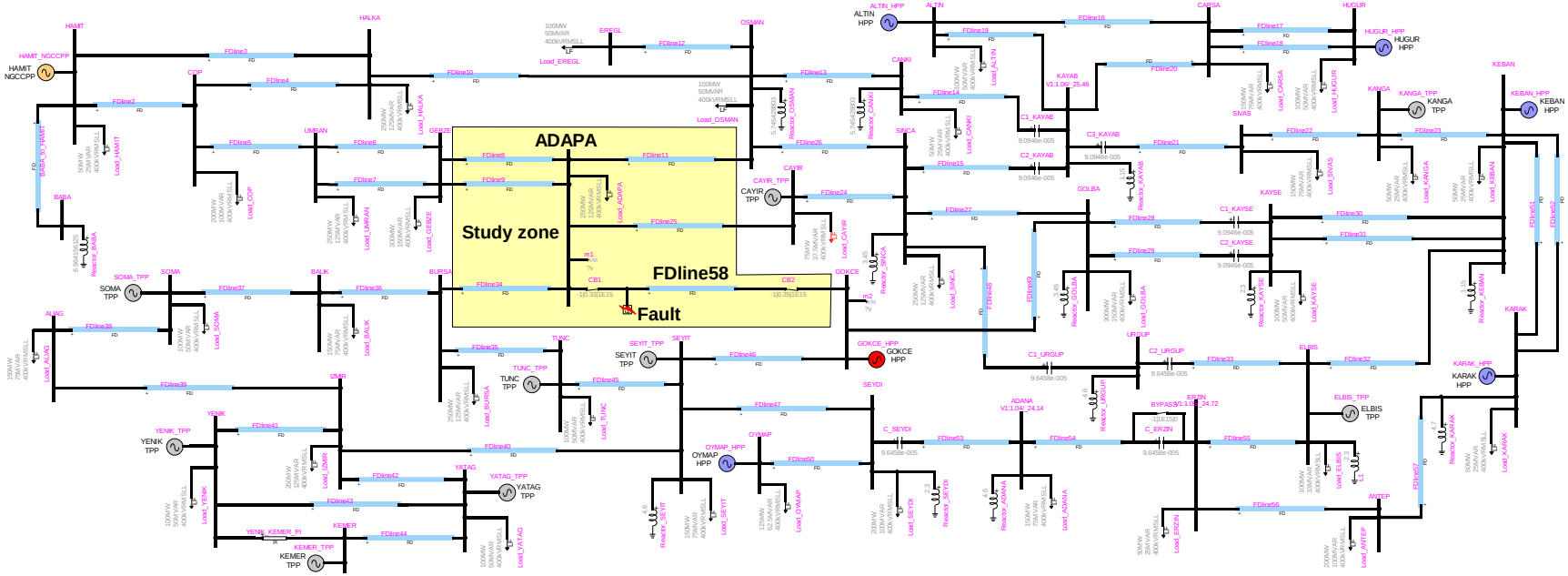

Figure 5.8. 400-kV Transmission network.

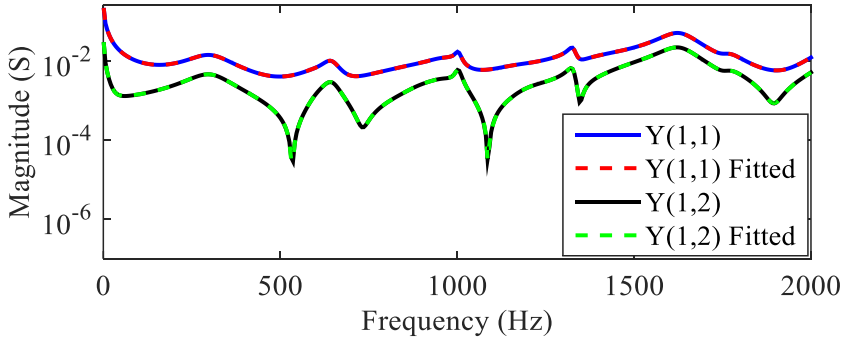

Figure 5.9. Magnitude of the admittance matrix entries $\mathbf{Y}(1,1)$ and $\mathbf{Y}(1,2)$ of the transmission network of Figure 5.8.

To further evaluate the proposed technique, the resulting model order and RMS error for different values of ξ are presented in Table 5.5. This table confirms that the resulting RMS error is about the same order of the selected threshold value ξ as discussed in section 5.3. Moreover, Table 5.5 declares if the rational model is passive or not, and it is observed that the rank of values for ξ to avoid passivity violations is between 1×10^{-4} and 1×10^{-5}. This rank of values is in agreement with the results obtained in section 5.3, for the fitting of the distribution network of Figure 4.9.

Table 5.5. Fitting accuracy by the proposed approach (MPM-VF) for the fitting of the transmission network system of Figure 5.8 with different values of ξ.

Threshold value (ξ)	**Model order** (N)	ε_{RMS}	**Model passivity**
1×10^{-2}	40	1.0×10^{-3}	No
1×10^{-3}	80	2.10×10^{-4}	No
1×10^{-4}	110	6.28×10^{-5}	**Yes**
5×10^{-5}	121	4.39×10^{-5}	**Yes**
1×10^{-5}	139	2.15×10^{-5}	**Yes**
1×10^{-6}	162	6.96×10^{-6}	No
1×10^{-7}	179	2.09×10^{-6}	No

Finally, the RMS error resulting by applying the proposed method and the VF technique individually are compared in Table 5.6 for different number of iterations applied in the pole relocation process. Although the differences are small, this table shows consistent results, i.e., the proposed MPM-VF approach achieves faster fitting accuracy of the pole relocation stage.

Table 5.6. Evaluation of the RMS error by the proposed MPM-VF technique and the VF method for the fitting of the admittance function of the transmission network of Figure 5.8.

Iterations	ε_{RMS}	
	VF	**MPM-VF**
1	3.82×10^{-4}	3.69×10^{-4}
2	1.56×10^{-4}	1.19×10^{-4}
3	1.31×10^{-4}	1.01×10^{-4}
4	1.20×10^{-4}	9.75×10^{-5}
5	1.14×10^{-4}	9.62×10^{-5}
10	9.77×10^{-5}	9.18×10^{-5}
20	9.05×10^{-5}	8.84×10^{-5}

5.6 Discussion

The proposed fitting technique (considering the two possible derivations: MPM-VF and LM-VF) constitute an improved version (or extended version) of the VF technique. The improvement consists of a novel (more efficient) initialization procedure of the pole relocation process by applying either the MPM or the LM technique. Using any of these two techniques, the most important issues of the traditional VF method are overcome, such as, model order identification and selection of initial poles. Furthermore, by applying any of the two possible combinations (MPM-VF or LM-VF), the model order identification step becomes automatic.

Alternatively, the proposed technique can be considered as an improved version of the MPM or the LM techniques, where the obtained poles are refined by applying the pole relocation process of the VF method, then, improving its accuracy.

5.7 Conclusions

In this chapter, a novel approach for the fitting of rational models has been proposed by incorporating the MPM or the LM method into the VF technique. The proposed approach is demonstrated to achieve a refined fitting accuracy than the stand-alone MPM and LM methods. Also, the proposed technique shows a faster convergence than the VF technique. A major feature of the proposed method is the automatic model order determination.

CHAPTER 6 A NEW PASSIVITY ENFORCEMENT TECHNIQUE

As it has been discussed in previous chapters, the passivity of rational models is crucial for the numerical stability of transient simulations. In Chapter 3, some methods for the passivity enforcement have been reviewed. In this chapter, first, some numerical examples are presented to unveil the limitations of the existing passivity enforcement methods; then, the causes of passivity violations are analyzed; finally, a new passivity enforcement method is presented and tested with numerical examples.

6.1 Limitations of traditional passivity enforcement techniques

The passivity enforcement techniques studied in Chapter 3, named Fast-Residue Perturbation (FRP), Hamiltonian Matrix Perturbation (HMP) and Semidefinite Programming (SDP), enforce the passivity of rational models by perturbing the state-space model matrix **C**, or equivalently, the residues of the rational model. Those methods rely on the solution of different optimization problems. In general, the objective function is set to minimize the deviation of the frequency-response of the rational model with respect to the original frequency-response, and the restrictions are set such that the passivity of the rational model is enforced. The problem addressed in this thesis is that when the model order or the number of ports of the rational model is substantial (or a combination of both), the computational burden required by the existing passivity enforced techniques becomes very high. Thus, the involved optimization problems require large CPU times, and sometimes, the existing techniques cannot find a solution due to the excessively large computational memory requirements.

To start analyzing the computational performance of the outlined passivity enforcement methods, the distribution network of Figure 4.9 is used one more time. For this test system, the number of ports is 6, and a rational model with order $N = 60$ is studied. By computing the singularity test matrix $\mathbf{S}$ as defined in (3.101) for the outlined rational model, passivity violations are revealed at the frequency intervals [0 - 2.11], [24.95 - 113.51] and [104×10^3 - 110×10^3] (Hz). Subsequently, passivity is enforced by applying the FRP, HMP and SDP techniques, the resulting CPU times and RMS errors are listed in Table 6.1. This table shows that the FRP technique achieves the lowest CPU time, whereas HMP achieves the lowest RMS error. On the other hand, the SDP method takes the largest CPU time and highest RMS error.

Table 6.1. Passivity enforcement by FRP, HMP and SDP methods for the FDNE of the distribution network case study with order $N = 60$.

Technique	**CPU (s)**	ε_{RMS}
FRP	41	3.31×10^{-5}
HMP	52	8.03×10^{-6}
SDP	3663	4.00×10^{-3}

A similar numerical experiment for the transmission network case study of Figure 5.8 is presented. In this case, the number of ports and the model order are 15 and $N = 100$, respectively. The resulting CPU times and RMS errors by the studied passivity enforcement techniques are listed in Table 6.2. This table shows that the CPU time is considerably larger than the previous example since a higher model order and higher number of ports in the rational model are involved. As for the SDP technique, passivity enforcement is unfeasible because of lack of computing memory.

Table 6.2. Passivity enforcement performances by FRP, HMP and SDP methods for a rational model with order $N = 100$ for the 400-kV transmission network case study of Figure 5.8.

Technique	**CPU (s)**	ε_{RMS}
FRP	1161	4.16×10^{-5}
HMP	81	4.99×10^{-5}
SDP	unfeasible	-

6.2 Causes of passivity violations

As studied in Chapter 5, one of the factors that may affect the passivity of rational models is the model order. That is, by selecting a very-low or very-high model order, the resulting model is more likely to present passivity violations. In the case of very-low model orders, this occurs because of poor fitting accuracy, such that the eigenvalues of the rational model cannot closely match those of the original frequency-response, and passivity violations may appear anywhere within the fitting band. On the other hand, for very-high model orders, passivity violations usually appear outside the fitting band. In this case, the reason is because poles with resonant frequency out of the fitting band usually appear in the rational model, and those poles produce an uncontrolled frequency-response out of the fitting band.

A special case of passivity violations in rational models occurs when the original frequency-response contains passivity violations. In this case, the fitted model will simply repeat this pattern since the eigenvalues of the conductance matrix of the fitted model will follow those of the original frequency-response. The reasons why a measured frequency-response might present a non-passive characteristic can be due to different factors, such as, error in the measurements or calculations, noise-contaminated frequency-responses, or simply because the device/network being modeled cannot be represented by a passive rational model. For this special case of passivity violations, the reader is referred to [70]. Additionally, an alternative and more detailed analysis about the causes of passivity violations can be found in [71].

Since this thesis aims at computing passive rational models for FDNEs, its focus is on cases where the frequency-response to fit is highly resonant. An example of this is the 400-kV transmission network Figure 5.8. For this example, the eigenvalues of the conductance matrix of the measured frequency-response and those of the fitted rational model (with order $N = 100$) are shown in Figure 6.1.

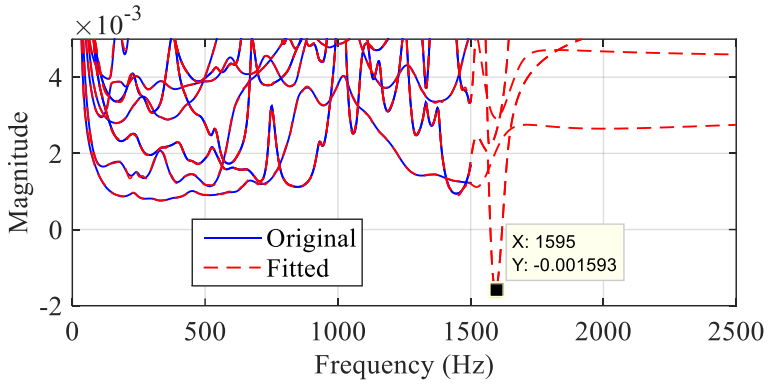

Figure 6.1. Eigenvalues of the conductance matrix of the original frequency-response and fitted rational model with $N = 100$ for the 400-kV transmission network example.

From Figure 6.1, it is observed that the rational model contains a single passivity violation which occurs out of the fitting frequency band (0.1 Hz to 1.5 kHz). Figure 6.1 also indicates the magnitude of the worst passivity violation point, -1.59×10^{-3}, and the corresponding frequency, 1595 Hz. For this rational model, the resonant frequencies of the three pair of complex poles (imaginary parts) with highest resonant frequencies are given in Table 6.3. This table reveals that the highest resonant frequency of the pair of poles 99-100 (1579.5 Hz) is very close to the frequency of the worst passivity violation point (1595 Hz).

Table 6.3. Complex-conjugate pair of poles with highest resonant frequencies for the rational model with $N = 100$ of the 400-kV transmission network.

Pair of poles (sort by resonant frequency)	**Resonant frequency**
95, 96	1476.2 Hz
97, 98	1505.5 Hz
99, 100	1579.5 Hz

Additionally, it is important to point out that the resonance frequency of the pair of poles 99-100 does not correspond to fitted frequency response since it is beyond the fitting band. Thus, the outlined pair of complex conjugate poles can be blamed for the identified passivity violation. As a preliminary hypothesis, it is believed that by appropriately perturbing the blamed pair of complex poles, passivity violations can be removed.

6.3 Pole-selective residue perturbation (PSRP) technique

To overcome the limitations of the existing passivity enforcement techniques, such as large computational burden and memory requirements, a new passivity enforcement technique is proposed in this thesis. The proposed methodology has the following two main characteristics: 1. unlike the existing passivity enforcement methods, it is not based on the solution of any optimization problem; 2. the correction applied to the rational model only affects specific residue matrices of the model. These two main features of the proposed passivity enforcement technique permit high computational efficiency compared to the existing methods. Moreover, the proposed method does not present restrictions regarding the model order and number of ports.

In the proposed technique, the residue matrices to be perturbed are selected according to the resonant frequencies of the poles of the rational model and the frequencies of worst passivity violations. As it will be demonstrated next, this simplistic but effective method, in most cases, enforces the passivity of rational models with very slight deviations of the initial fitting error and at very low computational cost.

6.3.1 Dominant poles

To identify the residue matrices of the rational model to be perturbed, the proposed approach first requires the identification of the pair of complex conjugate poles whose resonant frequency is the

closest to the worst passivity violation. These poles are called in this thesis *dominant poles*. Note that this identification process has already been achieved for the example analyzed in section 6.2, for the rational model of the transmission network of Figure 5.8 with order $N = 100$. Using the same 15-port example, the complete set of eigenvalues of the conductance matrix evaluated at the worst passivity violation frequency identified (1595 Hz) are

$$\begin{aligned}\boldsymbol{\Lambda} = [&0.0552 \quad 0.0552 \quad 0.0413 \quad 0.0413 \quad 0.0164 \quad 0.0085 \quad 0.0054 \quad 0.0120 \quad \cdots \\ &0.0120 \quad 0.0020 \quad 0.0029 \quad -0.0016 \quad -0.0016 \quad 0.0025 \quad 0.0025]^{\prime},\end{aligned} \tag{6.1}$$

As it can be observed in (6.1), two identical eigenvalues violate passivity, those are: $\lambda_{12} = \lambda_{13} = -1.6 \times 10^{-3}$. From (6.1), it can inferred that the required perturbation for the eigenvalues of the rational model to remove passivity violations at the studied frequency is

$$\begin{aligned}\Delta\boldsymbol{\Lambda} = [&0 \quad 0 \quad 0 \quad 0 \quad 0 \quad 0 \quad 0 \quad 0 \quad \cdots \\ &0 \quad 0 \quad 0 \quad 0.0016 \quad 0.0016 \quad 0 \quad 0]^{\prime},\end{aligned} \tag{6.2}$$

such that the eigenvalues of the perturbed model

$$\boldsymbol{\Lambda}_{perturbed} = \boldsymbol{\Lambda} + \Delta\boldsymbol{\Lambda}, \tag{6.3}$$

become all nonnegative (at the frequency point studied). Usually, by enforcing the negative eigenvalues to be nonnegative at the point or worst passivity violations, these eigenvalues are also moved at surrounding frequencies, eliminating passivity violations entirely.

As it has been discussed in Chapter 3, the increment for the eigenvalues of the conductance matrix of the rational model can be obtained by perturbing any of its parameters. However, the perturbation of the residue matrices is preferred to avoid changing the model dynamics. Then, for the example under study, it is concluded that the goal is to find the residue matrix perturbations $\Delta\mathbf{R}_{99}$ and $\Delta\mathbf{R}_{100}$ (residue matrices associated to the dominant poles) such that the required increment in the eigenvalues, as given by (6.2) is produced.

6.3.2 Residue perturbations by the PSRP method

For a generic passivity violation, let us consider that the worst passivity violation occurs at frequency $s_k = j\omega_k$; the dominant poles are p and its complex conjugate p^*; and the related residue matrices are $\mathbf{R}$ and $\mathbf{R}^*$. Once the dominant poles have been identified, the PSRP method

consists of approximating the fitted model frequency-response (admittance matrix in this thesis) evaluated at the worst passivity violation frequency, by considering only the dominant poles and associated residue matrices, i.e.,

$$\mathbf{Y}(s_k) \approx \frac{\mathbf{R}}{s_k - p} + \frac{\mathbf{R}^*}{s_k - p^*}. \tag{6.4}$$

Considering the approximation given in (6.4), the eigenvalues of the conductance matrix become

$$\mathbf{\Lambda}_k \simeq \mathbf{T}^{-1}\Re\left\{\frac{\mathbf{R}}{s_k - p} + \frac{\mathbf{R}^*}{s_k - p^*}\right\}\mathbf{T}, \tag{6.5}$$

where $\mathbf{T}$ is a matrix containing the right-eigenvectors of the real part of $\mathbf{Y}(s_k)$ in (6.4) (conductance matrix).

Then, applying linearization to (6.5) one obtains

$$\Delta\mathbf{\Lambda}_k \simeq \mathbf{T}^{-1}\Re\left\{\frac{\Delta\mathbf{R}}{s_k - p} + \frac{\Delta\mathbf{R}^*}{s_k - p^*}\right\}\mathbf{T}. \tag{6.6}$$

Considering that the dominant poles and the required increment $\Delta\mathbf{\Lambda}_k$ have been identified, as for the example of previous section, from (6.6), the searched $\Delta\mathbf{R}$ can be isolated as follows.

First, (6.6) is rewritten as

$$\Delta\mathbf{G}(s_k) = \Re\left\{\frac{\Delta\mathbf{R}}{s_k - p} + \frac{\Delta\mathbf{R}^*}{s_k - p^*}\right\}, \tag{6.7}$$

where

$$\Delta\mathbf{G}(s_k) = \mathbf{T}\Delta\mathbf{\Lambda}_k\mathbf{T}^{-1}. \tag{6.8}$$

From (6.7), note that only the real part is required at the right side of the equal. However, without loss of generality, (6.7) can be expressed as

$$\Delta\mathbf{Y}(s_k) = \Delta\mathbf{G}(s_k) + j\Delta\mathbf{\beta}(s_k) = \frac{\Delta\mathbf{R}}{s_k - p} + \frac{\Delta\mathbf{R}^*}{s_k - p^*}, \tag{6.9}$$

where $\Delta\boldsymbol{\beta}$ denotes the susceptance matrix, which, according to the procedure presented is a zero matrix, since only $\Delta\mathbf{G}(s_k)$ is given in (6.8).

Then, using (6.9), the (i, j) matrix entries can be identified as

$$\Delta y_{ij} = \frac{\Delta r_{ij}}{s_k - p} + \frac{\Delta r_{ij}^*}{s_k - p^*}. \tag{6.10}$$

Considering that the dominant poles and corresponding residue matrices are complex values, denoted by

$$\Delta r_{ij} = \Delta a_{ij} + j\Delta b_{ij} \tag{6.11}$$

$$p = \alpha + j\beta, \tag{6.12}$$

equation (6.10) can be expanded to

$$\Delta y_{ij} = \frac{\Delta a_{ij} + j\Delta b_{ij}}{j\omega_k - (\alpha + j\beta)} + \frac{\Delta a_{ij} - j\Delta b_{ij}}{j\omega_k - (\alpha - j\beta)}. \tag{6.13}$$

After some algebraic manipulations to (6.13), the searched solution for the real and imaginary parts of the residue matrices can be obtained as

$$\Delta a_{ij} = -\Delta y_{ij}\alpha, \tag{6.14}$$

$$\Delta b_{ij} = \frac{\Delta y_{ij}\left(\alpha^2 + \omega_k^2 - \beta^2\right)}{2\beta}. \tag{6.15}$$

Solving (6.14) and (6.15) for every (i, j) entry, the searched residue matrix perturbation $\Delta\mathbf{R}$, and as consequence $\Delta\mathbf{R}^*$ are obtained.

6.3.3 Numerical considerations by the PSRP method

Recalling the numerical example illustrated in Figure 6.1, for which the worst passivity violation, dominant poles, and the required increment $\Delta\boldsymbol{\Lambda}_k$ (as given in (6.2)) have been identified in section 6.3.1, the methodology presented in previous section is applied to compute the searched residue matrices perturbations $\Delta\mathbf{R}_{99}$ and $\Delta\mathbf{R}_{100}$.

First, $\Delta\mathbf{G}(s_k)$ is calculated as indicated in (6.8), subsequently, the entries of $\Delta\mathbf{R}_{99}$ and $\Delta\mathbf{R}_{100}$ as are computed according to (6.14) and (6.15). Finally, the obtained matrix perturbations are applied to the original residue matrices as

$$\begin{aligned}\mathbf{R}_{99,new} &= \mathbf{R}_{99} + \Delta\mathbf{R}_{99} \\ \mathbf{R}_{100,new} &= \mathbf{R}_{100} + \Delta\mathbf{R}_{100}\end{aligned}. \tag{6.16}$$

Then, using the perturbed rational model, the eigenvalues at the frequency of study (worst passivity violation) are calculated again, the resulting new eigenvalues are

$$\begin{aligned}\mathbf{\Lambda} = [&0.0552 \quad 0.0552 \quad 0.0413 \quad 0.0413 \quad 0.0164 \quad 0.0085 \quad 0.0054 \quad 0.0120 \quad \cdots \\ &0.0120 \quad 0.0020 \quad 0.0029 \quad -2\times10^{-7} \quad -2\times10^{-7} \quad 0.0025 \quad 0.0025]\end{aligned}. \tag{6.17}$$

As it can be observed in (6.17), the eigenvalues that were initially of magnitude -1.6×10^{-3} have become four orders of magnitude smaller (-2×10^{-7}); however, the objective of enforcing passivity has not been accomplished, since the two eigenvalues are still negative. The reason why the eigenvalues in (6.17) are still negative is because the proposed methodology is based on an approximation, as given in (6.4), which is strictly not correct. Moreover, the obtained perturbation is based on the increment given in (6.2), which ideally, would make the negative eigenvalues equal to zero. Considering these factors, a modification to (6.8) is suggested as

$$\Delta\mathbf{G}(s_k) = \mathbf{T}(1.05)\Delta\mathbf{\Lambda}_k\mathbf{T}^{-1}. \tag{6.18}$$

By using (6.18), the negative eigenvalues are forced not only to approach the zero value, but to take small positive values to effectively remove passivity violations. The factor 1.05 in (6.18) indicates that the magnitude of the perturbation as given in (6.2) is being increased by 5%. This magnitude increase does not modify the direction towards the eigenvalues are being displaced (given by the corresponding eigenvectors).

The perturbation for the passivity enforcement of the example of Figure 6.1 is achieved again, but using (6.18) instead of (6.8). This time, the eigenvalues of the perturbed model are

$$\begin{aligned}\mathbf{\Lambda} = [&0.0552 \quad 0.0552 \quad 0.0413 \quad 0.0413 \quad 0.0164 \quad 0.0085 \quad 0.0054 \quad 0.0120 \quad \cdots \\ &0.0120 \quad 0.0020 \quad 0.0029 \quad 8\times10^{-5} \quad 8\times10^{-5} \quad 0.0025 \quad 0.0025]\end{aligned}. \tag{6.19}$$

From (6.19), it is observed that the originally negative eigenvalues have been successfully displaced to positive values, proving the effectiveness of (6.18). Moreover, it is interesting to analyze the impact of the applied perturbation on the eigenvalues over the entire frequency fitting band including boundaries. To do so, the eigenvalues of the initially fitted (non-passive) and perturbed model are shown in Figure 6.2. This figure reveals that the perturbation applied by the PSRP technique has a trivial impact on the eigenvalues far from the violation frequency and passivity violations are effectively removed.

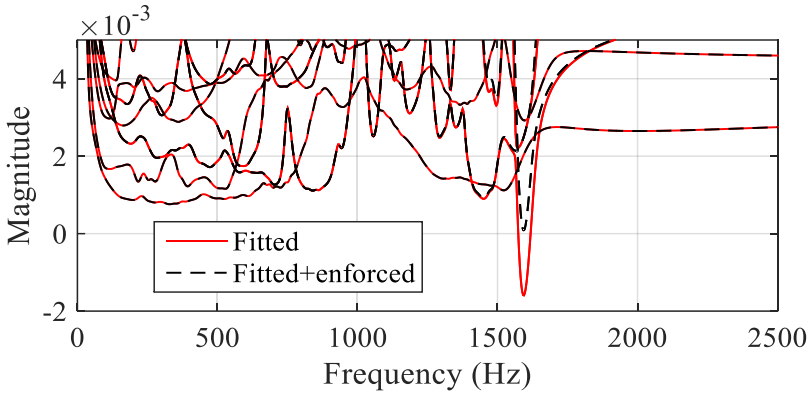

Figure 6.2. Eigenvalues of the initially fitted (non-passive) and perturbed (passive) model for the 400-kV transmission network with $N = 100$.

6.3.3.1 Low-frequency passivity violations

In some cases, passivity violations can appear at very low frequencies, where none of the pairs of complex poles has a resonant frequency nearby. In this case, the dominant pole can be set as a real pole of the rational model. Since real poles almost behave as decaying exponential functions in the frequency-domain, the perturbation of any real pole of the rational model can substantially modify the eigenvalues of $\mathbf{G}(s)$ at low frequencies for passivity enforcement.

In the case of perturbing the residue matrices related to a real pole, the corresponding approximation, analogous to (6.4), is

$$\mathbf{Y}(s_k) \approx \frac{\mathbf{R}}{s_k - p}. \tag{6.20}$$

Considering that passivity of the rational model is given by the real part of $\mathbf{Y}(s_k)$ and linearizing (6.20) one obtains

$$\Delta\mathbf{G}\left(s_k\right) = \Re\left\{\frac{\Delta\mathbf{R}}{s_k - p}\right\}. \tag{6.21}$$

Solving (6.21) for the increment of the residue matrix results in

$$\Delta\mathbf{R} = -\Delta\mathbf{G}\left(\omega_k^2 + p^2\right)\Big/ p\,. \tag{6.22}$$

Note that $\Delta\mathbf{G}$ in (6.22) must be calculated as indicated in (6.18).

6.3.4 Iterative scheme by the PSRP method

Since rational models may result with multiple passivity violations, multiple perturbations may be required for effectively removing all passivity violations. An example of multiple passivity violations is illustrated in Figure 6.3, where two violation frequency intervals are represented, and for each violation interval, two eigenvalues are observed to take negative values. In the PSRP technique each of them, requires a perturbation. Additionally, Figure 6.3 illustrates the selection of dominant poles according to worst passivity violations for each negative eigenvalue.

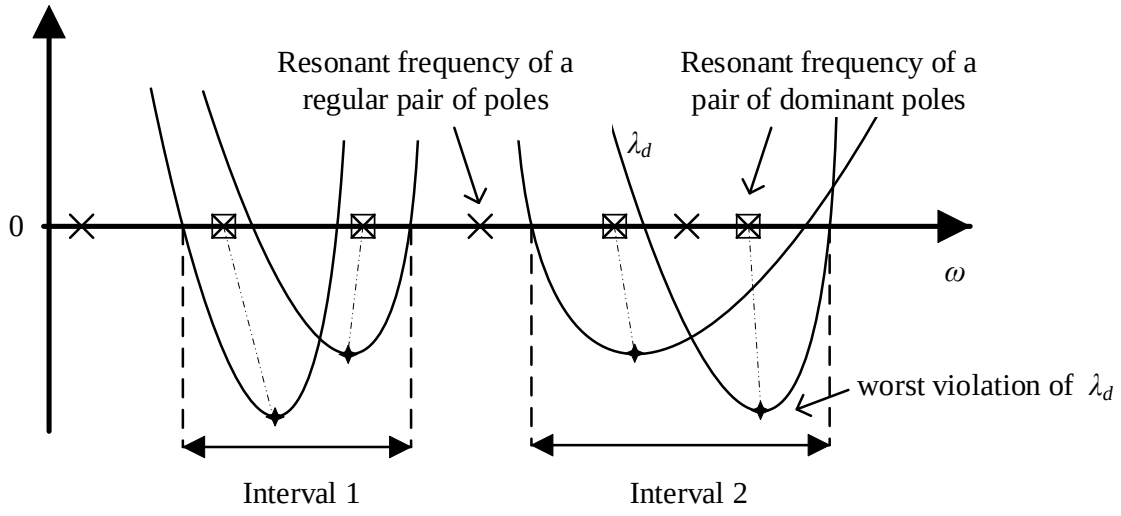

Figure 6.3. Illustration of multiple passivity violation intervals.

To deal with the passivity enforcement of rational models with multiple passivity violations, an iterative scheme is proposed for the PSRP technique as shown in Figure 6.4. This figure shows that after the application of a perturbation, or a set of them, a new passivity assessment is required, and if passivity violations persist, a new iteration of perturbations must be applied. The proposed iterative scheme is tested in the following section with numerical examples.

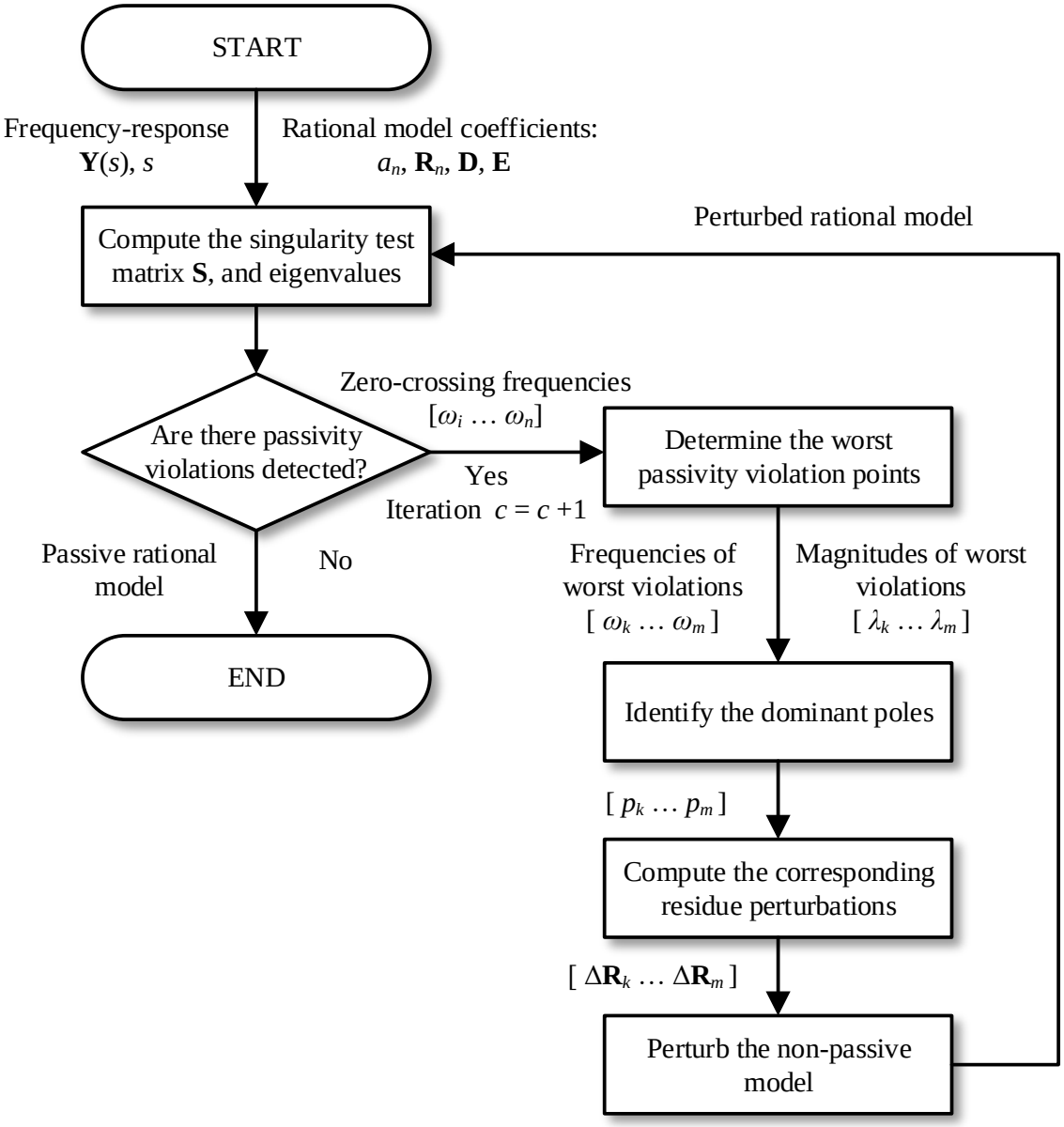

Figure 6.4. Iterative scheme proposed for the PSRP technique.

6.4 Evaluation of the PSRP method

6.4.1 Case study 1: 400-kV transmission network

To start with the evaluation of the proposed technique, the 400-kV transmission network of Figure 5.8 is used again. As it was demonstrated in section 6.3.3, Figure 6.2, the passivity of the 100-order rational model obtained for this case study is effectively enforced by the PSRP technique with a single perturbation. In this section, the computational performances and the fitting deviation by the PSRP method are compared with FRP, and HMP techniques for different model orders, as given in Table 6.4. Note that the results by SDP technique are not included since it fails due to multiple ports/large order, requiring large computational resources. The same occurs for the 150-order FDNE with FRP method.

Table 6.4. Comparison of the efficiency and fitting deviation by the PSRP, FRP, and HMP techniques, for different model orders for the 400-kV transmission network FDNE.

N	ε_{RMS}	**FRP**		**HMP**		**PSRP**	
		CPU (s)	ε_{RMS}	**CPU (s)**	ε_{RMS}	**CPU (s)**	ε_{RMS}
90	4.83×10^{-5}	366	5.52×10^{-5}	89	1.04×10^{-4}	1.5	5.51×10^{-5}
95	4.05×10^{-5}	377	4.06×10^{-5}	94	5.23×10^{-5}	1.5	4.06×10^{-5}
100	3.71×10^{-5}	429	5.61×10^{-5}	107	3.84×10^{-5}	1.8	5.59×10^{-5}
105	3.23×10^{-5}	468	5.54×10^{-5}	119	6.11×10^{-5}	1.8	1.25×10^{-4}
150	4.35×10^{-6}	unfeasible	–	455	1.60×10^{-5}	5.5	1.80×10^{-4}

From the RMS errors shown in Table 6.4, it is observed that the three passivity enforcement methods achieve a similar (very slight) deviation of the fitting accuracy respect to the initial-fitting RMS error (as given in the second column). However, it is clearly seen that the proposed PSRP method is computationally more efficient compared to the FRP and HMP techniques, about 60 and 250 times faster than the HMP and FRP methods, respectively.

As for the 100-order model, Figure 6.5 and Figure 6.6 show the magnitude of the original and fitted admittances before and after passivity enforcement via PSRP method, respectively. Figure 6.6 reveals that by applying the PSRP technique, the fitting error is slightly increased near the maximum frequency of the fitted band (see the dashed-line square in Figure 6.6). This increment in the fitting error is observed around the frequency of the selected (dominant) poles. This deviation is, however, negligible to the overall fitting accuracy.

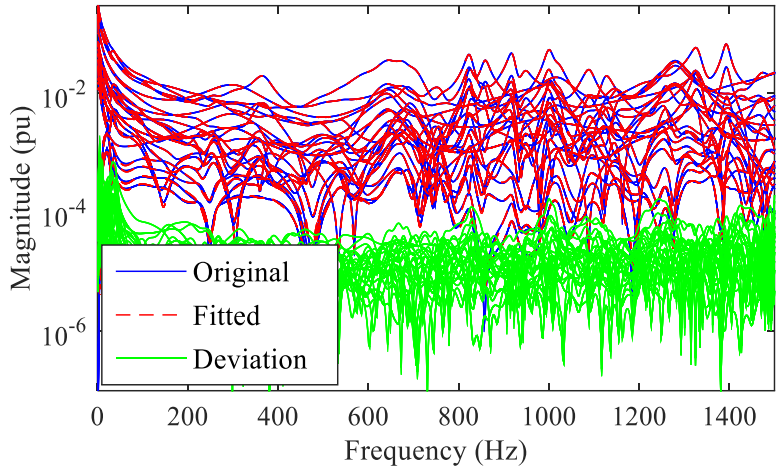

Figure 6.5. Admittance matrix elements of the external zone of the 400-kV transmission system of Figure 5.8 together with their fitted counterparts.

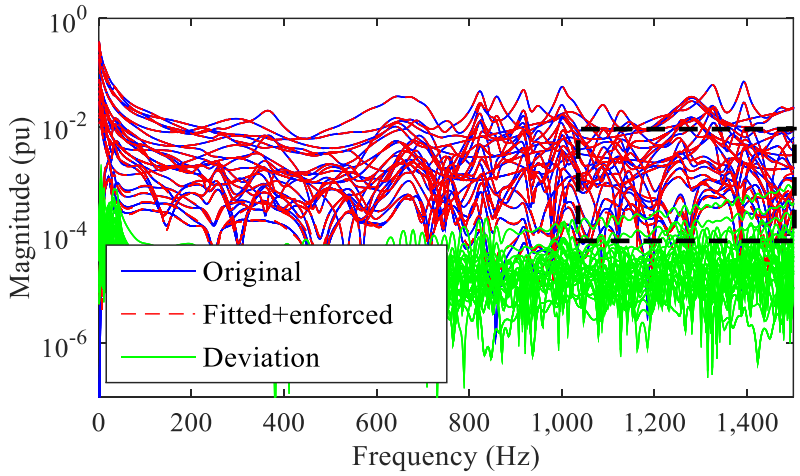

Figure 6.6. Admittance matrix elements of the external zone of the 400-kV transmission system of Figure 5.8 after passivity enforcement by the PSRP method.

Now, the passivity enforcement for the FDNE with fitting order is analyzed. The conductance matrix eigenvalues before and after applying the PSRP method are shown in Figure 6.7. This case shows that the PSRP method is still well suited for more severe passivity violations, in terms of both, magnitude and quantity. For this case, the PSRP applies perturbations on six eigenvalues and two iterations are required. Table 6.4 shows that although the computational effort by the PSRP method is increased for this case, the PSRP technique is still far more efficient (80 times faster) than the HMP technique, whereas the SDP and FRP techniques cannot achieved a solution due to the high computational burden.

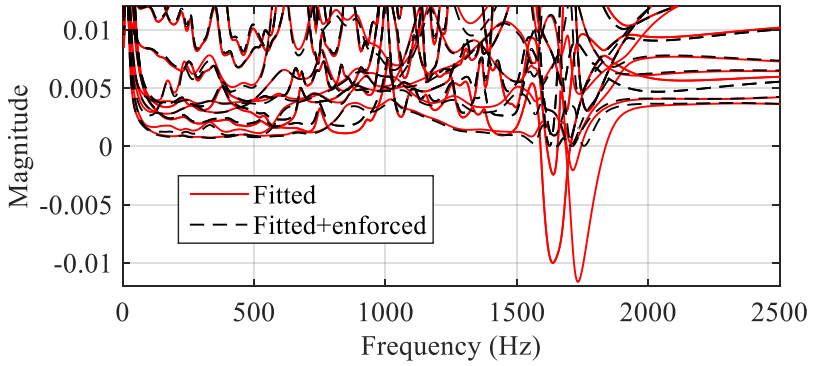

Figure 6.7. Eigenvalues of the conductance matrix for the fitting of the 400-kV transmission system of Figure 5.8 with $N = 150$ before and after passivity enforcement by PSRP.

To complement this case study, the 100-order FDNE, with passivity enforced via the PSRP method, is evaluated in transient simulation and compared with the original system. In TD- simulation, the network of Figure 5.8 is initialized at steady-state from load-flow solution. Then, at simulation time t = 0.25 s, a fault is applied at one end of the transmission line FDline58. The fault is cleared by disconnecting the affected transmission line at t = 0.33 s and t = 0.35 s at its left and right terminations, respectively. The simulation time-step used is 10 µs. The voltages generated at bus ADAPA from the instant the fault is cleared are shown in Figure 6.8. A zoom of the plot of Figure 6.8 is given in Figure 6.9 to better observe the differences in the waveforms. Transient simulation results confirm that the PSRP technique does not affect the fitted FDNE model, since the results are in excellent agreement with those of detailed modeling.

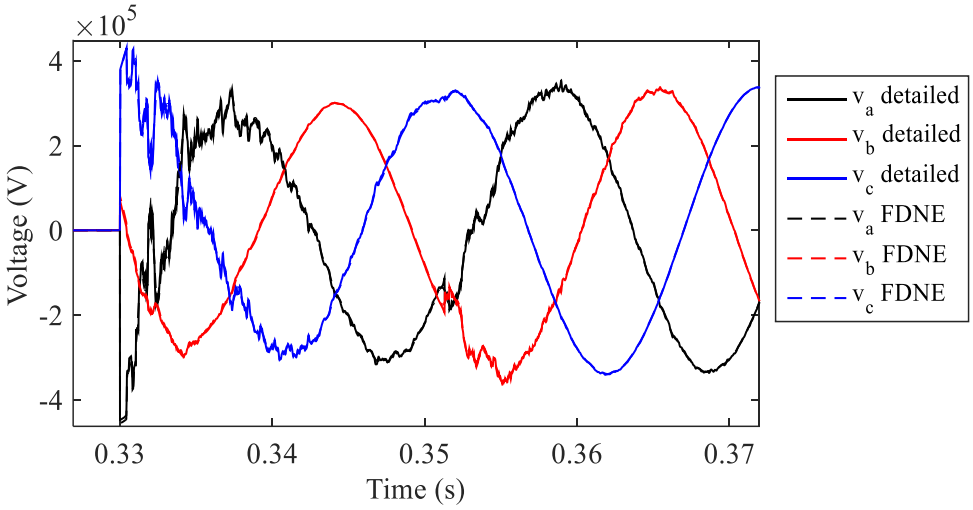

Figure 6.8. Time-domain simulation with passive 100-order FDNE model of 400-kV transmission system; voltages at ADAPA bus.

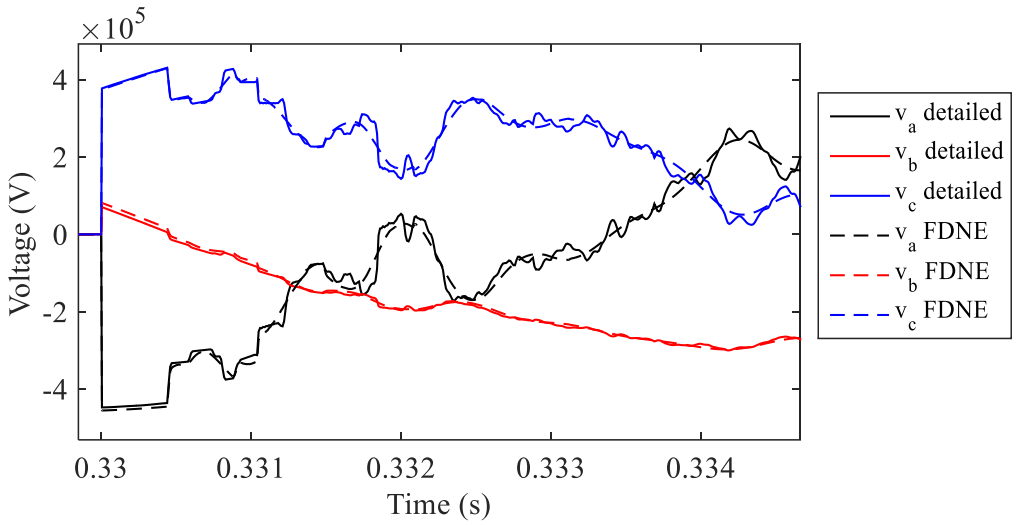

Figure 6.9. Zoom of Figure 6.8.

6.4.2 Case study 2: IEEE 39-bus benchmark

A new case study, the IEEE 39-bus benchmark system shown in Figure 6.10, is now used to evaluate the performance of the PSRP passivity enforcement technique for FDNEs. The system is constituted of 364 nodes, 24 CP-model transmission lines, 90 ideal transformer units, 205 RLC branches, and 10 generation stations modeled as constant sources behind impedances.

The admittance matrix of the external zone of the network of Figure 6.10 is measured and fitted from 1 Hz to 5 kHz with a rate sampling of 10 Hz to generate a 9-ports FDNE. The model orders $N = 90$ and $N = 100$ are used, for which the resulting FDNE models result non-passive. Then, the SDP, FRP, HMP and PSRP techniques are applied for passivity enforcement.

The resulting CPU-times and fitting errors by the outlined passivity enforcement methods are listed in Table 6.5. By comparing the initial RMS fitting error, as shown in the second column of Table 6.5, with the RMS error after passivity enforcement, it can be seen that all the studied techniques do not markedly affect the fitting accuracy by enforcing passivity, however, by comparing the CPU times, it can be observed that the PSRP method is, one more time, computationally far more efficient than the traditional methods.

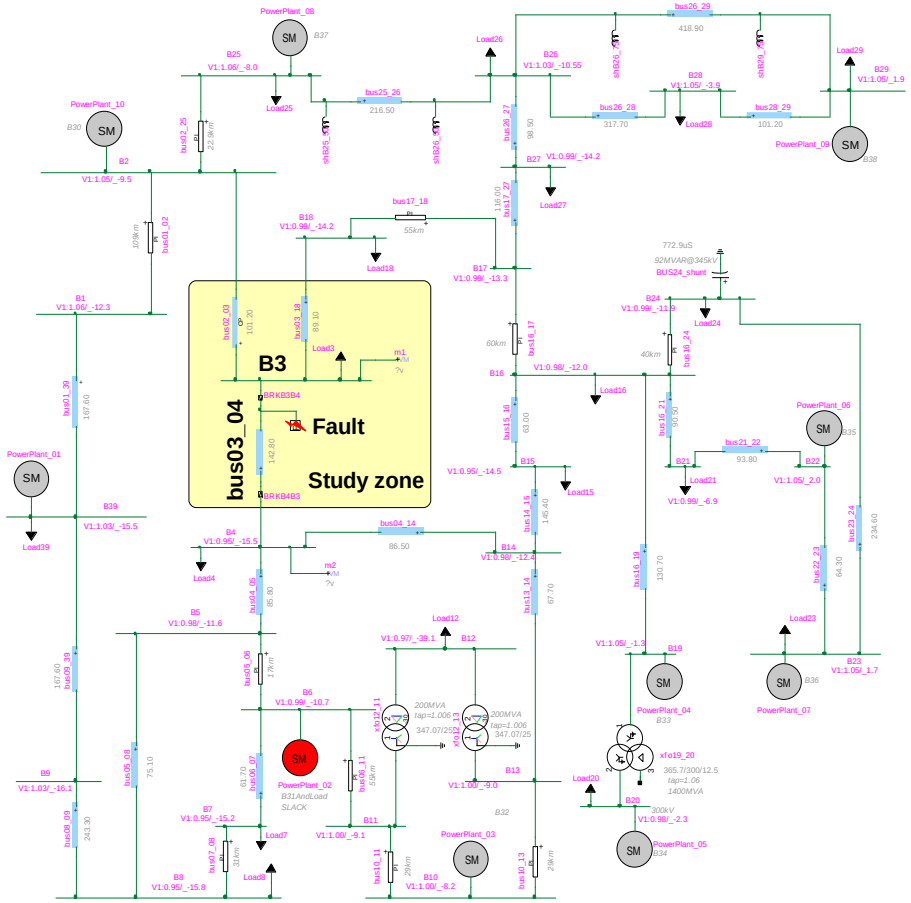

Figure 6.10. IEEE 39-Bus benchmark.

Table 6.5. Comparison of the passivity enforcement techniques for different model orders for the IEEE 39-Bus benchmark case study.

N	ε_{RMS}	SDP		FRP		HMP		PSRP	
		CPU (s)	ε_{RMS}	**CPU (s)**	ε_{RMS}	**CPU (s)**	ε_{RMS}	**CPU (s)**	ε_{RMS}
90	1.98×10^{-4}	147864	3.87×10^{-3}	108	2.27×10^{-4}	101	1.98×10^{-4}	12	2.08×10^{-4}
100	1.65×10^{-4}	152648	2.25×10^{-3}	119	1.97×10^{-4}	112	1.65×10^{-4}	5	1.71×10^{-4}

The conductance matrix eigenvalues for the 90- and 100-order FDNEs before and after passivity enforcement by the PSRP method are shown in Figure 6.11 and Figure 6.12, which are reached after 16 and 5 iterations, respectively. These figures show that, although both in-band and out-of-band passivity violations occur, the proposed PSRP technique effectively enforces passivity. Moreover, it is confirmed that the PSRP technique can correct the negative eigenvalues without substantially affecting the overall fitting accuracy.

The identified frequencies of worst passivity violations and resonant frequencies of dominant poles for the passivity enforcement of the 100-order FDNE model are given in Table 6.6 (for the first iteration of the PSRP technique). This table illustrates how the worst passivity violations and dominant poles closely coincide, which permits the successful application of the PSRP method.

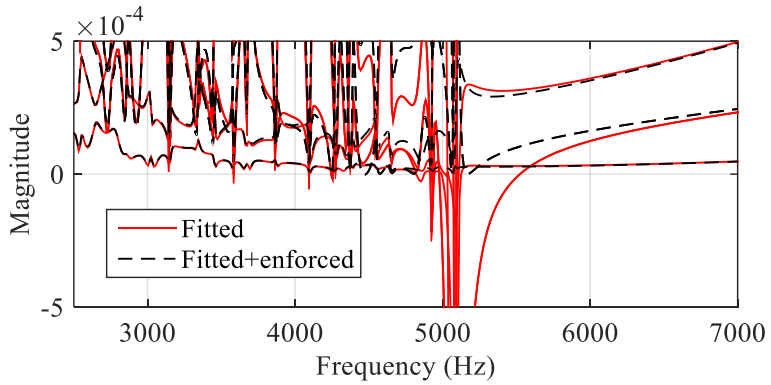

Figure 6.11. Eigenvalues of the conductance matrix for the FDNE of the IEEE 39-Bus benchmark with order $N = 90$ before and after passivity enforcement by PSRP.

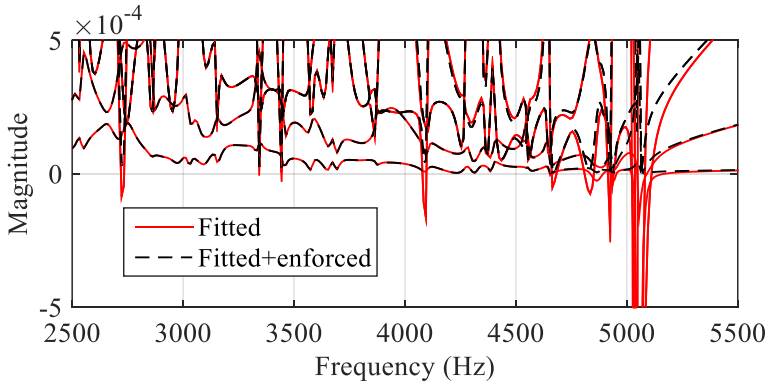

Figure 6.12. Eigenvalues of the conductance matrix for the FDNE of the IEEE 39-Bus benchmark with order $N = 100$ before and after passivity enforcement by PSRP.

Table 6.6. Dominant poles for the passivity enforcement by the PSRP method for the 100-poles FDNE for the IEEE 39-Bus benchmark case study.

Maximum passivity violation	**Frequency of maximum violation (Hz)**	**Resonant frequency of dominant poles (Hz)**
-1.12×10^{-4}	2726	2728
-1.95×10^{-4}	4049	4099
-6.58×10^{-6}	4655	4646
-2.63×10^{-5}	4863	4855
-2.20×10^{-4}	4925	4933
-6.05×10^{-3}	5047	5053
-5.75×10^{-3}	5053	5053

To complement this case study, the 100-poles FDNE model with passivity enforced by the PSRP technique is tested in transient simulation. The TD-simulation of the network of Figure 6.10 is initialized at steady-state. Then, a temporary three-phase fault is applied at time t = 0.2 s at one side of the transmission line bus03_04. The faulty transmission line is disconnected at t = 0.3 s at both ends. The transient voltages resulted at bus **B3** are shown in Figure 6.13, and a zoom of this plot is given in Figure 6.14 for a better appreciation of the waveforms obtained by the FDNE and detailed models. These figures show that the FDNE model achieves very accurate transient simulations compared to the detailed model.

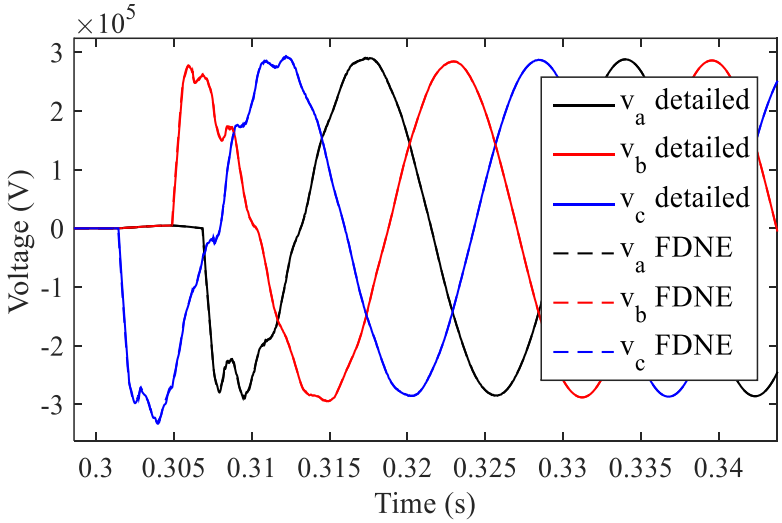

Figure 6.13. Transient voltages at bus **B3** of the network of Figure 6.10.

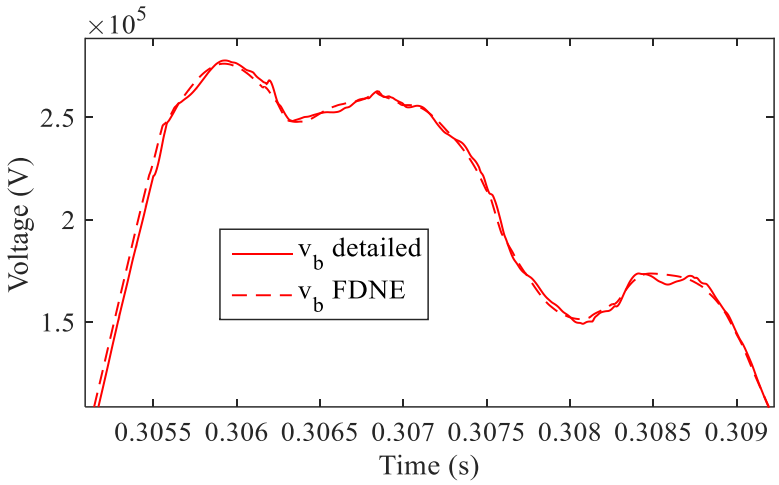

Figure 6.14. Zoom of the plot of Figure 6.13, phase *b* of the transient voltage at bus **B3**.

6.4.3 Case study 3: cross-bonded cable system

To further assess the performance of the proposed PSRP technique, the passivity enforcement of different FDNEs for the 225kV cross-bonded cable system of Figure 1.4, is studied. Note that a more detailed description of the system is given in Chapter 4, section 4.6. For this chapter, the outlined cable system is fitted for different frequency bands, such that different FDNEs model orders are obtained and tested. The resulting FDNE models result non-passive, then, these models are enforced applying the SDP, FRP, HMP and PSRP techniques.

The resulting CPU times and fitting accuracy deviations by the studied techniques are listed in Table 6.7. This table shows, one more time, a considerable superior computational performance of the PSRP method compared to the traditional techniques. Table 6.7 also reveals that both SDP and HMP techniques considerably corrupt the FDNEs fitting accuracy since the RMS errors are substantially increased compared to the initial fitting errors. On the other hand, the RMS errors resulting of the passivity enforcement by the FRP and PSRP technique are considerably lower.

The eigenvalues of the conductance matrix of the 50-order FDNE, before and after passivity enforcement, are shown in Figure 6.15. This figure shows that passivity violations mainly occur outside the fitting band; nonetheless, also low-frequency passivity violations are resulted, as it is better revealed in Figure 6.16. These figures show the effectiveness of the proposed PSRP method to enforce passivity without considerably affecting the overall fitting accuracy.

Table 6.7. Comparison of the passivity enforcement techniques for different fitting bands for the cross-bonded cable case study.

Fitting band (Hz)	N	ε_{RMS}	**SDP**		**FRP**		**HMP**		**PSRP**	
			CPU (s)	ε_{RMS}	**CPU** (s)	ε_{RMS}	**CPU** (s)	ε_{RMS}	**CPU** (s)	ε_{RMS}
$0.1 - 5\times10^3$	50	1.97×10^{-5}	2947	2.98×10^{-2}	20	1.40×10^{-4}	8	1.50×10^{-2}	0.7	1.70×10^{-4}
$0.1 - 10\times10^3$	100	8.16×10^{-6}	34430	3.07×10^{-2}	75	5.13×10^{-3}	22	5.00×10^{-3}	4	3.04×10^{-4}
$0.1 - 15\times10^3$	150	8.94×10^{-6}	139350	4.26×10^{-2}	70	7.11×10^{-4}	55	1.50×10^{-3}	3	3.65×10^{-4}

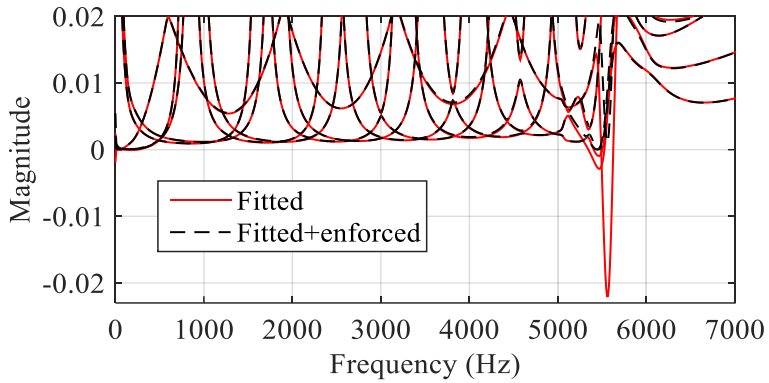

Figure 6.15. Eigenvalues of the conductance matrix of the cross-bonded cable system FDNE model with $N = 50$ before and after passivity enforcement by PSRP.

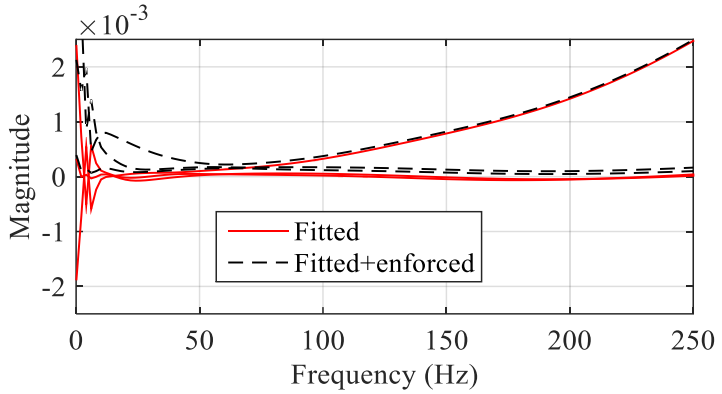

Figure 6.16. Zoom to the plot of Figure 6.15.

The accuracy of the 50-order FDNE with passivity enforced by the PSRP method is finally evaluated in time-domain simulation. The cross-bonded cable system of Figure 1.4 is energized at 4.5 ms. The resulting transient voltage measured at phase *a* of Bus-m is shown in Figure 6.17. A time-step of 4 μs is used to obtain this waveform. A zoom of Figure 6.17 is shown in Figure 6.18 for to better observe the differences between the detailed model and the 50-order (5-kHz maximum fitting frequency) FDNE. These figures demonstrate a high accuracy of the 50-order FDNE model enforced by the PSRP method, validating the proposed technique.

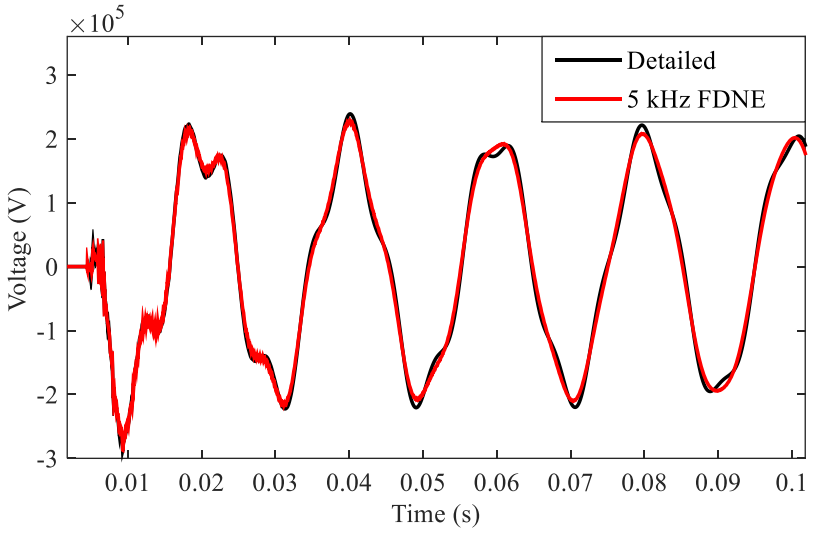

Figure 6.17. Transient voltage at phase *a* of bus m of the network of Figure 1.4.

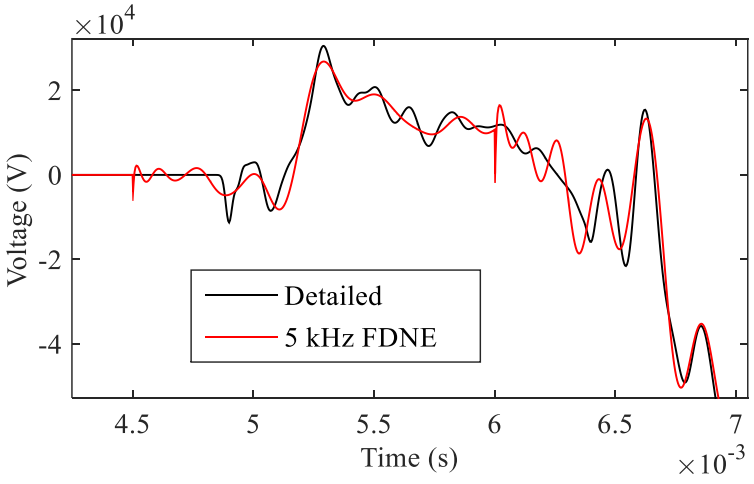

Figure 6.18. Zoom of the transient voltage of Figure 6.17.

6.5 Conclusions

In this chapter, a novel technique named Pole-Selective Residue Perturbation (PSRP) for the passivity enforcement of FDNEs has been proposed. The PSRP technique is especially advantageous when it is applied to high-order multi-port FDNEs, for which traditional techniques are extremely slow and sometimes unable to find a solution.

The main features of the proposed PSRP method are: 1. only selected residues of the rational model are perturbed, and 2. the perturbations are computed by simple algebraic calculations. These features of the PSRP method make the proposed passivity enforcement procedure much more efficient as compared to existing methods.

The proposed PSRP method has been applied to practical test cases. In general, a similar (slight) deviation of the fitting accuracy has been observed by the PSRP technique compared to the traditional techniques. On the other hand, the computational performance of the PSRP method is far better. Some rational models enforced by the PSRP technique have been tested in time-domain simulations and compared with the original models. The resulting waveforms show an excellent agreement between the FDNEs and original models, validating the proposed PSRP technique.

CHAPTER 7 CONCLUSIONS AND RECOMENDATIONS

7.1 Summary

This thesis presents improved techniques for the calculation of FDNEs in terms of curve fitting and passivity enforcement. Also, different analysis and studies are presented throughout this thesis as follows.

In Chapter 1, a historical review is given discussing the main advancements in the literature regarding the calculation of equivalent models for dynamic systems, such as FDNEs. Also, a discussion about the computational gain, advantages and limitations of the usage of FDNEs for electromagnetic transient studies is provided. This analysis defines the scope of the thesis.

In Chapter 2, the required conditions for FDNE modeling, such as linearity, stability and passivity are studied. In Chapter 3, the theoretical fundaments of the VF, MPM and LM techniques for rational modeling are presented, including a modified (novel) LM technique. Additionally, the Hamiltonian matrix-based method for the passivity assessment of FDNEs is presented, followed by the study of the so-called half-size singularity test matrix. Finally, the passivity enforcement techniques FRP, HMP and SDP are revisited.

In Chapter 4, the study of existing fitting techniques is complemented by performing different numerical comparisons and analyses for the fitting of different frequency-domain functions. Such studies demonstrate a higher fitting accuracy by the VF method over the MPM and LM techniques. On the other hand, the MPM and LM techniques are shown to be useful tools for model order identification.

Based on the theoretical review presented in Chapter 3 and the numerical comparisons of existing fitting techniques of Chapter 4, a new (improved) fitting technique is proposed in Chapter 5. The proposed fitting technique consists of a combination of either the MPM or the LM technique with the VF method. The resulting combined fitting approach is demonstrated to achieve a better performance compared to the application of any of the involved techniques individually. A unique advantage of the proposed technique is that the model order can be determined automatically. Some analysis about the impact of the model order on the passivity of rational models are also presented in this chapter.

A novel passivity enforcement technique, named PSRP, is proposed in Chapter 6. In this chapter, first, the causes of passivity violations are analyzed. Then, the contribution of a single pair of complex conjugate poles to individual passivity violations are studied. These analyses constitute the basis for the proposed PSRP technique. Unlike the existing passivity enforcement methods, the proposed PSRP technique is based on an algebraic solution. Also, by applying the PSRP technique only a few residue matrices are perturbed instead of all of them (as it is done by the traditional methods). As it is demonstrated with numerical examples, these two main features of the PSRP technique, result in substantial computational savings compared to the traditional methods. As for some FDNEs with many ports and/or high-order models, it is demonstrated that sometimes the existing techniques fail due to the large computational burden required, whereas the PSRP technique achieves effective solutions for all cases. Additionally, some transient simulations using the FDNEs with passivity enforced by the PSRP are presented. The resulting transient waveforms by using the FDNE model and the detail model result in very close agreement, validating the effectiveness of the PSRP technique.

The publications derived from this thesis are [67, 71-75].

7.2 Future work

As for future work, it is believed that it would be interesting to explore alternative fitting techniques that have not been studied in this thesis. For example, the Brune's realizations method is an interesting option, since the obtained equivalent model is guaranteed to be passive [38]. Another fitting technique with passivity guaranteed, is based on genetic algorithms, as reported in [37]. These two techniques, however, have not been applied to multiport FDNE models.

Another alternative to be studied is the combination of the techniques proposed in this thesis with Model Order Reduction (MOR) techniques, as presented in [76, 77].

BIBLIOGRAPHY

[1] G. L. Rabkin, A. Mitrofanov, and Y. O. Shterenberg, "On the determination of the numerical values of the coefficients of the transfer function of linearized links and systems from experimental frequency characteristics," *Automation and Remote Control*, vol. 16, no. 5, 1955.

[2] A. A. Kardashov and L. V. Karnyushin, "Determination of system parameters from experimental frequency characteristics," *Automation and Remote Control,* Jour vol. 19, no. 4, pp. 327-338, 1958.

[3] E. C. Levy, "Complex-curve fitting," *Institute of Radio Engineers -- Transactions on Automatic Control,* Jour vol. AC-4, no. 1, pp. 37-43, 1959.

[4] A. Clerici and L. Marzio, "Coordinated use of TNA and digital computer for switching-curve studies: transient equivalent of a complex network," *IEEE Transactions on Power Apparatus and Systems,* Jour vol. PAS-89, no. 8, pp. 1717-26, 1970.

[5] D. C. Youla, J. D. Rhodes, and P. C. Marston, "Driving-point synthesis of resistor-terminated cascades composed of lumped lossless passive 2-ports and commensurate TEM lines," *IEEE Transactions on Circuit Theory,* Jour vol. CT-19, no. 6, pp. 648-64, 1972.

[6] T. Koga, "Synthesis of a resistively terminated cascade of uniform lossless transmission lines and lumped passive lossless two- ports," Jour vol. CT18, no. 4, pp. 444-455, 1971.

[7] A. J. Riederer and L. Weinberg, "Synthesis of lossy lumped-distributed cascade networks," *IEEE Transactions on Circuits and Systems,* Jour vol. CAS-28, no. 12, pp. 1137-52, 1981.

[8] A. J. Riederer and L. Weinberg, "Synthesis of lumped-distributed networks: lossless cascades," *IEEE Transactions on Circuits and Systems,* Jour vol. CAS-27, no. 10, pp. 943-56, 1980.

[9] A. S. Morched and V. Brandwajn, "Transmission network equivalents for electromagnetic transients studies," *IEEE Transactions on Power Apparatus and Systems,* Jour vol. PAS-102, no. 9, pp. 2984-94, 1983.

[10] V. Que Do and M. M. Gavrilovic, "An iterative pole-removal for synthesis of power system equivalent networks," *IEEE Transactions on Power Apparatus and Systems,* Jour vol. PAS-103, no. 8, pp. 2065-70, 1984.

[11] A. S. Morched, J. H. Ottevangers, and L. Marti, "Multiport Frequency-Dependent Network Equivalents for the EMTP," *IEEE Transactions on Power Delivery,* vol. 8, no. 3, pp. 1402-1412, Jul 1993.

[12] A. Abur and H. Singh, "Time-Domain Modeling of External Systems for Electromagnetic Transients Programs," *IEEE Transactions on Power Systems,* vol. 8, no. 2, pp. 671-679, May 1993.

[13] W. C. Boaventura, A. Semlyen, M. R. Iravani, and A. Lopes, "Robust Sparse Network Equivalent for Large Systems: Part II—Performance Evaluation," *IEEE Transactions on Power Systems,* vol. 19, no. 1, pp. 293-299, 2004.

[14] W. C. Boaventura, A. Semlyen, M. R. Iravani, and A. Lopes, "Robust Sparse Network Equivalent for Large Systems: Part I—Methodology," *IEEE Transactions on Power Systems,* vol. 19, no. 1, pp. 157-163, 2004.

[15] A. Semlyen and M. R. Iravani, "Frequency-Domain Modeling of External Systems in an Electromagnetic Transients Program," *IEEE Transactions on Power Systems,* vol. 8, no. 2, pp. 527-533, May 1993.

[16] B. Gustavsen and A. Semlyen, "Simulation of transmission line transients using vector fitting and modal decomposition," *IEEE Transactions on Power Delivery,* vol. 13, no. 2, pp. 605-614, Apr 1998.

[17] B. Gustavsen and A. Semlyen, "Combined phase and modal domain calculation of transmission line transients based on vector fitting," *IEEE Transactions on Power Delivery,* vol. 13, no. 2, pp. 596-604, Apr 1998.

[18] B. Gustavsen and A. Semlyen, "Application of vector fitting to state equation representation of transformers for simulation of electromagnetic transients," *IEEE Transactions on Power Delivery,* vol. 13, no. 3, pp. 834-842, Jul 1998.

[19] B. Gustavsen and A. Semlyen, "Rational approximation of frequency domain responses by vector fitting," *IEEE Transactions on Power Delivery,* vol. 14, no. 3, pp. 1052-1061, Jul 1999.

[20] W. Hendrickx and T. Dhaene, "A Discussion of "Rational Approximation of Frequency Domain Responses by Vector Fitting"," *IEEE Transactions on Power Systems,* vol. 21, no. 1, pp. 441-443, 2006.

[21] C. K. Sanathanan and J. Koerner, "Transfer function synthesis as a ratio of two complex polynomials," *IEEE Transactions on Automatic Control,* Jour vol. AC-8, no. 1, pp. 56-58, 1963.

[22] B. Gustavsen, "Computer code for rational approximation of frequency dependent admittance matrices," *IEEE Transactions on Power Delivery,* vol. 17, no. 4, pp. 1093-1098, 2002.

[23] Y. S. Mekonnen and J. E. Schutt-Aine, "Fast macromodeling technique of sampled Time/Frequency data using z-domain vector-fitting method," *Electrical Performance of Electronic Packaging,* pp. 47-50, 2007.

[24] M. Abdel-Rahman, A. Semlyen, and M. Reza Iravani, "Two-layer network equivalent for electromagnetic transients," *IEEE Transactions on Power Delivery,* vol. 18, no. 4, pp. 1328-1335, 2003.

[25] J. R. Marti, "Accurate Modelling of Frequency-Dependent Transmission Lines in Electromagnetic Transient Simulations," *IEEE transactions on power apparatus and systems,* Jour vol. PAS-101, no. 1, pp. 147-157, 1982.

[26] T. Noda, "Identification of a Multiphase Network Equivalent for Electromagnetic Transient Calculations Using Partitioned Frequency Response," *IEEE Transactions on Power Delivery,* vol. 20, no. 2, pp. 1134-1142, 2005.

[27] T. K. Sarkar and O. Pereira, "Using the Matrix Pencil Method to Estimate the Parameters of a Sum of Complex Exponentials," *IEEE Antennas and Propagation Magazine,* vol. 37, no. 1, pp. 48-55, Feb 1995.

[28] T. K. Sarkar, J. Nebat, D. D. Weiner, and V. K. Jain, "Suboptimal approximation/identification of transient waveforms from electromagnetic systems by pencil-of-function method," *IEEE Transactions on Antennas and Propagation,* Jour vol. AP-28, no. 6, pp. 928-33, 1980.

[29] H. Jun-Hee and P. Jong-Keun, "A time-domain approach to transmission network equivalents via Prony analysis for electromagnetic transients analysis," *IEEE Transactions on Power Systems,* Jour vol. 10, no. 4, pp. 1789-97, 1995.

[30] S. Grivet-Talocia, "Package macromodeling via time-domain vector fitting," *IEEE Microwave and Wireless Components Letters,* vol. 13, no. 11, pp. 472-474, Nov 2003.

[31] K. Sheshyekani and B. Tabei, "Multiport Frequency-Dependent Network Equivalent Using a Modified Matrix Pencil Method," *IEEE Transactions on Power Delivery,* vol. 29, no. 5, pp. 2340-2348, Oct 2014.

[32] K. Sheshyekani, H. R. Karami, P. Dehkhoda, M. Paolone, and F. Rachidi, "Application of the Matrix Pencil Method to Rational Fitting of Frequency-Domain Responses," *IEEE Transactions on Power Delivery,* vol. 27, no. 4, pp. 2399-2408, Oct 2012.

[33] S. Lefteriu and A. C. Antoulas, "A New Approach to Modeling Multiport Systems From Frequency-Domain Data," *IEEE Transactions on Computer-Aided Design of Integrated Circuits and Systems,* vol. 29, no. 1, pp. 14-27, 2010.

[34] G. Gurrala, "Loewner matrix approach for modelling FDNEs of power systems," *Electric Power Systems Research,* vol. 125, pp. 116-123, Aug 2015.

[35] M. Kabir and R. Khazaka, "Loewner Matrix Macromodeling for Y-Parameter Data With a Priori D Matrix Extraction," *IEEE Transactions on Microwave Theory and Techniques,* vol. 64, no. 12, pp. 4098-4107, Dec 2016.

[36] Y. Z. Hu, W. C. Wu, and B. M. Zhang, "A Fast Method to Identify the Order of Frequency-Dependent Network Equivalents," *IEEE Transactions on Power Systems,* vol. 31, no. 1, pp. 54-62, Jan 2016.

[37] I. R. Pordanjani, C. Y. Chung, H. E. Mazin, and W. Xu, "A Method to Construct Equivalent Circuit Model From Frequency Responses With Guaranteed Passivity," *IEEE Transactions on Power Delivery,* vol. 26, no. 1, pp. 400-409, Jan 2011.

[38] M. Ahmadi and A. M. Gole, "A new approach to model frequency dependent network equivalents in transient simulation tools," presented at the IPST, Seoul, Republic of Korea, 2017.

[39] O. Brune, "Synthesis of a finite two-terminal network whose driving-point impedance is a prescribed function of frequency," *Journal of Math and Physics,* vol. 10, pp. 191-236, 1931.

[40] S. Grivet-Talocia, "Passivity enforcement via perturbation of Hamiltonian matrices," *IEEE Transactions on Circuits and Systems I-Regular Papers,* vol. 51, no. 9, pp. 1755-1769, Sep 2004.

[41] A. Semlyen and B. Gustavsen, "A Half-Size Singularity Test Matrix for Fast and Reliable Passivity Assessment of Rational Models," *IEEE Transactions on Power Delivery,* vol. 24, no. 1, pp. 345-351, Jan 2009.

[42] B. Gustavsen, "Fast passivity enforcement for pole-residue models by perturbation of residue matrix eigenvalues," *IEEE Transactions on Power Delivery,* vol. 23, no. 4, pp. 2278-2285, Oct 2008.

[43] C. P. Coelho, J. Phillips, and L. M. Silveira, "A convex programming approach for generating guaranteed passive approximations to tabulated frequency-data," *IEEE Transactions on Computer-Aided Design of Integrated Circuits and Systems,* vol. 23, no. 2, pp. 293-301, Feb 2004.

[44] Y. Z. Hu, W. C. Wu, A. M. Gole, and B. M. Zhang, "A Guaranteed and Efficient Method to Enforce Passivity of Frequency-Dependent Network Equivalents," *IEEE Transactions on Power Systems,* vol. 32, no. 3, pp. 2455-2463, May 2017.

[45] U. D. Annakkage *et al.*, "Dynamic System Equivalents: A Survey of Available Techniques," *IEEE Transactions on Power Delivery,* vol. 27, no. 1, pp. 411-420, Jan 2012.

[46] A. C. Antoulas, "An overview of approximation methods for large-scale dynamical systems," *Annual Reviews in Control,* vol. 29, no. 2, pp. 181-190, 2005.

[47] A. I. Ibrahim, "Frequency dependent network equivalents for electromagnetic transients studies: a bibliographical survey," *International Journal of Electrical Power & Energy Systems,* vol. 25, no. 3, pp. 193-199, Mar 2003.

[48] R. Pintelon, P. Guillaume, Y. Rolain, J. Schoukens, and H. Vanhamme, "Parametric Identification of Transfer-Functions in the Frequency-Domain - a Survey," *IEEE Transactions on Automatic Control,* vol. 39, no. 11, pp. 2245-2260, Nov 1994.

[49] N. Watson and J. Arrillaga, A. T. J. a. D. F. Warne, Ed. *Power Systems Electromagnetic Transients Simulations*. London, United Kingdom: The Institution of Engineering and Technology, 2007.

[50] J. Mahseredjian, S. Dennetiere, L. Dube, B. Khodabakhchian, and L. Gerin-Lajoie, "On a new approach for the simulation of transients in power systems," *Electric Power Systems Research,* vol. 77, no. 11, pp. 1514-1520, Sep 2007.

[51] I. Lafaia, J. Mahseredjian, A. Ametani, M. T. C. de Barros, I. Kocar, and Y. Fillion, "Frequency and Time Domain Responses of Cross-Bonded Cables," *IEEE Transactions on Power Delivery,* vol. 33, no. 2, pp. 640-648, Apr 2018.

[52] A. Morched, B. Gustavsen, and M. Tartibi, "A universal model for accurate calculation of electromagnetic transients on overhead lines and underground cables," *IEEE Transactions on Power Delivery,* vol. 14, no. 3, pp. 1032-1038, Jul 1999.

[53] I. Lafaia, A. Ametani, J. Mahseredjian, A. Naud, M. T. C. de Barros, and I. Kocar, "Field Test and Simulation of Transients on the RTE 225 kV Cable," *IEEE Transactions on Power Delivery,* vol. 32, no. 2, pp. 628-637, Apr 2017.

[54] "Matlab 2014b," ed. United States: Mathworks, 2014.

[55] J. G. Proakis and D. G. Manolakis, *Digital Signal Processing*, 4th ed. Pearson Prentice Hall, 2007.

[56] S. Grivet-Talocia and B. Gustavsen, *Passive Macromodeling, Theory and Applications*. Wiley, 2016.

[57] P. Triverio, S. Grivet-Talocia, M. S. Nakhla, F. G. Canavero, and R. Achar, "Stability, Causality, and Passivity in Electrical Interconnect Models," *IEEE Transactions on advance packaging,* vol. 30, pp. 795-808, 2007.

[58] B. Gustavsen, "Improving the pole relocating properties of vector fitting," *IEEE Transactions on Power Delivery,* vol. 21, no. 3, pp. 1587-1592, Jul 2006.

[59] M. Kabir and R. Khazaka, "Macromodeling of Distributed Networks From Frequency-Domain Data Using the Loewner Matrix Approach," *IEEE Transactions on Microwave Theory and Techniques*, vol. 60, no. 12, pp. 3927-3938, Dec 2012.

[60] B. Gustavsen and A. Semlyen, "Enforcing passivity for admittance matrices approximated by rational functions," *IEEE Transactions on Power Systems,* vol. 16, no. 1, pp. 97-104, Feb 2001.

[61] Z. C. Ye, "pmm: A Matlab Toolbox for Passive Macromodeling in RF/mm-wave Circuit Design," *2013 IEEE 10th International Conference on Asic (Asicon),* 2013.

[62] CVX Research Inc. (2011). *CVX: Matlab software for disciplined convex programming. http://cvxr.com/cvx, version 2.0.*

[63] M. B. Grant, S., "Graph implementations for nonsmooth convex programs, Recent Advances in Learning and Control (a tribute to M. Vidyasagar)," *Lecture Notes in Control and Information Sciences, Springer,* 2008.

[64] D. Deschrijver, B. Gustavsen, and T. Dhaene, "Advancements in iterative methods for rational approximation in the frequency domain," *IEEE Transactions on Power Delivery,* vol. 22, no. 3, pp. 1633-1642, Jul 2007.

[65] I. Kocar and J. Mahseredjian, "Accurate Frequency Dependent Cable Model for Electromagnetic Transients," *IEEE Transactions on Power Delivery,* vol. 31, no. 3, pp. 1281-1288, Jun 2016.

[66] I. Kocar, J. Mahseredjian, and G. Olivier, "Weighting method for transient analysis of underground cables," *IEEE Transactions on Power Delivery,* vol. 23, no. 3, pp. 1629-1635, Jul 2008.

[67] J. Morales, J. Mahseredjian, K. Sheshyekani, A. Ramirez, E. Medina, and I. Kocar, "Pole-Selective Residue Perturbation Technique for Passivity Enforcement of FDNEs," *IEEE Transactions on Power Delivery,* vol. 33, no. 6, pp. 2746-2754, Dec 2018.

[68] B. Gustavsen, "Passivity enforcement of rational models via modal perturbation," *IEEE Transactions on Power Delivery,* vol. 23, no. 2, pp. 768-775, Apr 2008.

[69] B. Gustavsen, "Improving the pole relocating properties of vector fitting," *2006 Power Engineering Society General Meeting, Vols 1-9,* pp. 916-916, 2006.

[70] L. P. R. K. Ihlenfeld, G. H. C. Oliveira, and M. R. Sans, "A data passivity-enforcement preprocessing approach to multiport system modeling," *IEEE Transactions on Power Delivery,* vol. 31, no. 3, pp. 1351-1359, June 2016.

[71] E. Medina, A. Ramirez, J. Morales, and J. Mahseredjian, "Alternative Approach to Alleviate Passivity Violations of Rational-Based Fitted Functions," *IEEE Transactions on Power Delivery*, Accepted for publication 2019.

[72] E. Medina, J. Morales, and A. Ramirez, "Identification of FDNEs via Frequency-Partitioned Loewner Matrix Fitting Technique," presented at the IEEJ-HV Conference, Montreal, Canada, 2018.

[73] J. Morales, E. Medina, J. Mahseredjian, A. Ramirez, K. Sheshyekani, and I. Kocar, "A Loewner/MPM – VF Combined Rational Fitting Approach," *Submitted to IEEE Transactions on Power Delivery,* 2019.

[74] J. Morales, E. Medina, J. Mahseredjian, A. Ramirez, and K. Sheshyekani, "A Comparative Study of Fitting Techniques," presented at the IPST Conference, Perpignan, France, 2019.

[75] J. Morales, J. Mahseredjian, K. Sheshyekani, A. Ramirez, E. Medina, and I. Kocar, "Frequency-Domain Fitting Techniques: A Review," *Submitted to IEEE Transactions on Power Delivery,* 2019.

[76] A. Ramirez *et al.*, "Application of balanced realizations for model-order reduction of dynamic power system equivalents," *IEEE Transactions on Power Delivery,* vol. 31, no. 5, pp. 2304 - 2312, Oct 2016.

[77] A. Ramirez, A. Semlyen, and R. Iravani, "Order reduction of the dynamic model of a linear weakly periodic system-part I: general methodology," *IEEE Transactions on Power Systems,* vol. 19, no. 2, pp. 857-865, May 2004.

APPENDIX A – STATE-SPACE FORM OF RATIONAL MODELS

In this appendix, the equivalent state-space representation of the rational model given in (2.3) is given. Let us start, for simplicity, with the scalar-function rational model

$$f(s)=\sum_{n=1}^{N}\frac{r_n}{s-a_n}+d+se\,. \tag{A.1}$$

This rational function admits the following matrix-vector representation

$$f(s)=\begin{bmatrix}r_1 & \cdots & r_N\end{bmatrix}\left\{s\begin{bmatrix}1 & & \\ & \ddots & \\ & & 1\end{bmatrix}-\begin{bmatrix}a_1 & & \\ & \ddots & \\ & & a_N\end{bmatrix}\right\}^{-1}\begin{bmatrix}1\\ \vdots \\ 1\end{bmatrix}+d+e\,. \tag{A.2}$$

Note that (A.2) has the same form as the transfer function (2.6), repeated here as

$$f(s)=\mathbf{C}\left(s\mathbf{I}-\mathbf{A}\right)^{-1}\mathbf{B}+\mathbf{D}+s\mathbf{E}\,, \tag{A.3}$$

which corresponds to the state-space model (2.4) and (2.5). Then, for the rational function (A.1), the corresponding state-space model matrices are

$$\mathbf{A}=\operatorname{diag}\left(\begin{bmatrix}a_1 & \cdots & a_N\end{bmatrix}\right). \tag{A.4}$$

$$\mathbf{B}=\begin{bmatrix}1 & \cdots & 1\end{bmatrix}^T. \tag{A.5}$$

$$\mathbf{C}=\begin{bmatrix}r_1 & \cdots & r_N\end{bmatrix}. \tag{A.6}$$

$$\mathbf{D}=d\,. \tag{A.7}$$

$$\mathbf{E}=e\,. \tag{A.8}$$

Now, let us consider the multiport rational model (2.3), repeated here as

$$\mathbf{Y}_{fitted}(s)=\sum_{n=1}^{N}\frac{\mathbf{R}_n}{s-a_n}+\mathbf{D}+s\mathbf{E}\,. \tag{A.9}$$

Similar to the scalar function (A.1), the rational model (A.9) as the following equivalent matrix-vector representation (analogous to (A.2))

$$\mathbf{Y}_{fitted}(s)=\begin{bmatrix} r_{11,1} & \cdots & r_{11,N} & \cdots & r_{1p,1} & \cdots & r_{1p,N} \\ \vdots & & \vdots & & \vdots & & \vdots \\ r_{p1,1} & \cdots & r_{p1,N} & \cdots & r_{pp,1} & \cdots & r_{pp,N} \end{bmatrix}\left\{ s\mathbf{I}-\begin{bmatrix} a_1 & & & & & & \\ & \ddots & & & & & \\ & & a_N & & & & \\ & & & \ddots & & & \\ & & & & a_1 & & \\ & & & & & \ddots & \\ & & & & & & a_N \end{bmatrix}\right\}^{-1}\begin{bmatrix} 1 & & \\ \vdots & & \\ 1 & & \\ & \ddots & \\ & & 1 \\ & & \vdots \\ & & 1 \end{bmatrix}+\mathbf{D}+s\mathbf{E}, \quad \text{(A.10)}$$

where the elements $r_{ij,n}$ denote the (i, j) entries of the n^{th} residue matrix $\mathbf{R}_n$.

Thus, for the matrix-form rational model (A.9), its equivalent state-space form is given by

$$\mathbf{A}=\text{diag}\left(\begin{bmatrix} a_1 & \cdots & a_N & \cdots & a_1 & \cdots & a_N \end{bmatrix}\right), \quad \text{(A.11)}$$

$$\mathbf{B}=\begin{bmatrix} 1 & & \\ \vdots & & \\ 1 & & \\ & \ddots & \\ & & 1 \\ & & \vdots \\ & & 1 \end{bmatrix}, \quad \text{(A.12)}$$

$$\mathbf{C}=\begin{bmatrix} r_{11,1} & \cdots & r_{11,N} & \cdots & r_{1p,1} & \cdots & r_{1p,N} \\ \vdots & & \vdots & & \vdots & & \vdots \\ r_{p1,1} & \cdots & r_{p1,N} & \cdots & r_{pp,1} & \cdots & r_{pp,N} \end{bmatrix}. \quad \text{(A.13)}$$

Note that matrices $\mathbf{D}$ and $\mathbf{E}$ in (A.9) remain the same for the state-space form model.

It is important to note that the abovementioned state-space model contains complex entries if the associated rational model contains complex poles/residues. There exists, however, an alternative purely real state-space model representation for complex rational models, given as follows.

For each complex conjugate pair of poles and residues, the frequency response is

$$f(s)=\frac{r}{s-a}+\frac{r^*}{s-a^*}=\frac{r'+\mathrm{j}r''}{s-(a'+\mathrm{j}a'')}+\frac{r'-\mathrm{j}r''}{s-(a'-\mathrm{j}a'')}. \tag{A.14}$$

The rational model subsystem of (A.14) can be equivalently represented by the state-space form

$$\mathbf{A}=\begin{bmatrix} a' & a'' \\ -a'' & a' \end{bmatrix}, \tag{A.15}$$

$$\mathbf{B}=\begin{bmatrix} 2 \\ 0 \end{bmatrix}, \tag{A.16}$$

$$\mathbf{C}=\begin{bmatrix} r' & r'' \end{bmatrix}, \tag{A.17}$$

Thus, each pair of complex conjugate poles/residues of the rational model, can be represented by the corresponding 2×2 blocks as given by (A.15)-(A.17) into the state-space model given by (A.11) -(A.13).

APPENDIX B – S-DOMAIN ROC FOR CAUSAL AND BIBO-STABLE SYSTEMS

The Laplace transform of a generic time-domain signal $x(t)$ is defined as

$$X(s) = \int_{-\infty}^{+\infty} x(t)\, e^{-st} dt \tag{B.1}$$

where $s = \sigma + \mathrm{j}\omega t$.

However, the Laplace-domain signal $X(s)$ exists, if and only if, the integral in (B.1) converges to a finite value. Since s is a complex variable, the region of the complex plane (the set of values of s) for which the integral in (B.1) converges is defined as the region of convergence (ROC).

In the case of the impulse response of a causal system, as discussed in section 2.1.3, the following condition is given

$$h(t) = 0, \quad \forall t < 0. \tag{B.2}$$

For calculating the Laplace transform of this particular function, the inferior limit of the Laplace integral as given in (B.1), can be set to 0. Moreover, the complex variable in (B.1) can be expanded into real and imaginary parts, i.e.,

$$H(s) = \int_{0}^{\infty} \left[h(t)\, e^{-\mathrm{j}\omega t} \right] \left[e^{-\sigma t} \right] dt. \tag{B.3}$$

From (B.3), it can be observed that the convergence of the integral is not compromised by ω (the imaginary part of s). Thus, the ROC includes all the possible values in the imaginary axis. On the other hand, the convergence of the integral in (B.3) does depend on σ (the real part of s). The following three situations can occur:

1. If $\sigma < 0$, the integrand in (B.3) behaves as an exponentially growing function, such that its integral does not converge.
2. If $\sigma = 0$, the convergence of the integral in (B.3) may or not converge since it depends on the nature of $h(t)$. Thus, the convergence of the integral is not guaranteed.

3. Finally, if $\sigma > 0$, the integrand in (B.3) vanishes towards $t \to +\infty$, such that the integral converges to a finite value. Thus, for this case, the ROC includes the entire positive side of the real axis in the complex plane.

From this analysis, it can be concluded that the guaranteed ROC of the Laplace transform of the impulse response $h(t)$, for a causal system, is the open right side of the complex plane, i.e., $\mathrm{Re}\{s\} > 0 : s \in \mathbb{C}$.

Moreover, if, in addition to the causality condition, the outlined system is considered also BIBO stable, $h(t)$ also satisfies the following condition (as defined in Section 2.1.4)

$$\int_0^{+\infty} h(t)\,dt < \infty. \tag{B.4}$$

Under this condition, the convergence of (B.3) is also guaranteed for the case $\sigma = 0$. This means that for a causal and BIBO stable system, the region of convergence is the closed right side of the complex plane, i.e., $\mathrm{Re}\{s\} \geq 0 \ : s \in \mathbb{C}$.

APPENDIX C – IMPLEMENTATION OF FDNES IN EMTP

The state-space model in (2.4)-(2.5), repeated here as

$$\dot{\mathbf{x}}(t) = \mathbf{A}\mathbf{x}(t) + \mathbf{B}\mathbf{v}(t). \tag{C.1}$$

$$\mathbf{i}(t) = \mathbf{C}\mathbf{x}(t) + \mathbf{D}\mathbf{v}(t) + \mathbf{E}\dot{\mathbf{v}}(t). \tag{C.2}$$

can be included into time-domain simulations as follows. Considering the Modified-Augmented Nodal Analysis (MANA) approach used in the EMTP software, a Norton equivalent of the model in (C.1)-(C.2) is calculated. This Norton equivalent is obtained by discretizing (C.1)-(C.2) using the trapezoidal numerical integration technique, i.e.,

$$\mathbf{x}(t_{k+1}) = \mathbf{x}(t_k) + \frac{\Delta t}{2}\left\{ f\left[\mathbf{x}(t_k)\right] + f\left[\mathbf{x}(t_{k+1})\right]\right\}. \tag{C.3}$$

Firstly, the contribution of matrix **E** in (C.2) is treated separated, such that an auxiliary variable is defined as

$$\boldsymbol{\varphi}(t) = \mathbf{E}\dot{\mathbf{v}}(t). \tag{C.4}$$

Discretizing (C.4) via the trapezoidal method (C.3), the following expression is obtained

$$\boldsymbol{\varphi}(t_{k+1}) = -\boldsymbol{\varphi}(t_{k+1}) - \frac{2}{\Delta t}\mathbf{E}\mathbf{v}(t_k) + \frac{2}{\Delta t}\mathbf{E}\mathbf{v}(t_{k+1}). \tag{C.5}$$

In the same manner, discretizing (C.1) we obtain

$$\mathbf{x}(t_{k+1}) = \left[\left(\mathbf{I} - \frac{\Delta t}{2}\mathbf{A}\right)^{-1}\left(\mathbf{I} + \frac{\Delta t}{2}\mathbf{A}\right)\right]\mathbf{x}(t_{k+1}) + \frac{\Delta t}{2}\left(\mathbf{I} - \frac{\Delta t}{2}\mathbf{A}\right)^{-1}\mathbf{B}\left[\mathbf{v}(t_k) + \mathbf{v}(t_{k+1})\right]. \tag{C.6}$$

In discrete form, (C.2) can be written as

$$\mathbf{i}(t_{k+1}) = \mathbf{C}\mathbf{x}(t_{k+1}) + \mathbf{D}\mathbf{v}(t_{k+1}) + \boldsymbol{\varphi}(t_{k+1}). \tag{C.7}$$

Then, substituting (C.5) and (C.6) into (C.7) results into

$$\mathbf{i}(t_{k+1}) = \mathbf{C}\boldsymbol{\Gamma}\mathbf{x}(t_k) - \boldsymbol{\varphi}(t_k) + \left[\mathbf{C}\boldsymbol{\Theta} - \frac{2}{\Delta t}\mathbf{E}\right]\mathbf{v}(t_k) + \left[\mathbf{C}\boldsymbol{\Theta} + \mathbf{D} + \frac{2}{\Delta t}\mathbf{E}\right]\mathbf{v}(t_{k+1}). \tag{C.8}$$

where

$$\boldsymbol{\Gamma} = \left(\mathbf{I} - \frac{\Delta t}{2} \mathbf{A} \right)^{-1} \left(\mathbf{I} + \frac{\Delta t}{2} \mathbf{A} \right), \tag{C.9}$$

and

$$\boldsymbol{\Theta} = \frac{\Delta t}{2} \left(\mathbf{I} - \frac{\Delta t}{2} \mathbf{A} \right)^{-1} \mathbf{B} . \tag{C.10}$$

Finally, (C.8) can be expressed in the desired Norton equivalent form as

$$\mathbf{i}\left(t_{k+1}\right) = \mathbf{I}_{history} + \mathbf{G}_N \mathbf{v}\left(t_{k+1}\right), \tag{C.11}$$

where the Norton equivalent conductance matrix is

$$\mathbf{G}_N = \mathbf{C}\boldsymbol{\Theta} + \mathbf{D} + \frac{2}{\Delta t} \mathbf{E}, \tag{C.12}$$

and the equivalent history current is

$$\mathbf{I}_{history} = \mathbf{C}\boldsymbol{\Gamma}\mathbf{x}\left(t_k\right) - \boldsymbol{\varphi}\left(t_k\right) + \left[\mathbf{C}\boldsymbol{\Theta} - \frac{2}{\Delta t} \mathbf{E} \right] \mathbf{v}\left(t_k\right). \tag{C.13}$$